Production of Li, Be and B nuclei in the interaction of ^{12}C with ^{12}C at incident energies of 200 and 400 MeV

Joele Paulus Mira

Thesis submitted in fulfillment of the requirements for the degree of

Magister of Scientiae in the Department of Physics

University of the Western Cape

Supervisor: Dr. S. V. Förtsch

Physics Group

iThemba LABS

Co-supervisor: Prof. R. Lindsay

Department of Physics

University of the Western Cape

February 2008

DECLARATION

I, the undersigned, hereby declare that the work contained in this thesis is my own original work and that I have not previously in its entirety or in part submitted it at any university for a degree.

Signature: ……

Date: ……

KEYWORDS

- Double differential cross-sections
- Nucleon coalescence
- Fragmentation
- Break-up fusion
- Pre-equilibrium
- Evaporation
- FLUKA

Production of Li, Be and B nuclei in the interaction of ^{12}C with ^{12}C at incident energies of 200 and 400 MeV.

J. P Mira [a, b]

[a] University of the Western Cape, Private Bag X, Bellville 7535, South Africa
[b] iThemba LABS, Old Faure Road, Somerset West 7129, South Africa
e-mail: mira@tlabs.ac.za

ABSTRACT

The objective of this project is to study the production of Li, Be and B isotopes emitted in the interaction of ^{12}C with ^{12}C at incident energies of 200 and 400 MeV. The energies of these produced fragments were measured with a detector telescope consisting of two silicon detectors at the incident energy of 200 MeV while a third silicon detector was added for the measurements at 400 MeV. The ΔE-E technique was used for particle identification by measuring the energy loss in the thin ΔE detector and the energy deposited in the following E detector. A Bragg curve detector (BCD) with a low energy threshold was used to also measure the low energy component of the spectra of the detected fragments. Double differential cross sections of the $^{6,7,8}Li$, $^{7,9,10}Be$ and $^{8,10,11,12}B$ were extracted from the spectra over an angular range between 8° and 60° for the Si detector telescope, while for the BCD the cross sections were obtained over an angular range between 15° and 60°. Reaction mechanisms which were considered to interpret the energy spectra and to describe the production of $^{8,10,11,12}B$ in the interaction of ^{12}C with ^{12}C at 200 MeV incident energy, include projectile and target fragmentation, nucleon transfer, pre-equilibrium emission, nucleon coalescence through complete and incomplete fusion as well as evaporation. The nuclear transport and Monte Carlo code FLUKA was extended to also include the Boltzmann Master Equations (BME) to evaluate the contributions from nucleon coalescence, while the projectile and target fragmentation processes were calculated with the local plane wave (LPWA) approximation. Based on the qualitative and quantitative agreement between the measured spectra of the Li and Be isotopes with those of the B isotopes as a function of emission energy and emission angle, it is assumed that the same reaction mechanisms applied to describe the spectra of the B isotopes also play a predominant role in the production of the Be and Li isotopes.

Tlhahiso ya dinuclei tsa Li, Be le B thulanong ya ^{12}C le ^{12}C ka matla a petsetso a 200 le 400 MeV.

J. P Mira [a,b]

[a] University of the Western Cape, Private Bag X, Bellville 7535, South Africa
[b] iThemba LABS, Old Faure Road, Somerset West 7129, South Africa
e-mail: mira@tlabs.ac.za

ABSTRACT

Sepheo sa mantlha ka mosebetsi ona ke ho ithuta le ho batlisisa ka tlhahiso ya dikgetshwana tsa isotope tsa Lithium (Li), Beryllium (Be) le Boron (B) tse hlahang ha ho thulanngwa ^{12}C le ^{12}C ka matla a petsetso a 200 le 400 MeV. Matla a tlhahiso a dikgetshwana tsena tse hlahiswang ane a methwa ka *detector* tse pedi tsa *Silicon* moo ho sebedisitsweng matla a petsetso a 200 MeV, mme *detector* ya boraro ya *Silicon* e ile ya kenyelletswa tshebedisong ya matla a petsetso a 400 MeV. *Detector* ke sepapetlwana se tjhedikana se bobebenyana se sebedisetswang ho metha dikarolwana. ΔE-E ke mokgwa o ile wa sebediswa ho arohanya le ho tsebisa dikgetshwana ka ho metha matla a dikgetshwana a setseng ho ΔE *detector* le ho metha matla a keneng ho Si (E) *detector*. Bragg Curve Detector (BCD) ke *detector* e sebedisitsweng ho metha matla a dikgetshwana tse hlahisitsweng ka matla a manyenyane. Di *double differential cross sections* tsa ^{6,7,8}Li, ^{7,9,10}Be le ^{8,10,11,12}B di methilwe mahareng a 8° le 60° ho sebediswa *detector* ya *Silicon*, mme bakeng sa BCD di ile tsa methwa mahareng a 15° le 60°. Mekgwa e sebedisitsweng ho toboketsa le ho hlalosa tlhahiso ya ^{8,10,11,12}B thulanong ya ^{12}C le ^{12}C ya matla a petsetso a 200 MeV ke e latelang: *projectile* le *target fragmentation, nucleon transfer, pre-equilibrium emission, nucleon coalescence* ka *complete* le *incomplete fusion* le ka *evaporation*. Monte Carlo e bitswang FLUKA e ile ya fetolwa ho kenyeletsa Boltzmann Master Equation (BME) ho batlisisa *nucleon coalescence*, mme *projectile* le *target fragmentation* tsona di ile tsa batlisiswa ka *local plane wave approximation* (LPWA). Ho ya ka ditumellano tse ka bonwang pakeng tsa ditshwantsho tsa Lithium le Berrylium ha di bapiswa le tsa Boron, ho ka fihlellwa qeto ya hore mokgwa o sebeditseng ho hlahisa Boron o ka bapala karolo e kgolo ho hlahiseng isotopes tsa Lithium le Beryllium.

ACKNOWLEDGEMENTS

- Firstly I would like to express my sincere gratitude to my supervisor Dr S. V Förtsch and my co-supervisor Prof R. Lindsay for their invaluable supervision and support to the completion of this thesis.
- I would also like to thank Dr R. Nevelling and Dr F. D. Smit for helping me when my supervisor was not around.
- I like to thank my fellow students for their friendship and assistance to make our office suitable for studying.
- I would also like to express my sincere gratitude to my family for the support they give me. Ke leboha lerato le tsheetso tseo le mphang tsona, eka Ramasedi a ka le matlafatsa hore le dule le ntsheeditse ka moo le etsang ka teng. Modimo obe le lona mme ole boloke. Haholo ke leboha mme waka Mmathabo ka kgodiso eo a mphileng yona ho tloha bonyaneng baka le ho fihla le kajeno.
- This work is dedicated to my late brother Paseka Philemon Mira a.k.a "Buti" who passed away accidentally at the beginning of year 2007. He was a brother and a friend to me and I will always remember you.
- And most of all I would like to express my immense gratitude to my Heavenly Father for protecting me, and giving me power and strength to complete this thesis.

CONTENTS

CHAPTER 1 _____ *1*

Introduction _____ *1*

1.1 Overview _____ **1**

1.2 Reaction mechanisms _____ **2**

1.2.1 Nucleon coalescence through complete and incomplete fusion _____ 3
1.2.2 Pre-equilibrium emission _____ 4
1.2.3 Projectile and Target Fragmentation _____ 5
1.2.4 Evaporation _____ 5
1.2.5 Direct reaction and nucleon transfer _____ 6

1.3 Motivation of study _____ **7**

CHAPTER 2 _____ *9*

Experimental _____ *9*

2.1 Introduction _____ **9**

2.2 Silicon detectors _____ **9**

2.3 Bragg curve detector _____ **10**

2.3.1 BCD construction _____ 11
2.3.2 Principle of operation _____ 13

2.4 Experimental procedure _____ **14**

2.4.1 Beams _____ 14
2.4.2 Scattering chamber _____ 15
2.4.3 Targets _____ 17
2.4.4 Setup of the detectors _____ 18

2.5 Gas flow system of the BCD _____ **19**

2.6 Electronics _____ **19**

2.6.1 Detector signals and preamplifiers _____ 20
2.6.2 Linear signal of the silicon detector telescope _____ 20
2.6.3 Linear signal of BCD _____ 21
2.6.4 Logic signals of the Si detector telescope _____ 22
2.6.5 Logic signal of BCD _____ 23
2.6.6 Current integrator _____ 25
2.6.7 Pulsers _____ 25
2.6.8 Event trigger _____ 26
2.6.9 Pattern register _____ 26
2.6.10 Computer busy _____ 26
2.6.11 Clock _____ 27
2.6.12 Scalers _____ 27

CHAPTER 3 _____ *28*

Data analysis _____ *28*

3.1 Introduction _____ **28**

3.2 Data acquisition programs _____ **28**

3.3 Online data taking _____ **29**

3.4 Offline data replay _____ **30**

3.5 Energy calibrations _____ **30**

3.5.1 Si ΔE detector _____ 30

3.5.2 Si (E_1) Detector for 200 MeV 31
3.5.3 Si (E_1) detector 400 MeV 34
3.5.4 Si (E_2) detector 400 MeV 35
3.5.5 Bragg curve detector 36

3.6 Particle Identification 37
3.6.1 Silicon telescope 37
3.6.2 BCD 45

3.7 Background subtraction 49

3.8 Conversion to double differential cross section 50

3.9 Error analysis 52
3.9.1 Statistical error 52
3.9.2 Systematic error 53

CHAPTER 4 56

Theoretical Model 56

4.1 Introduction 56

4.2 Binary break-up mechanism 57

4.3 Nucleon coalescence 59

4.4 Complete and incomplete fusion 63

CHAPTER 5 65

Results and Discussion 65

5.1 Overview 65

5.2 Inclusive energy spectra of Li, Be and B isotopes 65

5.3 Angular distributions of Li, Be and B 77

5.4 Comparison of experimental energy spectra with the theoretical calculations 82

CHAPTER 6 94

Summary and conclusions 94

References 97

LIST OF FIGURES

1.1: Schematic representation of complete energy spectra showing the contributions of reaction mechanisms as a function of emission energy and excitation energy. 8
2.1: Photo of the active volume of the BCD. 12
2.2: The Bragg peak of a particle that stopped in the active volume of the BCD with range R, nuclear charge Z, energy loss dE/dx over distance x inside BCD. 14
2.3: The layout of the cyclotron facility at iThemba LABS. 16
2.4: Photograph of the scattering chamber showing the target ladder, BCD and silicon detector telescope. 17
2.5: Electronic diagram used to process the linear signals from the Si detectors for the 400 MeV run. 21
2.6: Block diagram used to process the logic signals of the Si detectors, here shown for the 400 MeV run. 24
2.7: Block diagram used to process the logic signals of the BCD. 25
3.1: Loci of the Li, Be and B isotopes calculated by ELOSS program curves overlaid onto the experimental ΔE-E spectrum. 31
3.2: Typical energy spectrum of the alpha particles from a ^{228}Th source measured with the Si (E_1) detector. Energies are given in MeV 32
3.3: Raw energy spectrum used to calibrate the Si (E_1) detector using a 200 MeV ^{12}C beam. 32
3.4: The calibration curve for the Si E_1 detector showing the straight line fitted through the high energy (discrete states) as well as the low energy points (alpha particles from ^{228}Th source) at 200 MeV ^{12}C beam. 33
3.5: Raw energy spectrum used to calibrate the Si (E_1) detector for 400 MeV ^{12}C beam using 100 MeV ^{12}C beam. 33
3.6: The calibration curve for the Si E_1 detector showing the straight line fitted through the high energy (discrete states) as well as the low energy points (alpha particles from ^{228}Th source) at 400 MeV ^{12}C beam. 34
3.7: The calibration curve for the Si E_2 detector showing the straight line fitted through the high energy (discrete states) as well as the low energy points (alpha particles from ^{228}Th source) at 400 MeV ^{12}C beam. 36

3.8: An energy spectrum of the alpha particles from a ^{228}Th source detected by the BCD. The only energy which is fully resolved is the 8.78 MeV energy line. 37
3.9: Si PID spectrum from the interaction of ^{12}C with ^{12}C at an incident energy of 200 MeV with gates set around the loci of Li, Be and B as shown. 39
3.10: Si (ΔE-E_1) PID spectrum from the interaction of ^{12}C with ^{12}C at an incident energy of 400 MeV with gates set around the loci of Li, Be and B as shown. 40
3.11: Si (E_1-E_2) PID spectrum from the interaction of ^{12}C with ^{12}C at an incident energy of 400 MeV with gates set around the loci of Li, Be and B as shown. 40
3.12: Mass function spectrum showing gates that have been set around the ^{6}Li, ^{7}Li and ^{8}Li loci in the interaction of ^{12}C with ^{12}C at an incident energy of 200 MeV. 41
3.13: Mass function spectrum from the (ΔE-E_1) detectors showing gates that have been set around ^{6}Li, ^{7}Li and ^{8}Li loci in the interaction of ^{12}C with ^{12}C at an incident energy of 400 MeV..... 41
3.14: Mass function spectrum from the (E_1-E_2) detectors showing gates that have been set around ^{6}Li, ^{7}Li and ^{8}Li loci in the interaction of ^{12}C with ^{12}C at an incident energy of 400 MeV..... 42
3.15: Mass function spectrum showing gates that have been set around ^{7}Be, ^{9}Be and ^{10}Be loci in the interaction of ^{12}C with ^{12}C at an incident energy of 200 MeV..... 42
3.16: Mass function spectrum from the (ΔE-E_1) detectors showing gates that have been set around ^{7}Be, ^{9}Be and ^{10}Be loci in the interaction of ^{12}C with ^{12}C at an incident energy of 400 MeV..... 43
3.17: Mass function spectrum from the (E_1-E_2) detectors showing gates that have been set around ^{7}Be, ^{9}Be and ^{10}Be loci in the interaction of ^{12}C with ^{12}C at an incident energy of 400 MeV..... 43
3.18: Mass function spectrum showing gates that have been set around ^{8}B, ^{10}B, ^{11}B and ^{12}B loci in the interaction of ^{12}C with ^{12}C at an incident energy of 200 MeV. 44
3.19: Mass function spectrum from the (ΔE-E_1) detectors showing gates that have been set around ^{8}B, ^{10}B, ^{11}B and ^{12}B loci in the interaction of ^{12}C with ^{12}C at an incident energy of 400 MeV..... 44
3.20: Mass function spectrum from the (E_1-E_2) detectors showing gates that have been set around ^{8}B, ^{10}B, ^{11}B and ^{12}B loci in the interaction of ^{12}C with ^{12}C at an incident energy of 400 MeV..... 45

3.21: Raw BCD PID spectrum with background caused by protons and alphas punching through the detector. 46
3.22: Gated energy versus pulse length spectrum used to generate the BCD PID spectrum. 47
3.23: Generated BCD PID spectrum with gates set around the fragments of Lithium, Beryllium and Boron in the interaction of ^{12}C with ^{12}C at a beam energy of 200 MeV. 47
3.24: BCD PID spectrum with gates set around ^{6}Li and ^{7}Li loci in the interaction of ^{12}C with ^{12}C. 48
3.25: BCD PID spectrum with gates set around ^{7}Be and ^{9}Be loci in the interaction of ^{12}C with ^{12}C. 48
3.26: BCD PID spectrum with gates set around ^{8}B ^{10}B and ^{11}B loci in the interaction of ^{12}C with ^{12}C. 49
3.27: Sum of the energy spectra of ^{7}Li from the Si ($\Delta E+E_1+ E_2$) detector at an incident energy of 400 MeV. Data are binned in 1 MeV energy bins. 52
5.1: Double differential cross sections of ^{6}Li emitted in the interaction of ^{12}C with ^{12}C at incident energies of 200 and 400 MeV at different emission angles as indicated. The BCD data are given by the stars. The error bars reflect the statistical errors. 67
5.2: Double differential cross sections of ^{7}Li emitted in the interaction of ^{12}C with ^{12}C at incident energies of 200 and 400 MeV at different emission angles as indicated. The BCD data are given by the stars. The error bars reflect the statistical errors. 68
5.3: Double differential cross sections of ^{8}Li emitted in the interaction of ^{12}C with ^{12}C at incident energies of 200 and 400 MeV at different emission angles as indicated. The BCD data are given by the stars. The error bars reflect the statistical errors. 69
5.4: Double differential cross sections of ^{7}Be emitted in the interaction of ^{12}C with ^{12}C at incident energies of 200 and 400 MeV at different emission angles as indicated. The BCD data are given by the stars. The error bars reflect the statistical errors. 70
5.5: Double differential cross sections of ^{9}Be emitted in the interaction of ^{12}C with ^{12}C at incident energies of 200 and 400 MeV at different emission angles as

indicated. The BCD data are given by the stars. The error bars reflect the statistical errors..... 71
5.6: Double differential cross sections of ^{10}Be emitted in the interaction of ^{12}C with ^{12}C at incident energies of 200 and 400 MeV at different emission angles as indicated. The BCD data are given by the stars. The error bars reflect the statistical errors..... 72
5.7: Double differential cross sections of ^{8}B emitted in the interaction of ^{12}C with ^{12}C at incident energies of 200 and 400 MeV at different emission angles as indicated. The BCD data are given by the stars. The error bars reflect the statistical errors..... 73
5.8: Double differential cross sections of ^{10}B emitted in the interaction of ^{12}C with ^{12}C at incident energies of 200 and 400 MeV at different emission angles as indicated. The BCD data are given by the stars. The error bars reflect the statistical errors..... 74
5.9: Double differential cross sections of ^{11}B emitted in the interaction of ^{12}C with ^{12}C at incident energies of 200 and 400 MeV at different emission angles as indicated. The BCD data are given by the stars. The error bars reflect the statistical errors..... 75
5.10: Double differential cross sections of ^{12}B emitted in the interaction of ^{12}C with ^{12}C at incident energies of 200 and 400 MeV at different emission angles as indicated. The BCD data are given by the stars. The error bars reflect the statistical errors..... 76
5.11: Double differential cross sections of ^{7}Li, ^{7}Be ^{11}B emitted at a forward angle of 8° and a backward angle of 60° in the interaction of ^{12}C with ^{12}C at incident energies of 200 and 400 MeV. The error bars reflect the statistical errors..... 77
5.12: Angular distributions of ^{6}Li, ^{7}Li and ^{8}Li measured in the laboratory system in the interaction of ^{12}C with ^{12}C at incident energies of 200 and 400 MeV. The beam energies and the fragments with their emission energies are given in the figures. The error bars reflect the statistical errors..... 79
5.13: Angular distributions of ^{7}Be, ^{9}Be and ^{10}Be measured in the laboratory system the interaction of ^{12}C with ^{12}C at incident energies of 200 and 400 MeV. The beam energies and the fragments with their emission energies are given in the figures. The error bars reflect the statistical errors..... 80

5.14: Angular distributions of ^{8}B, ^{10}B, ^{11}B and ^{12}B measured in the laboratory system in the interaction of ^{12}C with ^{12}C at incident energies of 200 and 400 MeV. The beam energies and the fragments with their emission energies are given in the figures. The error bars reflect the statistical errors. 81
5.15: Angular distributions of ^{6}Li, ^{7}Be and ^{10}B measured in the interaction of ^{12}C with ^{12}C at incident energies of 200 and 400 MeV. The beam energies and the fragments with their emission energies are given in the figures. The error bars reflect the statistical errors. 82
5.16: Comparison between the experimental data and the theoretical calculations of double differential cross sections of ^{11}B at the emission angle of 12º. The experimental data are given by the full circles with statistical error bars. The red histogram represents the overall contributions from nucleon coalescence. The green histogram is the complete fusion. The remaining histograms show contributions from the break-up fusion processes which are listed in table 5.1 [Mai07]. The solid-line black histogram represents the incoherent sum of all contributions. 84
5.17: Comparisons between the experimental data and the theoretical calculations of double differential cross sections of ^{8}B at different emission angles. The experimental data are given by the full circles with statistical error bars. The incoherent sums of all contributions are represented by the red histograms [Mai07]..... 86
5.18: See caption of figure 5.17. 87
5.19: Comparisons between the experimental data and the theoretical calculations of double differential cross sections of ^{10}B at different emission angles. The experimental data are given by the full circles with statistical error bars. The blue histograms represent the complete fusion (CF) and the red histograms represent the break-up fusion (BF) processes. The green histograms represent the reaction ^{12}C(^{12}C,^{10}B)^{14}N. The incoherent sums of all contributions are given by the black histograms [Mai07]. 88
5.20: See caption of figure 5.19. 89
5.21: Comparisons between the experimental data and the theoretical calculations of double differential cross sections of ^{11}B at different emission angles. The experimental data are given by the full circles with statistical error bars. The blue histograms represent the complete fusion (CF) and the red histograms

represent the break-up fusion (BF) processes. The green histograms represent the reaction $^{12}C(^{12}C,^{11}B)^{13}N$. The incoherent sums of all contributions are given by the black histograms [Mai07]. 90
5.22: See caption of figure 5.21. 91
5.23: Comparisons between the experimental data and the theoretical calculations of double differential cross sections of ^{12}B at different emission angles. The experimental data are given by the full circles with statistical error bars. The incoherent sums of all contributions is represented by the red histograms [Mai07]..... 92
5.24: See caption of figure 5.23. 93

LIST OF TABLES

2.1: Shows the low and high energy thresholds for different isotopes detected by the silicon detector telescope for the 200 MeV and 400 MeV runs. 11
2.2: NIM modules used to process the linear signals of the BCD. 20
2.3: NIM modules used to process the linear signals from the silicon detectors. 21
2.4: NIM modules used to process the logic signals of the Si detectors. 23
2.5: Scalers and pattern register input definitions for 200 MeV run. 27
3.1: Emission angles covered by the two detectors. 30
3.2: Calibration parameters for the Si (E_1) detector at a beam energy of 200 MeV. 34
3.3: Calibration parameters for the Si (E_1) detector used at the beam energy of 400 MeV. 35
3.4: Calibration parameters of the Si (E_2) detector at a beam energy of 400 MeV. 35
3.5: The parameters used to generate mass function spectra for the 200 MeV run. 38
3.6: The parameters used to generate mass function spectra between ΔE and E_1 detectors for 400 MeV run. 39
3.7: Parameters used to generate mass function spectra between E_1 and E_2 detectors for 400 MeV run. 39
3.8: Contains the angles where the background subtractions were performed for 200 MeV. 50
3.9: Target positions as a function of energy loss of the 8.87 MeV alpha and a ^{12}C target thickness. 54
3.10: Summary of all uncertainties from different sources for both BCD and silicon detector telescope. 55
5.1: Contains the reaction mechanisms and the break-up cross sections considered in the theoretical calculations. 84

CHAPTER 1

INTRODUCTION

1.1 Overview

The emission of clusters of nucleons, also called Intermediate Mass Fragments (IMF) is quite a common feature in heavy ion reactions [Gad03]. These clusters are defined as IMFs if they have a nuclear charge of $Z \geq 3$. It is expected that at beam energies around 10 MeV/n a transition in the reaction mechanism is taking place [Mag98], [Fuc94]. The energy region below 10 MeV/n is dominated by reaction mechanisms such as fusion-fission, quasi-elastic and deep-inelastic scattering where the mean field determines the interaction process [Fuc94], in particular these mechanisms are found to persist even at energy regions above 10 MeV/n but fading with an increasing projectile energy [Fuc94]. The projectile and target either fuse completely or collide inelastically, while at energies above 10 MeV/n the projectile might break-up and part of it fuses with the target nucleus [Mag98], [Fuc94].

The measurements of the present work were performed for a light system of $^{12}C + ^{12}C$ at incident energies of 16.7 MeV/n and 33.3 MeV/n. At these incident energies different processes to the ones considered at low beam energy have to be introduced. The experimental advantages of using light nuclei in the entrance channel is that the reaction products are detected with a low energy threshold, good mass and charge separation of ejectiles and good energy resolution.

A series of experiments has been conducted at iThemba LABS to study the different reaction mechanisms involved in the formation of IMFs. Beams of ^{12}C and ^{16}O were used to bombard different targets of mass number ranging from 60 to 200 [Gad03],

[Bec03]. These studies have shown that in addition to the fragments produced in the binary fragmentation of the projectile with about the beam velocity. The low-energy fragments with an energy range between 6 and 25 MeV/n observed in the energy and angular distributions suggested that they are predominantly produced as binary fragmentation and also by nucleon coalescence in complete and incomplete fusion of interacting ions [Bec03]. During nucleon coalescence the energy of the projectile or participant fragment is shared equally amongst the nucleons of the compound nucleus due to nucleon-nucleon interactions. After the statistical equilibrium is reached nucleons with the same momentum escape from the compound nucleus as clusters, known as IMFs. The above mentioned experiments were extended to a lighter system of $^{12}C + ^{27}A1$ and $^{27}Al + ^{12}C$ interactions at incident energy of few MeV/n [För07].

The experiments were performed in order to study the underlying reaction mechanisms involved in the production of IMFs. The main reason for these reactions was to separate the fragments from the binary fragmentation of the projectile and that of the target nucleus [För07]. This study showed that the IMFs were produced mostly as evaporation residues in complete fusion and break-up fusion reactions. These mechanisms were shown to account for most of the reactions observed in the interaction of two light nuclei at incident energies of a few tens of MeV/n. This energy range also corresponds to the Bragg Peak region (BPR) of energetic heavy ions interacting with thick materials.

The present experiment was performed using a ^{12}C beam on ^{12}C target at incident energies of 200 and 400 MeV. This experiment was initially intended to study spectra of C, N and O isotopes [Dla06]. However the spectra of IMF which are lighter than the projectile and target nuclei also form part of the particle identification spectra (PID). This thesis presents the energy spectra of $^{6,7,8}Li$, $^{7,9,10}Be$ and $^{8,10,11,12}B$ emitted in the interaction of ^{12}C with ^{12}C at incident energies of 200 and 400 MeV.

1.2 Reaction mechanisms

When two nuclei collide there are a few processes that could occur, amongst others the emission of Intermediate Mass Fragments (IMF). There are a number of

mechanisms that are responsible for the production of these IMFs. There are other reaction mechanisms not applied in the present analysis such as fusion-fission, quasi-elastic and deep in-elastic reactions. The fusion-fission process starts with the complete fusion of the projectile and target nucleus leading to a compound nucleus which decays by emitting photons or breakup into two heavy nuclei, which occurs if the energy of the compound nucleus exceeds the activation energy, which is the energy needed to overcome the fission barrier [Lil01]. The quasi-elastic and deep-inelastic reactions are the non-fusion processes [Bha94], [Rit85], which occur when the two nuclei have a grazing collision, that is when the two nuclei are deflected by the Coulomb field. These reactions are incomplete in the sense that the excitation energy deposited in the fragments emitted in these reactions is smaller than the total kinetic energy loss from the entrance channel, whereby the entrance channel kinetic energy is carried away by pre-equilibrium emission. In previous studies involving the interaction of ^{12}C and ^{16}O with different heavy targets [Bec03], [Gad03], and also in the interaction of ^{12}C with ^{27}Al [För05], [För07] showed that the IMFs were mainly produced in binary fragmentation processes and as evaporation residues in complete and incomplete fusion reactions. Based on earlier assessment of their applicability the mechanisms that can possibly play a role in the formation of the IMFs in the interaction of ^{12}C with ^{12}C at incident energies of 200 and 400 MeV are discussed as follows: nucleon coalescence through incomplete and complete fusion, projectile and target fragmentation, nucleon transfer, pre-equilibrium emission and evaporation. These mechanisms are described in the sections below.

1.2.1 Nucleon coalescence through complete and incomplete fusion

Complete fusion of the projectile with the target nucleus or the fusion of a participant fragment with the target nucleus after projectile break-up, referred to as incomplete fusion, creates a non-equilibrated excited nucleus [Gad03]. Complete fusion dominates at lower beam energies, whereby the overlapping of the two ions is slowed by their Coulomb repulsion. This leads to the energy of the projectile's nucleons transform into thermal energy when they are still forming a dinuclear system while a large part of the Coulomb potential energy is not re-transformed into nucleon kinetic

energy [Cav98]. At higher incident energies, the ions overlap fast and their nucleons may even increase their energy when they fall in the common potential well because the Fermi energy of the composite nucleus is greater than those of the projectile and target.

- **Complete fusion**

  The complete fusion process takes place when the projectile fuses with the target nucleus, in which full amount of energy and momentum is transferred from the projectile to the target nucleus leading to the formation of an excited compound nucleus.

- **Incomplete fusion**

  The incomplete fusion process occurs when the remaining part of the projectile and the target nucleus fuses after the initial colliding nuclei have emitted particles.

Nucleon coalescence occurs when the projectile or participant fragment fuses with the target nucleus, the energy of the projectile or participant fragment is shared equally among the nucleons of the compound nucleus due to interaction between the nucleons until the statistical equilibrium is reached. If the excitation energy is high enough the nucleons of the same momentum will start to escape from the compound nucleus as single entities or clusters of nucleons, until the compound nucleus reaches its ground state.

1.2.2 Pre-equilibrium emission

In the nucleon-nucleon collision a particle can be emitted either immediately after the interaction of the projectile with a nucleon or with a group of nucleons of the target nucleus, as a direct reaction, or after a long time by statistical decay of the compound nucleus [Gad92]. The difference between what is referred to as nucleon coalescence and pre-equilibrium emission of nucleons or clusters is that pre-equilibrium emission occurs before the energy of the projectile or participant fragment is shared equally among the nucleons of the compound nucleus, while nucleon coalescence occurs after

the statistical equilibrium is reached when the energy of the compound nucleus is shared equally amongst its nucleons. Pre-equilibrium emission increases with increasing incident energies.

1.2.3 Projectile and Target Fragmentation

According to the perturbative Serber approximation [Ser47] and [Gad99], the projectile break-up has a maximum probability at the energy corresponding to the beam velocity and a peak related to the momentum distribution of the observed fragments within the projectile. At the grazing angle, these spectra peak at an energy very close to the beam velocity. The spectra tend to fall-off rapidly on the high energy side and have long tails on the low energy side [Hus81]. Binary break-up is assumed to be a peripheral direct reaction by which the projectile divides into two fragments [Gad02]. In the present study the spectra of the break-up fragments are evaluated by folding the local plane wave approximation (LPWA) cross section with an exponential survival probability [Gad00], [Gad02]. The exponential survival probability was introduced because we assume that the ^{12}C ions probability of surviving a breakup or mass transfer reaction decreases exponentially with increasing projectile energy loss [Mai07], [Gad03]. After the break-up the fragments may either be emitted without further interaction with the target nucleus or may fuse with the target nucleus. The fragmentation of the target nucleus into two fragments could also occur, of which the other fragment may interact with the projectile. In this study the projectile or target nucleus may break-up into ^{11}B and a proton or ^{10}B and deuteron, where ^{11}B and ^{10}B are emitted without further interaction with projectile or target nucleus. The projectile or target nucleus may also break-up into ^{6}Li and ^{6}Li.

1.2.4 Evaporation

The capture of the projectile (complete fusion) or the capture of the participant fragments (incomplete fusion) by the target leads to the formation of an excited compound nucleus [Gad92], of which the energy is shared among all its nucleons. According to the Bohr independent hypothesis the decay of the compound nucleus is determined by its energy, angular momentum and parity [Gad92]. For this hypothesis to be valid a long time should elapse between the time of the formation and the time it

starts to decay, which could only be possible if the average excitation energy of an individual nucleon is less than its binding energy. Mainly light particles are emitted long after the fusion process by a statistical process similar to the evaporation of molecules from a liquid drop until the residual nucleus reaches its ground state by eventually emitting gamma rays. It is these evaporation residues which are detected as IMFs and mainly populate the low energy side of the measured spectra.

1.2.5 Direct reaction and nucleon transfer

Direct reactions take place in the time the projectile takes to traverse the target nucleus (typically about 10^{-22}s) [Hod97]. In these processes the projectile may interact either with a single nucleon, a group of nucleons or the whole nucleus leading to immediate emission. Elastic scattering is the simplest direct reaction, leaving the target nucleus in its ground state. In non-elastic reactions, the states of the residual nucleus which are excited have a simple structural relationship with the ground state of the target nucleus.

Inelastic scattering predominantly excites collective states, one-nucleon transfer reactions excite single particle states, and multi nucleon transfer reactions excite cluster states of the target nucleus. Some examples of these reactions mechanism in this work include, ^{11}B could be produced in the transfer of proton from the projectile to the target nucleus or vice versa, the transfer of proton produces ^{13}N or ^{16}O can be produced from a pick up of an alpha particle.

As in the case of elastic scattering, the cross-section for inelastic scattering and nucleon transfer reactions often have compound nucleus components at low energies. The cross-section for the compound nucleus components rises rapidly after the incident energy passes the threshold energy, attains a maximum and falls as other reaction channels become available. The direct process typically shows much less variation with incident energy.

1.3 Motivation of study

Studies involving the interaction of two light ions are still of great interest not only for basic research and knowledge of underlying reaction mechanisms, but also in application of fields such as hadron therapy and for radiation protection during space mission of the crew and their equipment. Another factor which is also important is the study of reactions induced by ^{12}C on nuclei of biological tissue [Mai07]. As was mentioned the $^{12}C + ^{12}C$ experiment was performed as an extension of the $^{12}C + ^{27}Al$ experiments. The aim of the present experiment was to study the reaction mechanisms involved in the production of IMFs emitted in the interaction of light nuclei.

The purpose of the present study is to extract the complete energy spectra of the produced $^{6,7,8}Li$, $^{7,9,10}Be$ and $^{8,10,11,12}B$ which contains the aspect about part of the spectra where all these reaction mechanisms dominate (see figure 1.1). And also to study the reaction mechanisms involved in the production of these IMFs, and the most important reason is to obtain information which might allow us to estimate the production of positron emitters ($^{10,11}C$, $^{12,13}N$, $^{13,14,15}O$, $^{17,18}F$, $^{17,18,19}Ne$, ^{21}Na) which are important for visualizing the beam during irradiation. The double differential cross sections were measured at different emission angles between 8º and 60º (see table 3.1). In previous studies [Bec03], it was shown that these light IMFs are produced due to the binary fragmentation and also due to nucleon coalescence through complete and incomplete fusion of the two ions.

In this work the theoretical model of binary fragmentation and nucleon coalescence through complete and incomplete fusion will be tested in light system. The theoretical calculations for ^{8}B, ^{10}B, ^{11}B and ^{12}B fragments emitted in the interaction of ^{12}C with ^{12}C at incident energy of 200 MeV will be presented in this work. Based on the calculations performed for incident energy of 200 MeV sufficient conclusions could be drawn for the reactions mechanisms involved and which contribute to the spectra at 400 MeV. The theoretical model used in this thesis to calculate the binary break-up and the nucleon coalescence from complete and incomplete fusion was developed at the University of Milan, Italy. The binary break-up is interpreted under the hypothesis of the Serber approximation [Ser47], and the local plane wave approximation (LPWA) [McV80]. Contributions from nucleon coalescence are calculated by using a

set of Boltzmann Master Equations (BME) [Cav01] in the FLUKA code. The FLUKA code is the nuclear transport and Monte Carlo code which was extended to include the BME and the LPWA for theoretical calculations.

In chapter 2 the experimental procedure is outlined and also the electronics used is explained. The procedure about the online data taking as well as the analysis of the data is explained in chapter 3. The theoretical model calculations are described in chapter 4 while chapter 5 presents the experimental results and also the comparison of the theoretical spectra with the experimental results. Chapter 6 presents the summary and conclusion of this work.

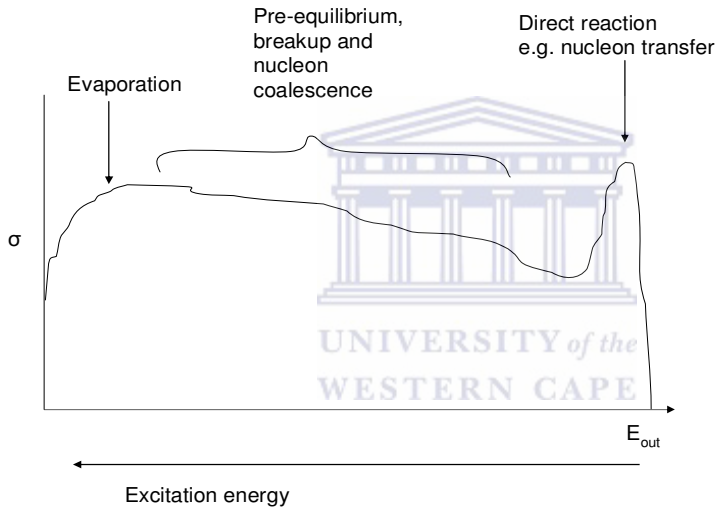

Figure 1.1: Schematic representation of complete energy spectra showing the contributions of reaction mechanisms as a function of emission energy and excitation energy.

CHAPTER 2

EXPERIMENTAL

2.1 Introduction

The original aim of this experiment was to measure the energy spectra of the IMFs with $Z \geq 6$ in the interaction of ^{12}C with ^{12}C at incident energies of 200 and 400 MeV. Nevertheless this also provided the energy spectra of $^{6,7,8}Li$, $^{7,9,10}Be$ and $^{8,10,11,12}B$ from which their double differential cross-sections were extracted. For the 200 MeV runs two silicon surface barrier (SSB) detectors were used. Double differential cross-sections were measured over an angular range between 8º and 60º. A third SSB detector was added for the 400 MeV measurements to obtain double differential cross-sections measured over an angular range between 8º and 70º. SSB detectors were used because of their good mass and charge resolution. SSB detectors were used to measure the high energy components of the IMF spectra while a Bragg curve detector (BCD) was employed to measure the fragments emitted at low emission energies. The ΔE-E technique was used for particle identification (PID) and also to separate the various isotopes of the specific species. Here the energy loss in the first ΔE detector is plotted against the energy that is deposited in the second E detector. The PID of the BCD was obtained by plotting the energy lost by a detected particle against the range it traveled inside the gas. In this chapter both the detectors as well as the electronic setup is described which were used to process the detector signals.

2.2 Silicon detectors

The silicon detector telescope consisted of two charge sensitive silicon surface barrier (SSB) detectors for the 200 MeV run while a third SSB detector was added for the

400 MeV run. For the 200 MeV run the SSB detector thicknesses were 57.6 µm and 1011 µm for ΔE and E_1, respectively. A 1017 µm thick E_2 detector was included in the telescope for the 400 MeV run. The SSB detectors were used because of their resistance to radiation damage, a very thin entrance window and they have a good charge, mass and energy resolution. The characteristic of these detectors are as follows: thin dead layers; energy loss distribution function; surface area of SSB; ability to operate at room temperature without excessive leakage current and the means to detect bound charged particle due to low intrinsic conductivity [Tyk95] [Sin68]. A ΔE detector was used to measure the energy loss of a charged particle passing through the detector for the 200 MeV run, the E_1 detector was used as a stopping detector, while for the 400 MeV run it was used as a transmission detector together with stopping E_2 detector. The energy thresholds of the detected fragments were obtained by using the ELOSS program [Jip84] and are shown in table 2.1 below. The thickness of the detectors defines the low and high energy thresholds.

2.3 Bragg curve detector

During the last few decades gas ionization chambers were used to register highly ionizing reaction products such as fission fragments and intermediate mass fragments (IMF) [And92]. There are several advantages that are associated with this kind of detector which include insensitivity to radiation damage, large solid angles, good nuclear charge resolution and it is easy to change the active chamber by varying the gas pressure. The registration of particles with higher energies and charge demands higher gas pressure while the voltage has to be increased to provide sufficient reduced strength necessary for the full charge collection. A thin foil is used as the cathode and entrance window in order to minimize the energy loss and decrease the low energy threshold of the particles entering the detector. The detector is called Bragg curve detector because the aim of the detector and associated electronic is to measure the Bragg peak of each ion stopping in the gas filled active volume of the detector [Ass82].

Table 2.1: The low and high energy thresholds for different isotopes detected by the silicon detector telescope for the 200 MeV and 400 MeV runs.

Fragments	Low energy threshold (MeV)	High Energy threshold	
		200 MeV	400 MeV
^{6}Li	17	96.5	140.8
^{7}Li	18	103.5	150.5
^{8}Li	18.8	109.5	159.5
^{7}Be	25	142.5	207.5
^{9}Be	26	158.5	231.5
^{10}Be	27	166	242.5
^{8}B	33	193.5	282.5
^{10}B	35.5	213.5	311
^{11}B	36	222	324.5
^{12}B	37	230.5	337

2.3.1 BCD construction

The detector (figure 2.1) is encapsulated by a stainless steel cylinder of 200 mm length and 55 mm internal diameter. The detector is designed to be an axial ionization chamber with the distance between the cathode and Frisch grid to be slightly larger than the range of the particle stopped [Gru82]. The entrance window is a Mylar foil of 1.010 µm thickness coated with 0.798 µm carbon on the inside which served as the cathode. The voltage between the cathode (ground) and the Frisch grid (positive) is divided by a resistor chain of 10 MΩ connected and interspaced by seven shaping rings. Thereby a homogeneous electric field over the active volume of the detector is maintained. The spacing between the Frisch grid and the anode defines the sampling region, which also determines the minimum range of the particles in the gas which are identified by the BCD. The cathode to grid and grid to anode distances are 160 mm and 20 mm, respectively. The Frisch grid consists of parallel tungsten wires of 2 µm thickness with 1 mm spacing. The Frisch grid is made to be as transparent as possible

to electrons in order to attract the electrons passing to the anode. The anode is a copper disk maintained at positive potential through the low impedance input of a preamplifier. While the Frisch grid voltage was at +1800 V, the anode voltage was at +2500 V. The gas pressure was regulated at 300 mbar throughout the measurements 99.5% pure isobutane (C_4 H_{10}) was used. The entrance window was tested to withstand a pressure up to 400 mbar.

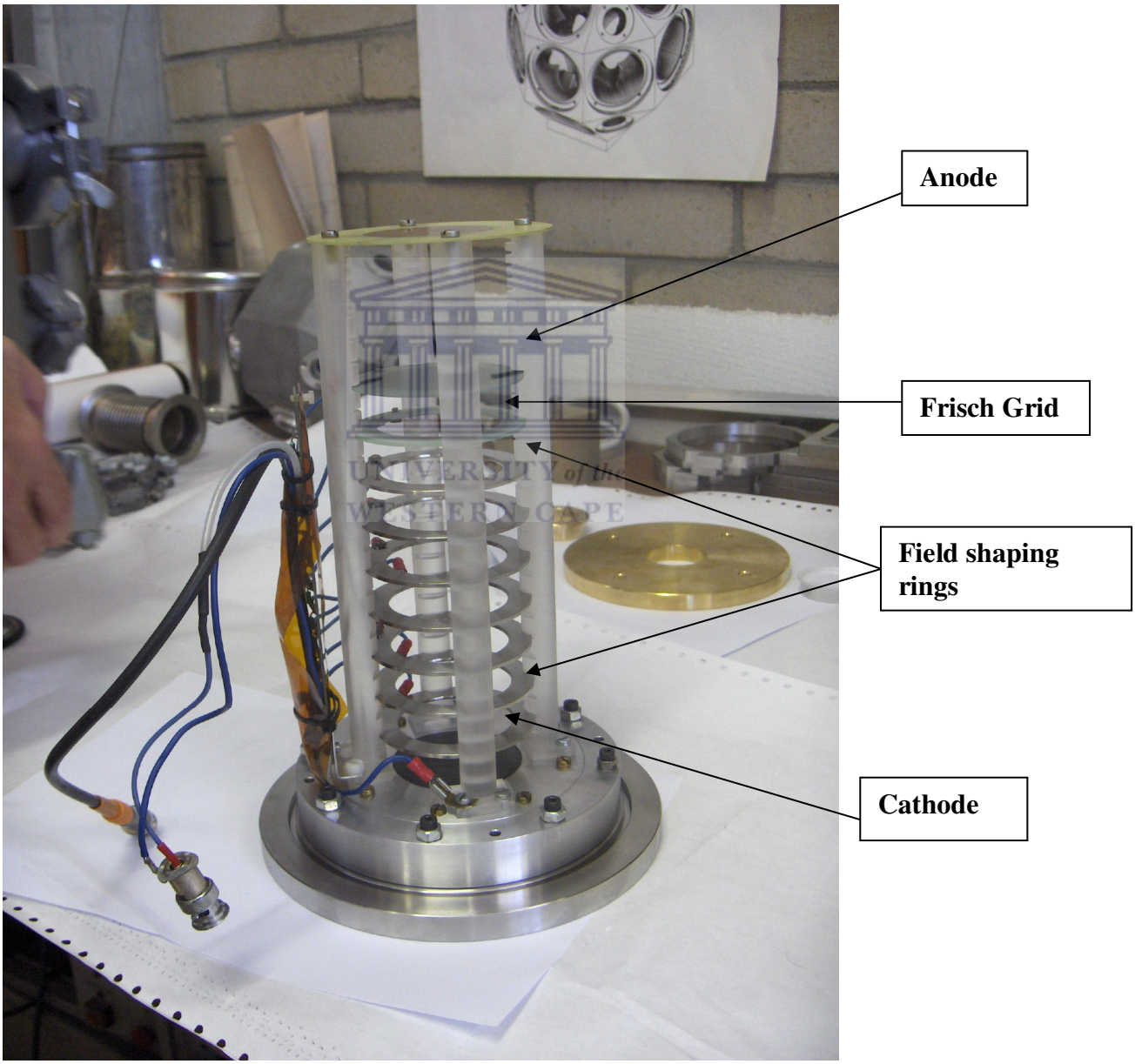

Figure 2.1: Photo of the active volume of the BCD.

2.3.2 Principle of operation

The principle objective of the detector is to the Bragg curve of each ion that stops in the gas (figure 2.2) by measuring the anode current as function of time [Ass82]. The length of the curve leads to the range of ions that stops inside the active volume, while the area beneath the curve is proportional to the energy lost along the track. The height of the Bragg peak is directly related to the nuclear charge (Z) of the stopped ion. From the above information we are in the position to deduce the relevant parameters of the detected ion; the nuclear charge Z, energy E and the mass. The detector operates on the principle of continuously sampling the ionization along the track left by the ion entering the detector. This sampling is achieved in the section of the detector defined by the Frisch grid. The particle enters the detector through the Mylar foil and moves along the detector, close to the axis and if its energy is low enough, will stop in the gas before reaching the Frisch grid. The electric field in the gas is parallel to the axis in the central region where the ionization track is created. When particles interact with the gas molecules inside the chamber they ionize the gas and produce ion pairs. These ion pairs are split, with the negative charges drifting towards the anode while the positive charges drift towards the cathode at a much smaller rate [Och96]. The anode current I_A is proportional to the total number of electrons distributed along the track inside the sampling space at a certain time t. By recording the current I_A (t) an image of the Bragg curve of the ionization dE/dx (x) assuming a linear dependence of t on x (constant drift velocity) is obtained. For good identification, the anode current must reproduce very closely the Bragg curve [Bar04]. The gaseous absorber quantity between grid and anode must be small, and the smaller the grid anode distance the smaller the grid screening efficiency, so the grid anode distance results in a compromise [Bar04].

The induced anode current is proportional only to the charge contained in the grid to anode gap and is given by [She85]

$$i(t) = \frac{v_d}{g} \int_{l}^{l+g} q^{-}(x,t)dx \qquad (2.1)$$

l = drift region length

g = grid to anode gap width

v_d = electron drift velocity

q^- = ionizing charges distribution of an electron at given time.

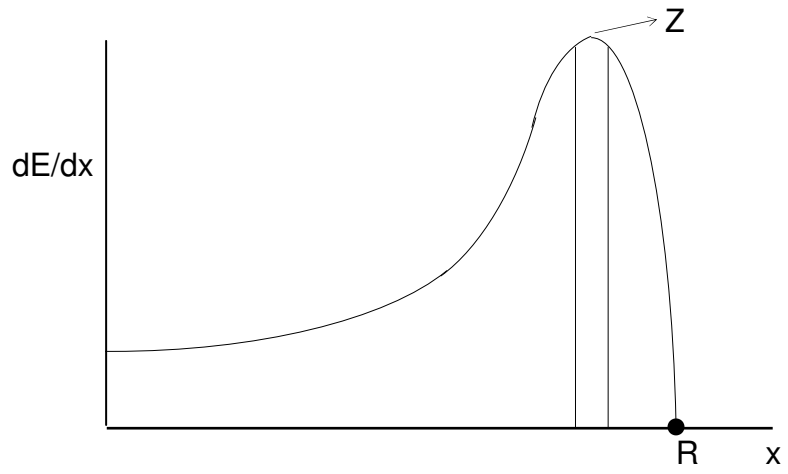

Figure 2.2: The Bragg peak of a particle that stopped in the active volume of the BCD with range R, nuclear charge Z, energy loss dE/dx over distance x inside BCD.

Isobutane ($C_4 H_{10}$) was chosen as the detecting gas for this type of detector for the following reasons [Bar04]: it has a high electronic stopping power that allows the detector to operate with relatively low gas pressure for reasonable counter length; the electron drift velocity is high and does not depend strongly on the applied reduced field in a given range; this large velocity limits electron recombination and attachment. When an ion is drifting in the gas it will collide with the gas molecules and start to lose energy from the collisions. When the remaining energy is smaller than about 1 MeV/nucleon the energy loss dE/dx increases rapidly with x and the Bragg peak is formed (see figure 2.2).

2.4 Experimental procedure

2.4.1 Beams

The iThemba LABS separated sector cyclotron (SSC) is capable of accelerating protons to energies of 200 MeV and can accelerate heavier particles to energies

between 30 and 40 MeV/nucleon. The SSC can accelerate carbon ions up to an energy of 35 MeV/nucleon. Figure 2.2 shows a layout of the iThemba LABS cyclotron facility. The Electron Cyclotron Resonance (ECR) ion source generates ^{12}C ions with different charge states depending on the beam energy. The ^{12}C ions had charge states of +3, +4 and +5 for the beam energies of 100 MeV, 200 MeV and 400 MeV, respectively. The ECR accelerates these to a few tens of keV and injects the ion beam into a Solid Pole Cyclotron (SPC2) which then accelerates the beam to a few MeV. From the SPC2 the ions are extracted and injected into the SSC which accelerates the ions to the required beam energy. On the three weekends of the experiment the 200 MeV as well as the 400 MeV ^{12}C beams were delivered into the A-line scattering chamber where the experiment was performed. The beam was then focused to a spot of less than 3 mm in diameter on the centre of the target which was mounted inside the scattering chamber.

2.4.2 Scattering chamber

The scattering chamber is about 1.5 m in diameter and is situated in the A-line vault and is equipped with two movable detector arms which can be placed at different angles relative to the beam direction. The aluminium target ladder is situated at the center of the scattering chamber, and it can hold five different targets arranged vertically. This arrangement allows a selected target to be positioned perpendicular to the beam. The target angle can also be changed by rotating the target ladder to allow the target to be visible to the full solid angle of the detector and to prevent the target frame and the magnet on the target frame from obstructing the detectors especially from an emission angle of 60º and larger. This changes the thickness of the target. The detector arms and the target ladder can be remotely controlled from the control unit in the data room or from inside the vault. The beam enters the chamber on one side and exits the scattering chamber to the beam stop on the opposite side. Another port which is above the incoming beam pipe is used as a viewing port and is sealed with lead glass. This viewing port is used for the closed-circuit television camera to view the beam spot and help to align the beam through the 3 mm diameter hole of a scintillating target mounted on the target ladder. There are other various ports for high voltage and power supply cables for the preamplifiers and also for the BNC cables used to transmit the detector signals from the vaults to the data room.

To obtain a good vacuum inside the scattering chamber, the o-rings were cleaned and greased properly. During the experiment the pressure inside the chamber was in the order of 10^{-5} mbar, which was achieved in the following steps. A rotary pump was used to pump down the chamber to a pressure of 1 mbar. Then a turbo pump was switched on and at a pressure of 10^{-3} mbar a cryogenic pump was also used to reach the eventual pressure of 10^{-5} mbar. To protect the silicon detectors while being in vacuum a holding bias of 10% of the operating bias was applied. The silicon detectors and BCD were fully biased as soon as beam was delivered and the experimental procedure was started.

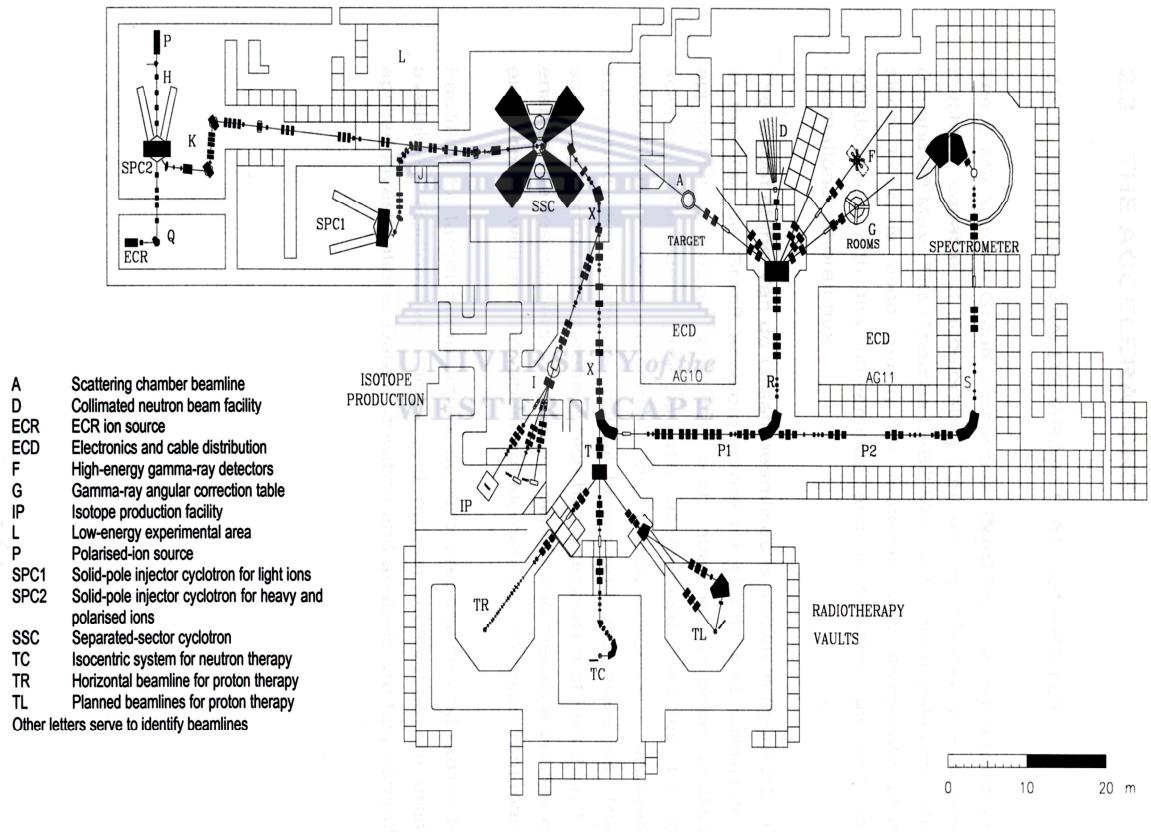

Figure 2.3: The layout of the cyclotron facility at iThemba LABS.

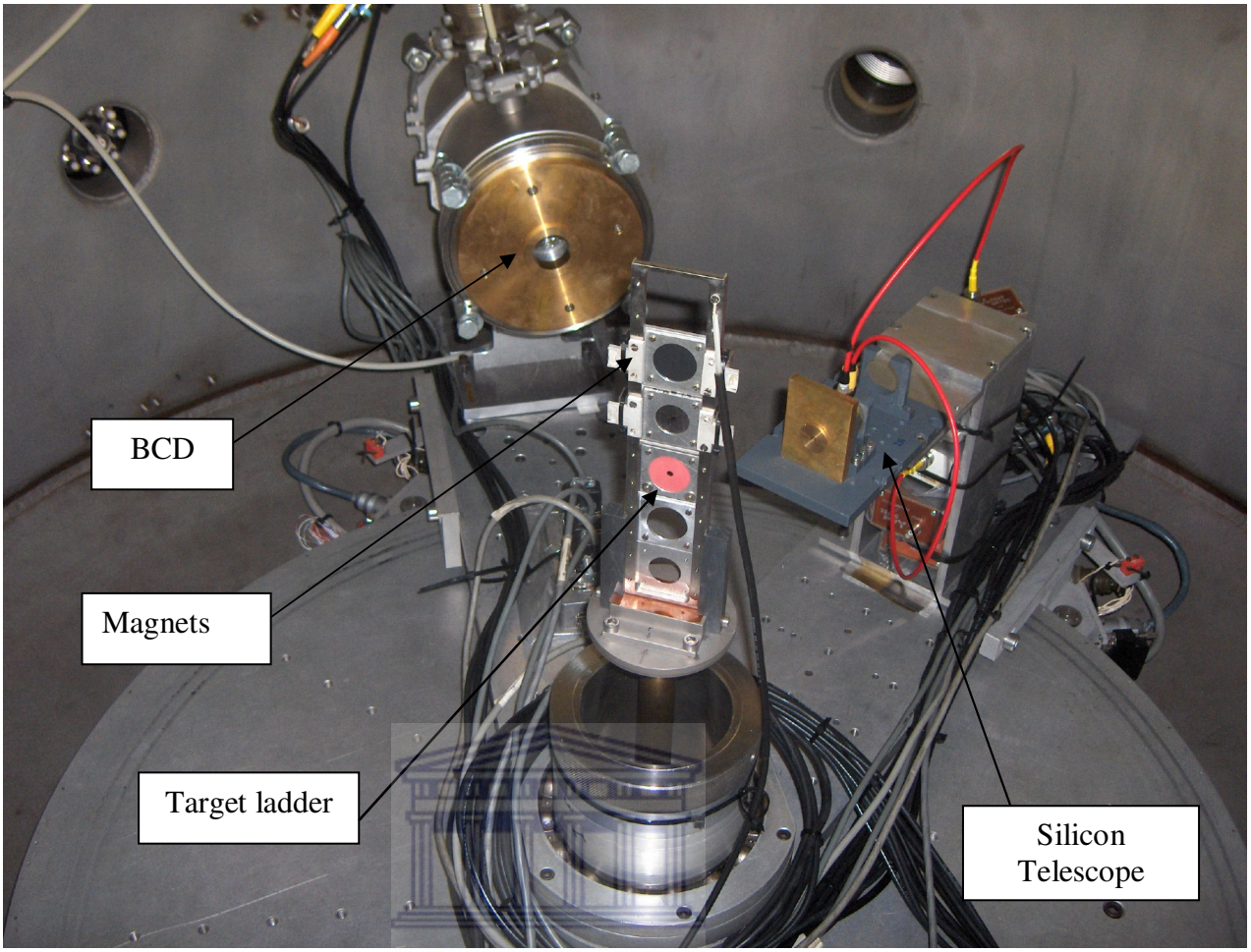

Figure 2.4: Photograph of the scattering chamber showing the target ladder, BCD and silicon detector telescope.

2.4.3 Targets

The targets were mounted on a target ladder which can house five different targets. Two ^{12}C targets of thickness of 100µg/cm^2 and 1mg/cm^2 were mounted on aluminium frames of 25 mm and 20 mm in diameter, respectively. The two corresponding empty frames were also mounted on the target ladder together with a ruby target. The ruby target was used to align the beam. The target ladder also consisted of permanent magnets on each side of the upper two targets and a power supply cable to supply the target ladder with a positive voltage to deflect away δ-electrons from reaching the detectors. The target thickness was confirmed by using the 8.78 MeV alphas from the ^{228}Th source inside the vacuum by placing first an empty target and then a ^{12}C target in front of the Si E_1 detector and recording the alpha peaks on the spectrum. The

thickness of the target was calculated from the measured energy loss by the alpha particles when passing through the target.

2.4.4 Setup of the detectors

The silicon detector telescope as well as the BCD were each mounted on rotatable arms inside the 1.5 m diameter scattering chamber which is situated in the A-line vault (figure 2.2). The silicon detector telescope was mounted on the other rotatable arm on the opposite side of the BCD. The Si detector telescope consisted of two silicon surface barrier (SSB) detectors for the 200 MeV run while a third SSB detector was added for the 400 MeV run. The detectors were arranged as follows. A 57.6 µm thick ΔE detector was followed by a 1011 µm thick SSB (E_1) detector for the 200 MeV run and an additional 1017 µm thick SSB (E_2) detector for the 400 MeV beam. A 10 mm thick brass collimator was used to shield the silicon detector telescope. A 8 mm thick collimator insert with a 8 mm diameter was fitted in the collimator hole. The solid angle subtended by the silicon detector telescope was calculated to be 1.1230±0.0012 msr. The BCD which is 20 cm long was mounted at a distance of 393.67 mm from the target ladder and was shielded by a 10 mm thick brass collimator. To avoid the fragments from hitting the shaping rings inside the active volume of the BCD, the effective collimator opening was reduced with a 32 mm diameter collimator insert. The collimator insert opening subtended a solid angle of 5.186±0.002 msr. The minimum forward angle relative to the beam that the BCD could reach, was 15^0.

The solid angles (ΔΩ) of both detectors were calculated from

$$\Delta\Omega = \frac{\pi r^2}{s^2} \qquad (2.1)$$

where,

r is the radius of the collimator insert

s is the distance from the target to the back of the collimator insert.

2.5 Gas flow system of the BCD

A crucial aspect for proper performance of the BCD is a reliable gas flow [Bar04]. The effect of the gas ageing can reduce the detection efficiency of the detector. When the gas is not refreshed continuously, after a short time the detection efficiency drops significantly, eventually even to zero. The admixture into isobutane remnant of electronegative gases which are attached to the vessel walls and hidden in the pores of various ports of the detector causes the detection efficiency to drop [Och96]. The mixture may capture the drifting electrons and prevents them from reaching the anode. This admixture can only be washed out by a constant flow of uncontaminated isobutane. An electronic unit is used to keep the pressure inside the detector constant, which according to the readout of a pressure sensor controls the opening fraction of the electromagnetic dosage valve.

In order to allow the gas to flow constantly inside the BCD the following procedure was adopted. Firstly, a by-pass linking the scattering chamber to the detector was opened to allow the pressure inside the detector to be the same as the operating pressure inside the scattering chamber. To avoid a sudden drop in the pressure which could cause the entrance window of the detector to break, the chamber was pumped down slowly by using a hand valve on the roughing pump, at a pressure of 10^{-4} mbar the by-pass linking the BCD and the scattering chamber was closed, thereby isolating the BCD from the scattering chamber's vacuum. The roughing pump of the gas supply system was then started to allow the gas to circulate through the BCD to the pump and an exhaust system. The gas bottle was opened to supply the isobutane gas. A needle valve as well as the supply valve on the pressure regulator control unit was opened to start the gas flow. After the BCD was filled with the gas, the gas regulator control unit was connected to a remote control unit in the data room. The pressure inside the BCD was kept at 300 mbar.

2.6 Electronics

The electronic set-up which was used to process the different detector signals of both the silicon detector telescope as well as the BCD are discussed in this section.

2.6.1 Detector signals and preamplifiers

The purpose of the preamplifiers is to convert a charged pulse to a voltage step. The charge-sensitive preamplifiers were mounted inside the scattering chamber to avoid noise pick-up of signals from both the BCD and the silicon detectors. The preamplifiers were mounted on the same rotatable arms where the detectors were mounted. Short BNC cables were used to connect the preamplifiers to the detectors. Events of interest were those that were in coincidence between the Si (ΔE) and Si (E_1) detectors and between Si (E_1) and Si (E_2) detectors as well as events of particles that stopped inside the active volume of the BCD. Both the linear as well as the logic signals were used to extract the events of interest.

2.6.2 Linear signal of the silicon detector telescope

This type of signal gives information about the energy and charge of the detected particle. The linear output signals from the preamplifiers of the silicon detector telescope were transmitted through standard 93Ω BNC coaxial cables to the individual amplifiers in the data room. From the individual amplifiers the signals were transmitted through the logic gates to the linear gate and stretcher (LGS) which sent the signals to the Analog-to-Digital Converter (ADC) module. Only the valid events which originated from coincidences between the ΔE and E_1 and between the $E_1$and E_2 detectors were allowed by the LGS to go through to the ADC (figure 2.3). Table 2.2 lists all the NIM modules used to process the linear signals.

Table 2.2: NIM modules used to process the linear signals of the BCD.

NIM modules	Models
Preamplifier	Built in-house
Spectroscopy amplifier	CANBERRA 2020
Delay Amplifier	ORTEC 427A
Flash Analog-to-Digital Converter (Flash ADC)	Caen V729A

Table 2.3: NIM modules used to process the linear signals from the silicon detectors.

Module	Model
Charged Sensitive Preamplifier	ORTEC 142B (ΔE) CANBERRA 2003BT (E)
Linear Gate and Stretcher	EG&G ORTEC 542
Spectroscopy Amplifier	CANBERRA 2021
Analog-to-Digital Converter (ADC)	CANBERRA 8077
Gate and Delay Generator	ORTEC 416

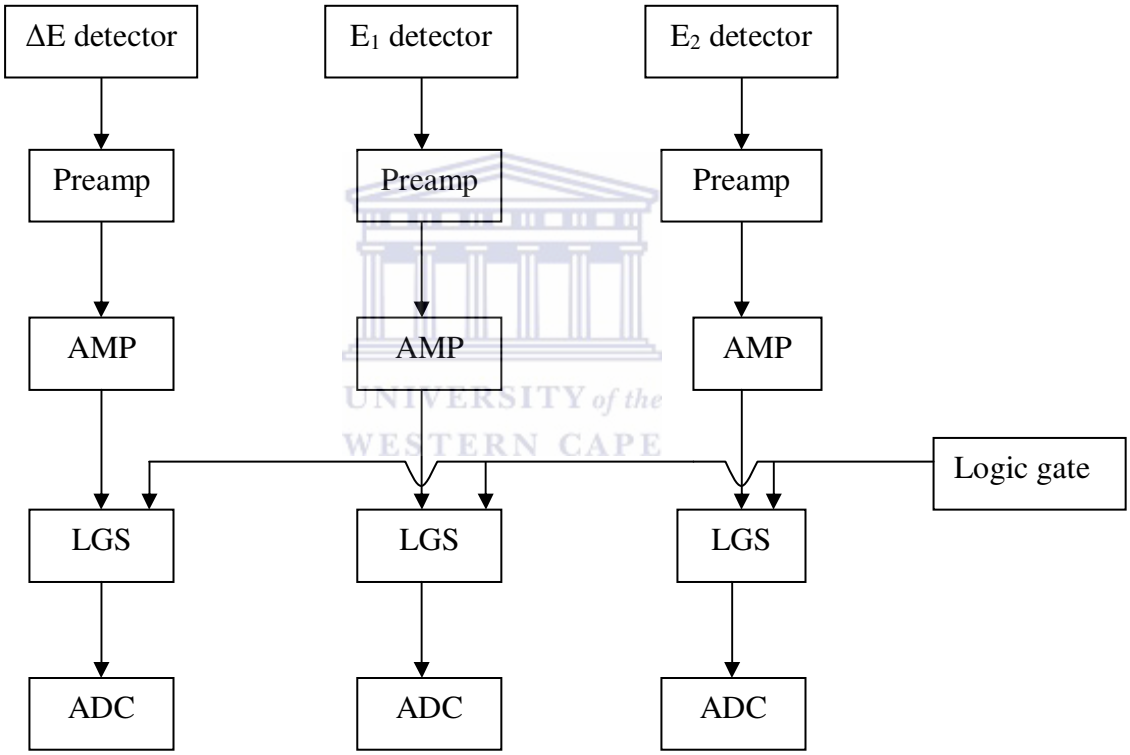

Figure 2.5: Electronic diagram used to process the linear signals from the Si detectors for the 400 MeV run.

2.6.3 Linear signal of BCD

The linear preamplifier output from the BCD was connected to a spectroscopy amplifier. The function of the spectroscopic amplifier is to shape the signal from the

charge-sensitive preamplifier to provide a pulse suitable for the data acquisition system and with a pulse height proportional to energy deposition. The shape of the linear signal contains the information about the energy, nuclear charge and the range of the detected particle. The signal from the amplifier was sampled and digitized by a Flash ADC. Table 2.3 shows all the NIM modules used to process the linear signal of the BCD.

2.6.4 Logic signals of the Si detector telescope

The logic or digital signals have a fixed shape and are used to count certain events or provide timing information of a detected particle. The digital signals have only two possible conditions 0 or 1. The logic signals of the Si detectors were transmitted from the preamplifiers to the data room through 50 Ω BNC cables. The timing filter amplifier (TFA) was used to shape and amplify the timing signals. The amplified timing signals were fed to a Constant Fraction Discriminator (CFD). The role of the CFD is to process the fast pulse and produce a logic signal when a constant fraction of the fast pulse peak amplitude is reached [Met04]. The output of the CFD was connected to a 4-fold logic unit (4FLU). The 4FLU was used to perform the AND operation between the ΔE and E_1 detector and between the E_1 and E_2 detector for the 200 MeV and 400 MeV runs, respectively. Since the E_1 detector was more stable and less sensitive to noise than the ΔE detector because of its thickness, the E_1 detector's timing signal provided the timing reference for setting up coincidences between the ΔE and E_1 detector for the 200 MeV run. For every ΔE-E_1 and E_1-E_2 coincidences, the corresponding logic pulse was fanned out to the Gate and Delay Generator (GDG), a rate-meter and a discriminator. The LGS received a logic signal from the GDG to open the gate for the linear signals to be processed by the ADC. Table 2.4 contains all the NIM modules used to process the Si detector logic signals.

Table 2.4: NIM modules used to process the logic signals of the Si detectors.

Modules	Models
Timing Filter Amplifier (TFA)	ORTEC 474
Constant Fraction Discriminator (CFD)	EG&G ORTEC 934
4 Fold Logic Unit (4FLU)	Le Croy 365AL
Discriminator (DISC)	ORTEC 436
Logic fan-in-out (FAN)	Le Croy Model 428F
Timer	ORTEC 719
Level Adaptor	Le Croy
Gate an Delay Generator (GDG)	ORTEC 416
QUAD Discriminator	Le Croy 821

2.6.5 Logic signal of BCD

The linear output signal from the preamp of the BCD was split to an amplifier and a timing amplifier. The timing amplifier was used to amplify the timing signal and its output was connected to a timing filter amplifier (TFA). From the TFA the signal was fed through a NIM FAN to amongst others the event trigger. The event trigger module sent an enable signal to the 4FLU to enable it to perform the AND operation between the enable signal and the timing signal from the NIM FAN. The stop signal required by the Flash Analog to Digital Converter (FADC) was generated from this AND operation. A GDG was used to delay the stop signal so that the stop signal arrives 1-2μs after the end of the corresponding BCD signal at the FADC. The stop signal was set to be a negative logic signal with a width of 400 ns. The BCD signal was digitized into 200 samples at a rate of 10 MHz by the FADC. The busy signal from the event trigger was fanned out by a logic fan to veto the AND operation and inhibit the scalers as shown in figure 2.7. All NIM modules used to process the logic signals of the BCD are of the same type as the ones used for the Si detectors.

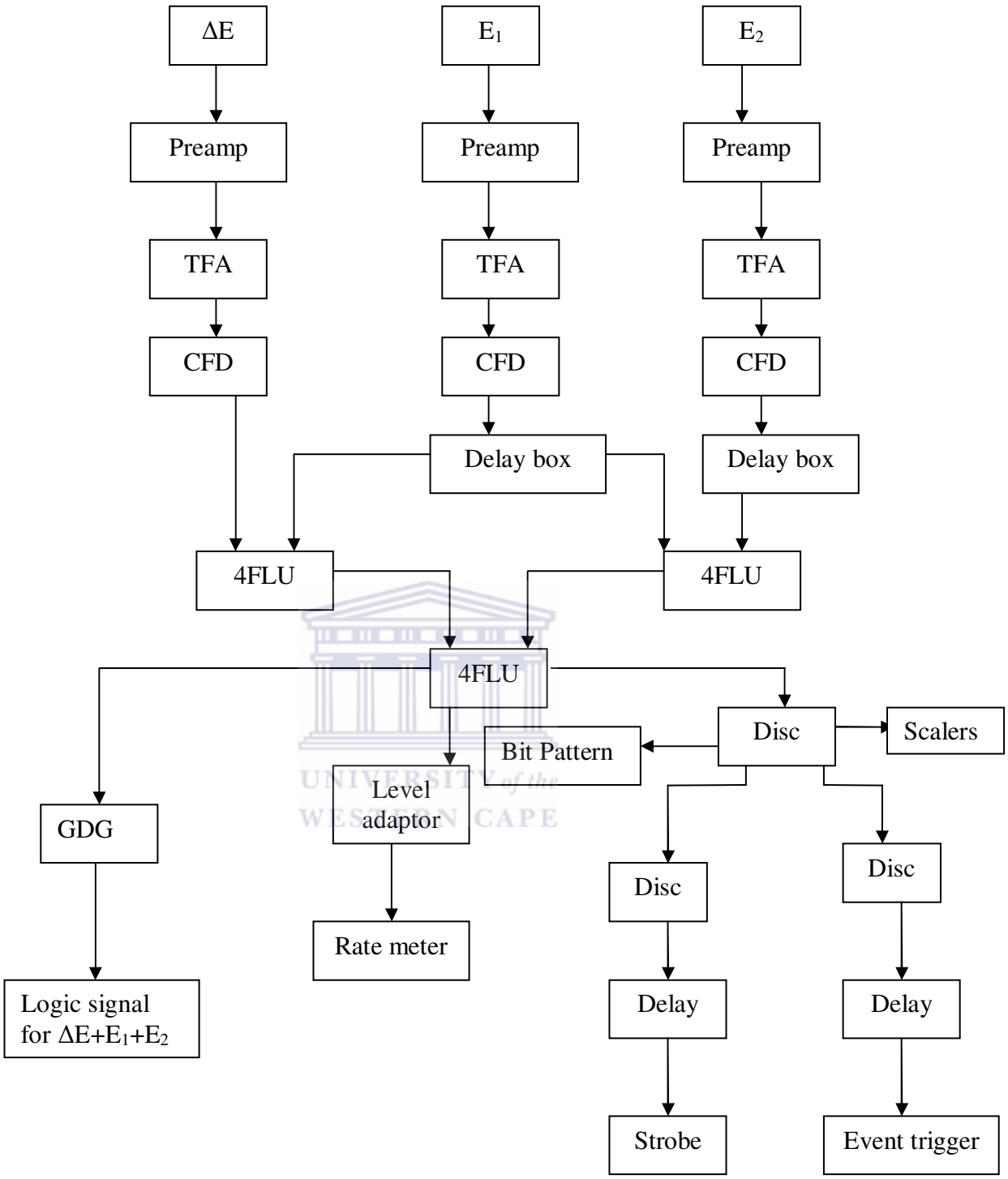

Figure 2.6: Block diagram used to process the logic signals of the Si detectors, here shown for the 400 MeV run.

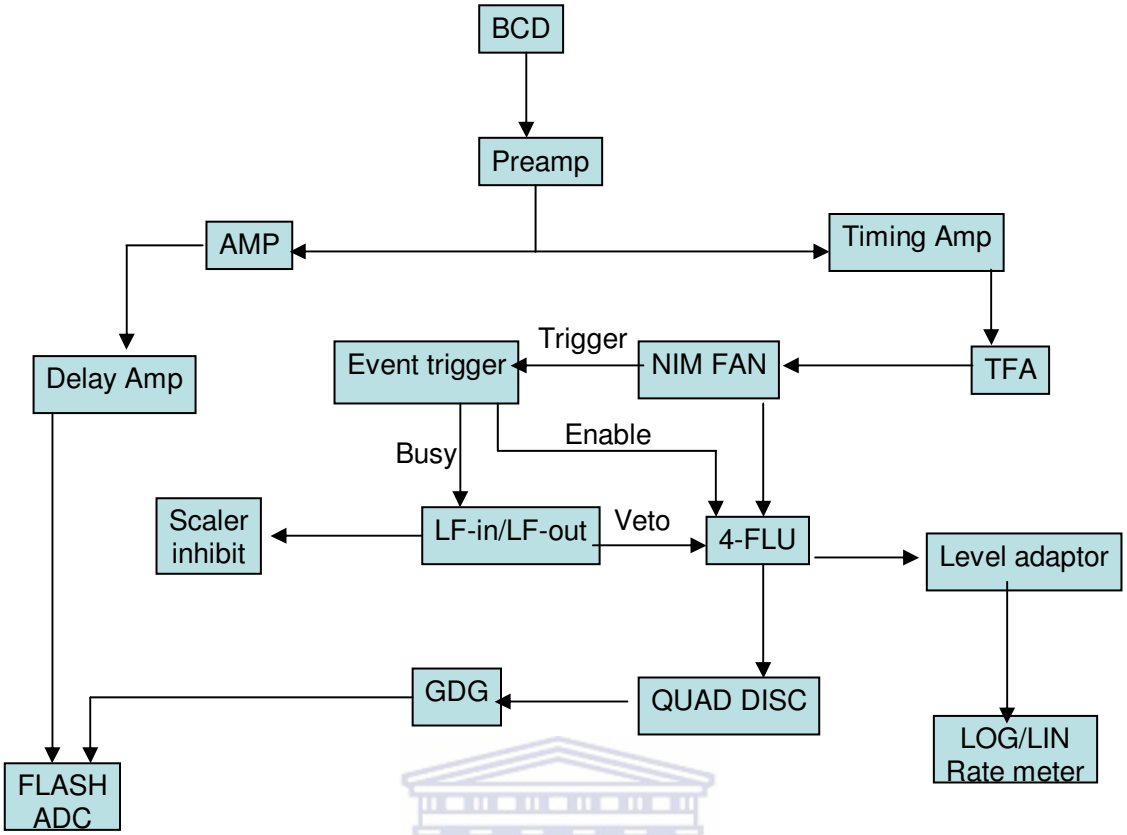

Figure 2.7: Block diagram used to process the logic signals of the BCD.

2.6.6 Current integrator

The amount of beam current registered at the beam stop was measured by connecting the beam stop to the Brookhaven Instrument Current integrator (BIC 1000C) module [Bas05]. This module allows the current integrator range to determine the number of pulses output for every unit of accumulated charge. The Brookhaven Instrument current integrator module provides digital output pulses with a width of 5µs.

2.6.7 Pulsers

The output of the Brookhaven Instrumental current integrator was connected to a timing single channel analyzer (TSCA), the positive output of the TSCA was connected to a constantly running timer. The pre-scaled signals from the timer are connected to a gate and delay generator (GDG). The GDG externally triggered the

pulse generators. The generated pulser signals for the ΔE, E_1 and E_2 detectors were fed to the test input of the charge sensitive preamplifiers. The output from the GDG was also connected to a discriminator and a pattern register (see 2.6.9). A method to determine the electronic dead time is to apply the pulse-to-pulse timing measurements [Den98], by recording the time distribution of the pulse from the amplifier. The ratio between the number of counts in a pulser spectrum and the measured number of counts from the inhibited scalers give the electronic dead time. The discriminator output was connected to both inhibited and uninhibited scalers (see 2.6.9).

2.6.8 Event trigger

Events of the Bragg curve, Si detector telescope and pulses accumulated during the logical requirement were accepted in an event trigger unit module which enters the computer through a CAMAC module. The computer accepted event 0 as a BCD event and event 1 as a Si detector telescope event through individual event trigger modules.

2.6.9 Pattern register

The pattern register was only used for valid events from the Si detector telescope. The timing signal of every valid event was fed into a pattern register. The strobe is a delayed signal which is needed for the pattern register to be read out. The pattern register is used to define every valid accepted event. For the 400 MeV run bits were set for each SSB detector event, and for the coincidence events between ΔE-E_1 and E_1-E_2 to avoid particles that punched through the E_1 detector to contaminate the ΔE-E_1 particle identification (PID) spectrum. The two input definitions for the pattern register are listed (see table 2.5).

2.6.10 Computer busy

For every event trigger signal that was accepted by the CAMAC event trigger modules a computer busy signal was generated. These signals were fanned out to veto part of the electronic circuit, block the LGS gates and also to inhibit certain scalers (section 2.6.12).

2.6.11 Clock

A constant running timer was connected to a timing single channel analyzer (TSCA). The TSCA output was connected to both an inhibited and an uninhibited scaler. The computer dead time can be determined by comparing the inhibited and uninhibited scalers.

2.6.12 Scalers

The scalers which were used to count the number of specific events are listed in table 2.5 for the 200 MeV run and in table 2.6 for the 400 MeV run.

Table 2.5: Scalers and pattern register input definitions for 200 MeV run.

Uninhibited Scalers	Inhibited Scalers	Bit	Pattern register
Telescope	Telescope	1	Telescope
Pulser trigger	Pulser trigger	2	Pulser
Clock	Clock	-	-
Current integrator	Current integrator	-	-
BCD	BCD	-	-

Table 2.6: Scalers and pattern register input definitions for 400 MeV run.

Scalers	Bit	Pattern register
Telescope	1	Detector telescope ΔE - E_1
Telescope	2	Detector telescope E_1 - E_2
Pulser trigger	3	Pulser
Telescope	4	Si ΔE detector
Telescope	5	Si E_1 detector
Telescope	6	Si E_2 detector

CHAPTER 3

DATA ANALYSIS

3.1 Introduction

After biasing all the detectors, the signals from all the detectors were first checked on an oscilloscope before taking data. The ΔE-E technique was used to extract the data for the Si detector telescope. In this technique the energy lost by the particle in the ΔE detector was plotted against the energy deposited in the stopping detector E. The events from the BCD were treated separately from the silicon detector telescope events. For the BCD the data was extracted by plotting the Bragg peak of the ions against the energy deposited by the ion inside the BCD. The double differential cross-section of different isotopes of Li, Be and B were extracted from the interaction. This chapter reports on how the data were analyzed.

3.2 Data acquisition programs

The XSYS software package which operates on the VAX system was used for online data acquisition as well as offline data replay [Gou83]. The online data acquisition was initiated by going through the following steps:

- Run XSYS
- Load the VME file
- Load COM and EVAL files respectively

The VME files are CAMAC and sub process files. The sub process XSORT reads the COM and the EVAL files and activate the sorting process [Pil96]. All the data areas for different histograms and one-dimensional and two-dimensional gates used by the EVAL sorting code are defined in the COM file. The EVAL file is an event analysis

program used to sort the data online as well as offline. The EVAL file contains algorithms needed to sort the events and increment the spectra according to the event types.

3.3 Online data taking

The online data taking was initiated by focusing and aligning the beam by using a ruby target which has a 3 mm diameter hole. Once the beam was focused XSYS was started as discussed in section 3.2. The beam halo was monitored by comparing the count rate produced from the empty frame targets with the count rate produced from the corresponding ^{12}C targets. A background rate of less than 10% was acceptable for data to be taken from the interaction of ^{12}C with ^{12}C target. The target that was used for data taking has a thickness 100 $\mu g/cm^2$. Data were collected for a period of one hour for every run. Background runs of 5 to 10 minutes were performed every two hours. The background was monitored for each emission angle for possible background subtraction. The BCD was positioned over an angular range between 15° and 60° and the silicon detector telescope was positioned over an angular range between 8° and 60° (see table 3.1). The pressure inside the BCD was kept at 300 mbar throughout the experiment. To get a good mass resolution in the PID spectrum the shaping time on the spectroscopy amplifier of the ΔE and E_1 detectors were optimized. The silicon detector telescope was used to measure the energy spectra of fragments emitted with high energies while the BCD was used to measure the energy spectra of the fragments emitted with low energies. The dynamic ranges of these detectors were largely limited by their low and high energy thresholds (see table 2.1). To obtain clean PID spectra with the Si detector telescope for the 400 MeV the bit patterns were set for each detector and also for the coincidences between ΔE-E_1 and between E_1-E_2 (see table 2.6).

Table 3.1: Emission angles covered by the two detectors.

Detectors	Emission angle
Si detector telescope	8º, 10º, 12º,15º,17º, 20º, 25º, 30º, 35º, 40º, 45º, 50º, 55º, 60º
BCD	15º, 17º, 20º, 25º, 30º, 35º, 40º, 45º, 50º, 55º, 60º

3.4 Offline data replay

The data replay was performed by extending the COM and EVAL files used for the online data acquisition. The COM and EVAL files were modified in order to accommodate all the additional gates and data areas. Separate COM and EVAL files were created for the replay of the data obtained with the Si detector telescope and the BCD.

3.5 Energy calibrations

This section describes the methods followed to calibrate the detectors for both incident energies of 200 MeV and 400 MeV.

3.5.1 Si ΔE detector

The energy calibration of the 56.7 μm thick ΔE detector was performed once for both beam energies of 200 MeV and 400 MeV. Since this detector was not thick enough to stop all the alpha particles emitted from the ^{228}Th source, it was calibrated using also the calibration of the Si (E_1) detector. The energy loss of Li, Be and B isotopes in the ΔE detector was calculated using the ELOSS program [Jip84]. This calculated energy loss was then plotted against the calibrated energy in the E_1 detector. The calculated Li, Be and B loci were fitted to the measured PID spectrum by multiplying them by a certain factor. That factor was then taken to be the gradient of the calibration for the ΔE detector. Figure 3.1 shows the calculated loci fitted to the experimental ΔE-E spectrum.

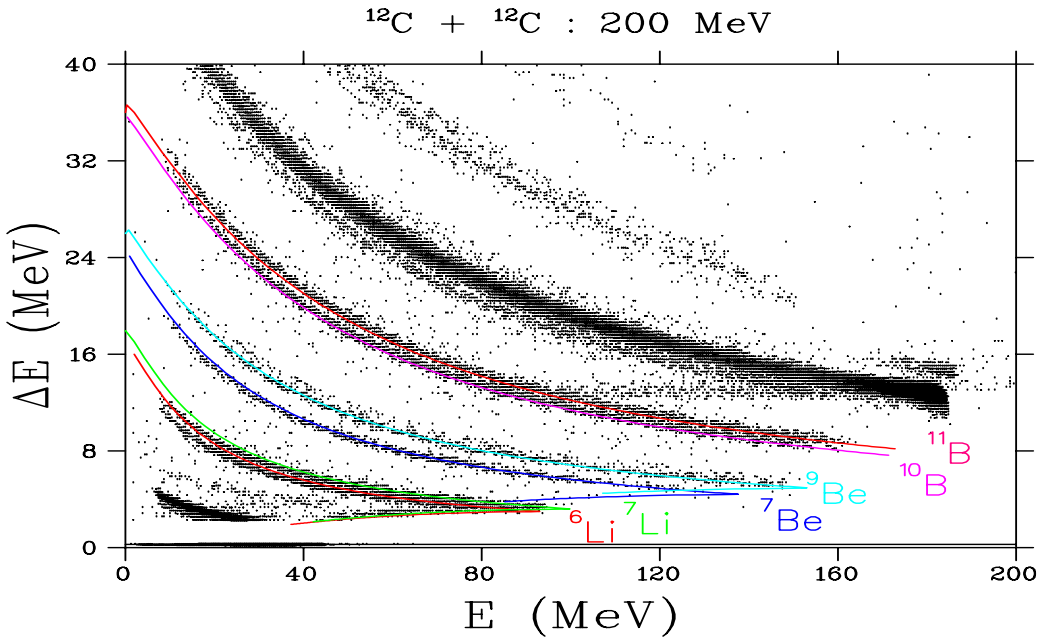

Figure 3.1: Loci of the Li, Be and B isotopes calculated by ELOSS program curves overlaid onto the experimental ΔE-E spectrum.

3.5.2 Si (E_1) Detector for 200 MeV

The E_1 detector was calibrated for a high energy as well as a low energy response. The low energy calibration of the E_1 detector was performed inside the scattering chamber by placing a ^{228}Th source in front of the detector. The alpha particles emitted from the ^{228}Th source were stopped in the detector. From the energy spectrum of the E_1 detector all alpha energy peaks and the corresponding channel numbers were identified (figure 3.2). The high energy part of the detector response was calibrated by elastically and inelastically scattered ^{12}C at different forward scattering angles. The peaks corresponding to the ground and the first excited state of ^{12}C were identified together with their channel numbers at different angles ranging between 8° and 17° (see figure 3.3). The energies corresponding to these peaks were obtained by using the value of the beam energy as well as KINMAT program. The energy values were plotted against the channel number. The gradient and offset parameters of the detector were determined by a linear fit. The calibration for this detector was confirmed by comparing the high energy peak of the calibrated spectra with the calculated values obtained with the KINMAT program considering the energy loss in the Si ΔE

detector. Figure 3.4 shows the calibration curve of the detector. Table 3.2 shows the calibration parameters for this detector.

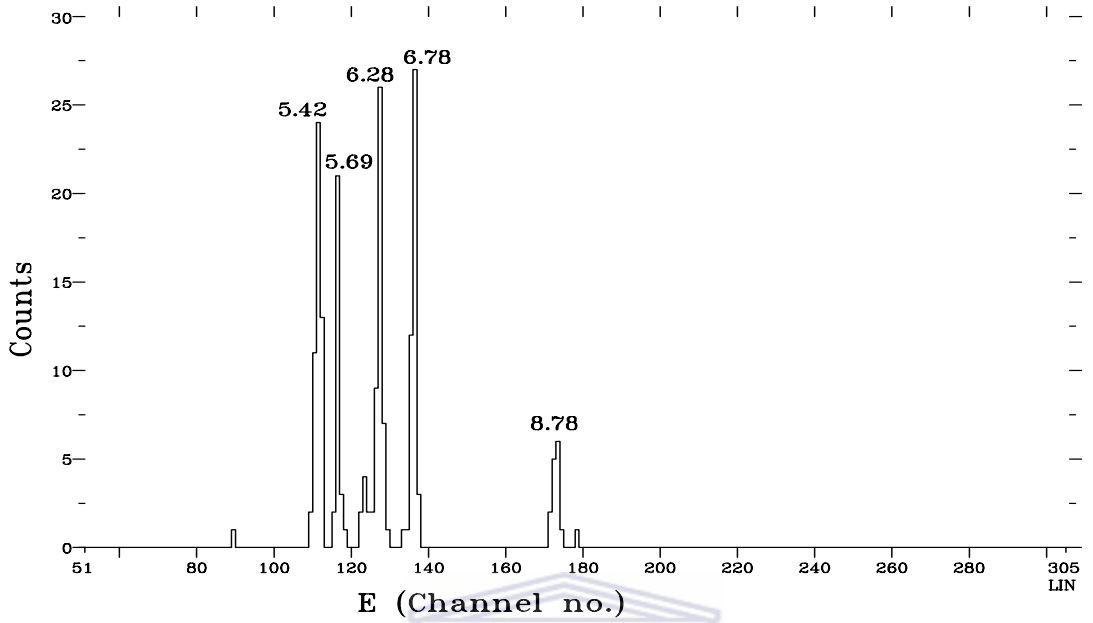

Figure 3.2: Typical energy spectrum of the alpha particles from a ^{228}Th source measured with the Si (E_1) detector. Energies are given in MeV.

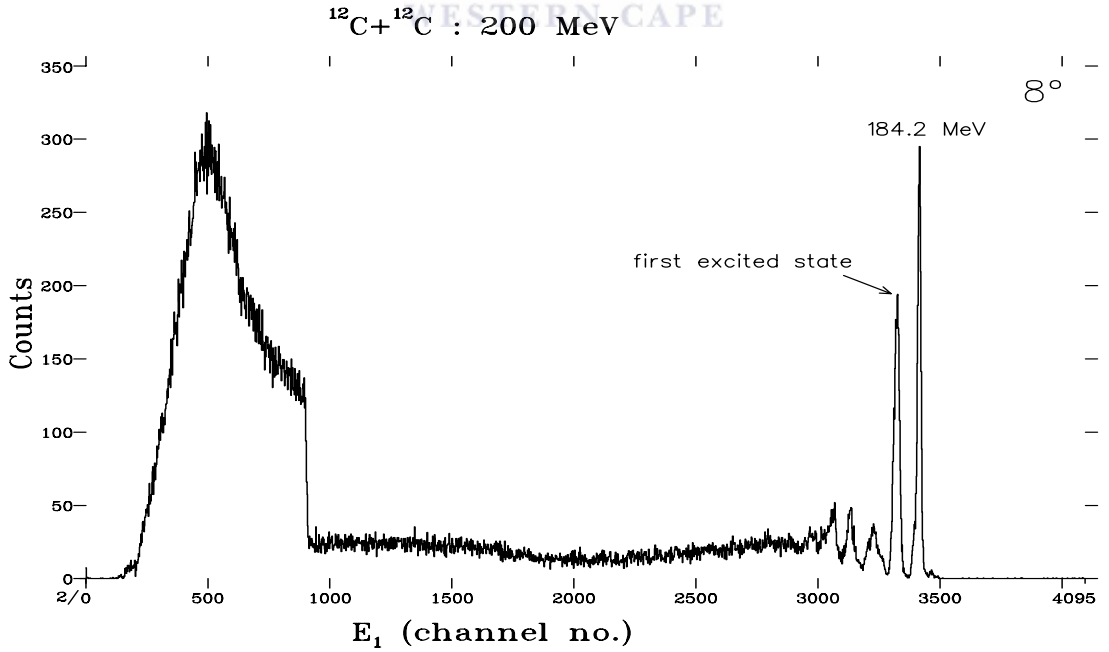

Figure 3.3: Raw energy spectrum used to calibrate the Si (E_1) detector using a 200 MeV ^{12}C beam.

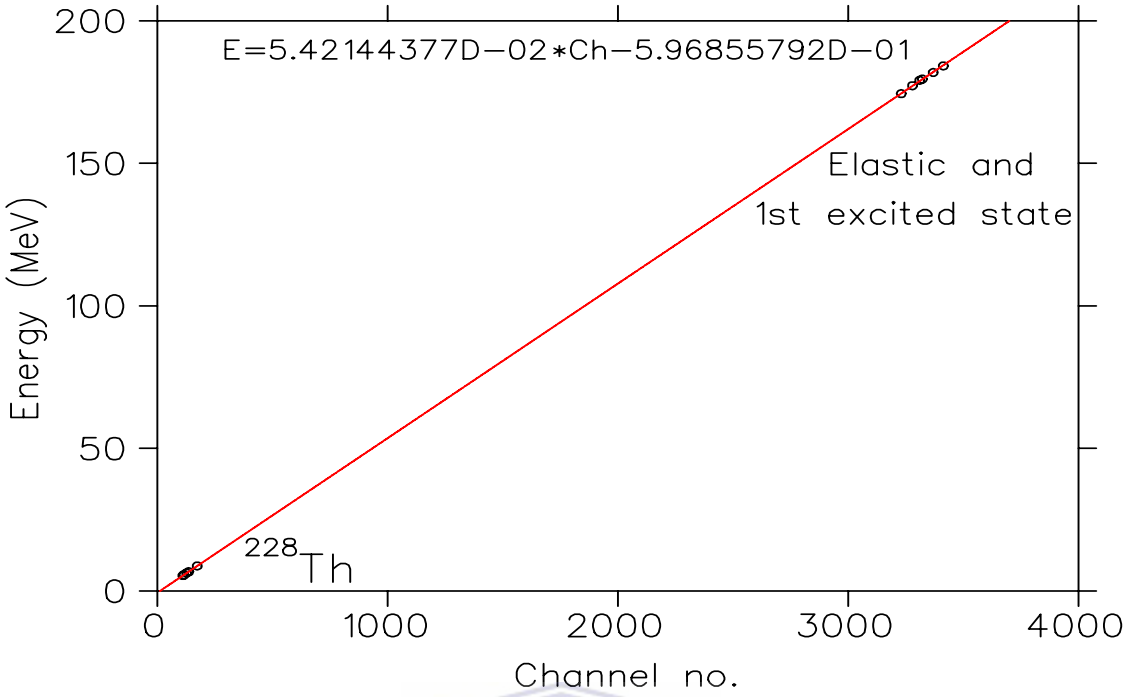

Figure 3.4: The calibration curve for the Si E_1 detector showing the straight line fitted through the high energy (discrete states) as well as the low energy points (alpha particles from ^{228}Th source) at 200 MeV ^{12}C beam.

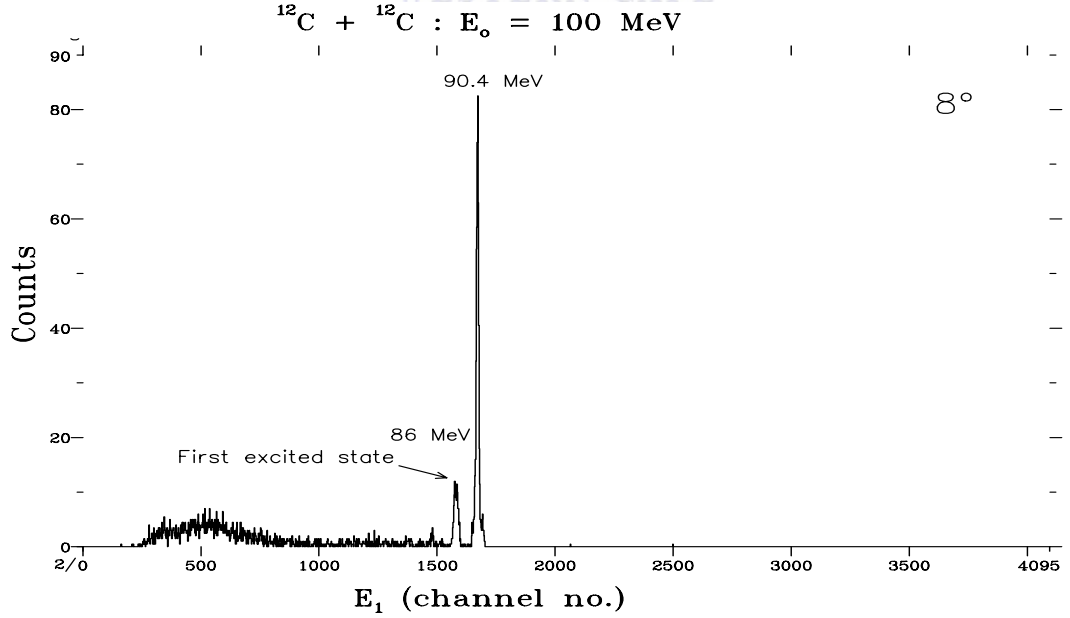

Figure 3.5: Raw energy spectrum used to calibrate the Si (E_1) detector for 400 MeV ^{12}C beam using 100 MeV ^{12}C beam.

Table 3.2: Calibration parameters for the Si (E_1) detector at a beam energy of 200 MeV.

Parameters	Values
Slope	$5.42144377*10^{-2}$
Offset	$5.96855792*10^{-1}$

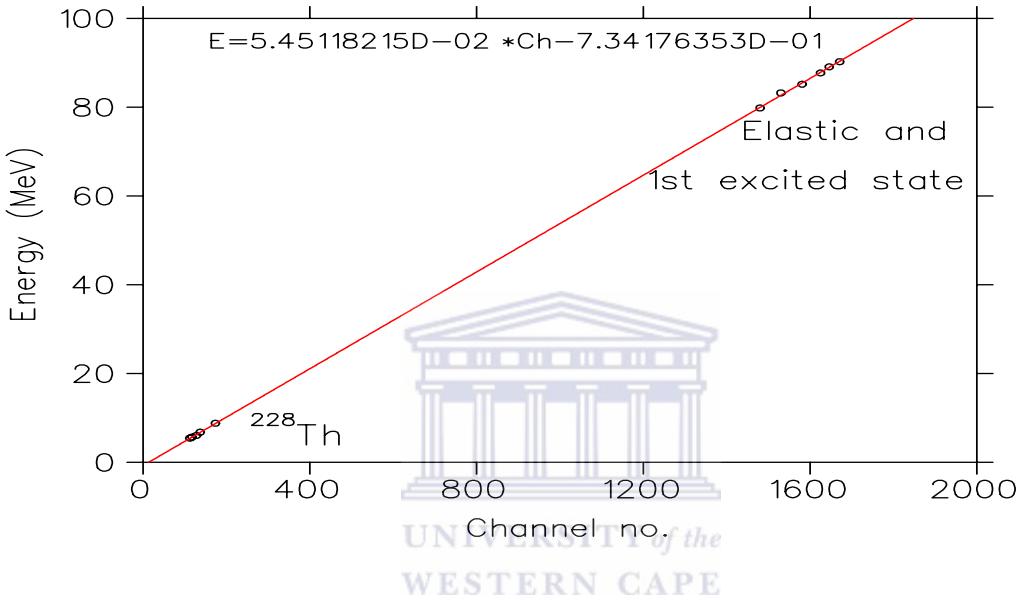

Figure 3.6: The calibration curve for the Si E_1 detector showing the straight line fitted through the high energy (discrete states) as well as the low energy points (alpha particles from ^{228}Th source) at 400 MeV ^{12}C beam.

3.5.3 Si (E_1) detector 400 MeV

The calibration for a low energy response was also performed with the alpha particles from a ^{228}Th source. In the case of the high energy response the calibration was performed using a 100 MeV ^{12}C beam at different angles ranging between 8° and 12°. The elastic peaks and the first excited state peaks of the ^{12}C were identified with their corresponding channel numbers (see figure 3.5). The alpha energies and the calculated elastic peak energies were plotted against the corresponding channel number. The offset and the slope parameters were determined from the linear relationship. Figure 3.4 shows the calibration curve of this detector while table 3.3 contains the calibration parameters for this detector.

Table 3.3: Calibration parameters for the Si (E_1) detector used at the beam energy of 400 MeV.

Parameters	Values
Slope	$5.45118215*10^{-2}$
Offset	$7.34176353*10^{-1}$

3.5.4 Si (E_2) detector 400 MeV

The calibration of the 1017 μm thick detector was also done for the detector response at low and high energies. The low energy calibration was performed by using alpha particle as discussed in section 3.5.2. The high energy calibration was also performed as described in section 3.5.3 using the 400 MeV ^{12}C beam. The alpha energies and the calculated energies of the elastic peak were plotted against their corresponding channel numbers. The energy loss in the Si ΔE detector and the Si E_1 detector had to be taken into consideration when calculating the energies of the elastically scattered ^{12}C. The offset and the gradient parameters of the detector were determined from the linear relationship. The calibration curve of this detector is shown in figure 3.8. Calibration parameters are listed in table 3.4 below.

Table 3.4: Calibration parameters of the Si (E_2) detector at a beam energy of 400 MeV.

Parameters	Values
Slope	$5.41028122*10^{-2}$
Offset	$5.60101818*10^{-1}$

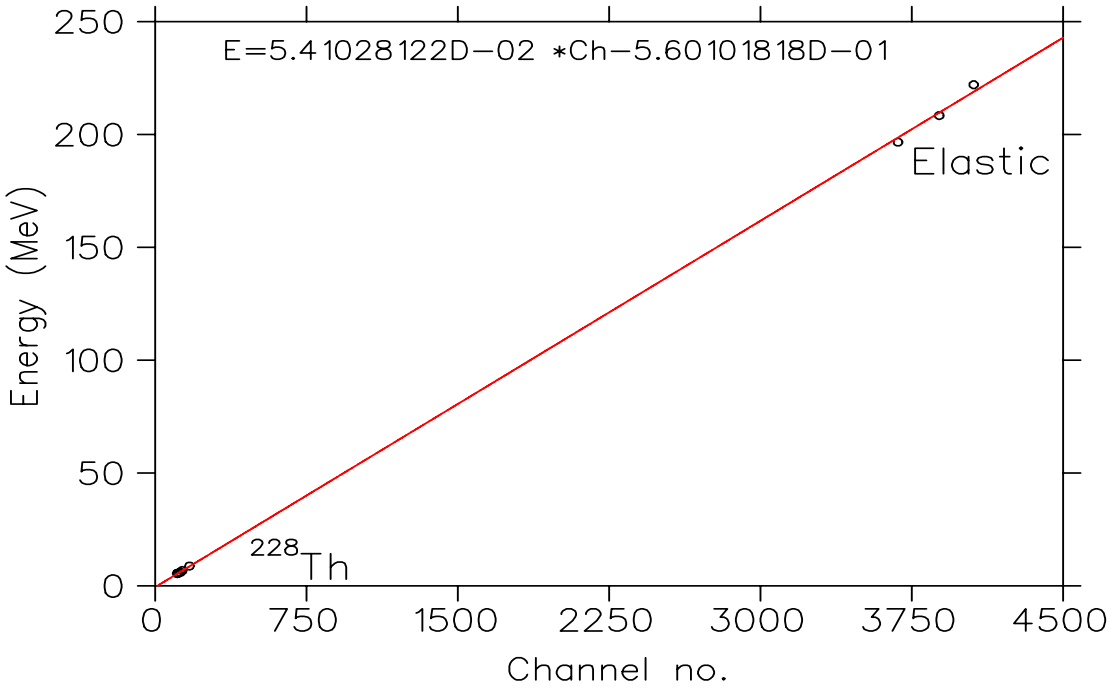

Figure 3.7: The calibration curve for the Si E_2 detector showing the straight line fitted through the high energy (discrete states) as well as the low energy points (alpha particles from ^{228}Th source) at 400 MeV ^{12}C beam.

3.5.5 Bragg curve detector

The BCD was calibrated inside the scattering chamber by using the alpha particles emitted from a ^{228}Th source. The source was placed in front of the detector close to the entrance window. The detector could only fully resolve the alpha particle emitted with energy of 8.78 MeV. Figure 3.8 shows the energy spectrum of the alpha particles detected by the BCD. The channel number corresponding to this energy was identified. The gradient parameter of the detector was determined by a linear relationship. The calibration was confirmed by comparing the highest energy peak with the high energy threshold calculated using the ELOSS program [Jip84].

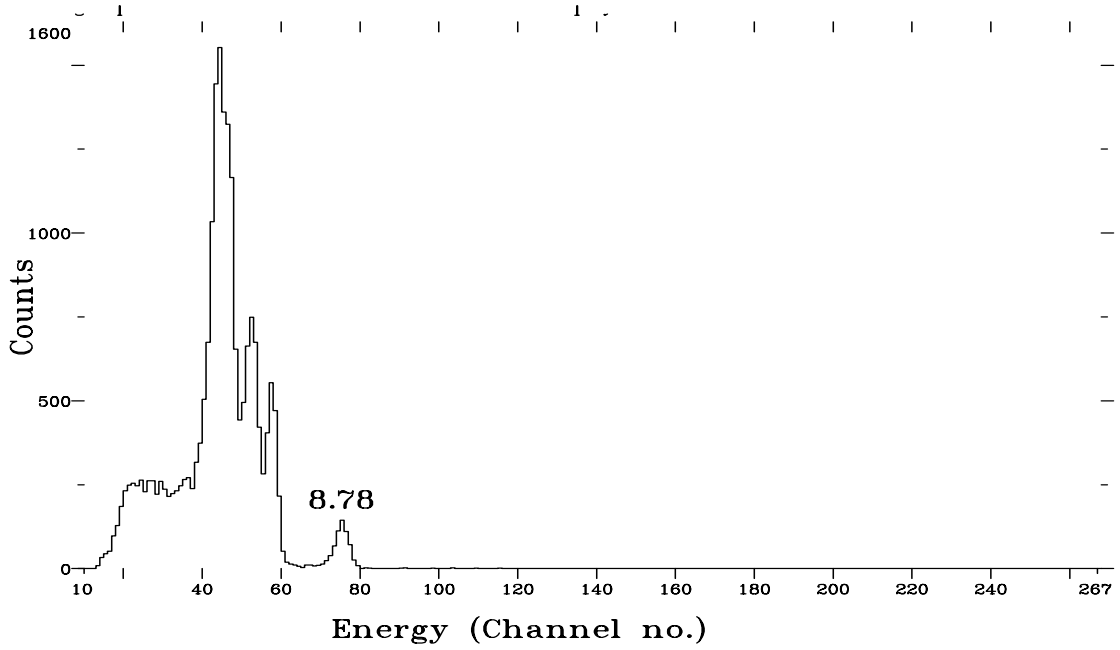

Figure 3.8: An energy spectrum of the alpha particles from a ^{228}Th source detected by the BCD. The only energy which is fully resolved is the 8.78 MeV energy line.

3.6 Particle Identification

After confirming the calibration of the detectors, the standard ΔE-E technique was used to identify and separate the charged particles registered by the silicon detectors. For the BCD the height of the Bragg peak of the ions that stop inside the active volume of the BCD was plotted against the total kinetic energy of the detected particle. The following sections describe how the particle identification (PID) was done and show the raw PID and mass function spectra.

3.6.1 Silicon telescope

Separation of isotopes and particle identification of the charged particles detected in the silicon detector telescope were obtained by using the standard ΔE-E technique. For the 400 MeV beam two PID spectra were generated between Si ΔE detector and Si E_1 detector and also between Si E_1 detector and Si E_2 detector. Figure 3.9 shows a typical two dimensional PID spectrum obtained with the Si detector telescope with gates set around the loci of lithium, beryllium and boron for the 200 MeV run, while

figures 3.10 and 3.11 show the PID spectra obtained with the Si (ΔE-E_1) and (E_1-E_2) detector, respectively, for 400 MeV run.

Mass functions were generated from these gated PID spectra for each specie in order to separate different isotopes of Li, Be and B. These mass functions were generated by using the following formula [Mud05]. Figures 3.12-3.20 show the mass function spectra with gates set around the loci of Li, Be and B isotopes at 200 and 400 MeV.

$$MF = \left[(E_B + E_A)^P - (E_B)^P \right] * M_s + M_o \qquad (3.1)$$

where,

E_B is the energy deposited in E_1 detector

E_A is the energy lost in ΔE detector

P is a constant

M_s is the slope factor used to optimize the position of the loci in the mass function spectra

M_o is an offset factor and was also used to optimize the position of the loci in the mass function spectra.

Tables 3.5, 3.6 and 3.7 contain the values of the parameters that were used to generate the mass functions for Li, Be and B both for the 200 MeV beam and the 400 MeV beam, respectively. The energy spectra of Li, Be and B isotopes were extracted from the gates set around the loci in the mass function spectra.

Table 3.5: The parameters used to generate mass function spectra for the 200 MeV run.

Fragments	M_s	M_o	P
Lithium	1.5	0.0	1.78
Beryllium	1.8	-400	1.8
Boron	1.8	-1200	1.8

Table 3.6: The parameters used to generate mass function spectra between ΔE and E_1 detectors for 400 MeV run.

Fragments	M_s	M_o	P
Lithium	1.8	0	1.8
Beryllium	1.8	-400	1.8
Boron	1.8	-600	1.8

Table 3.7: Parameters used to generate mass function spectra between E_1 and E_2 detectors for 400 MeV run.

Fragments	M_s	M_o	P
Lithium	1.35	-100	1.4
Beryllium	1.5	-300	1.3
Boron	1.4	-700	1.3

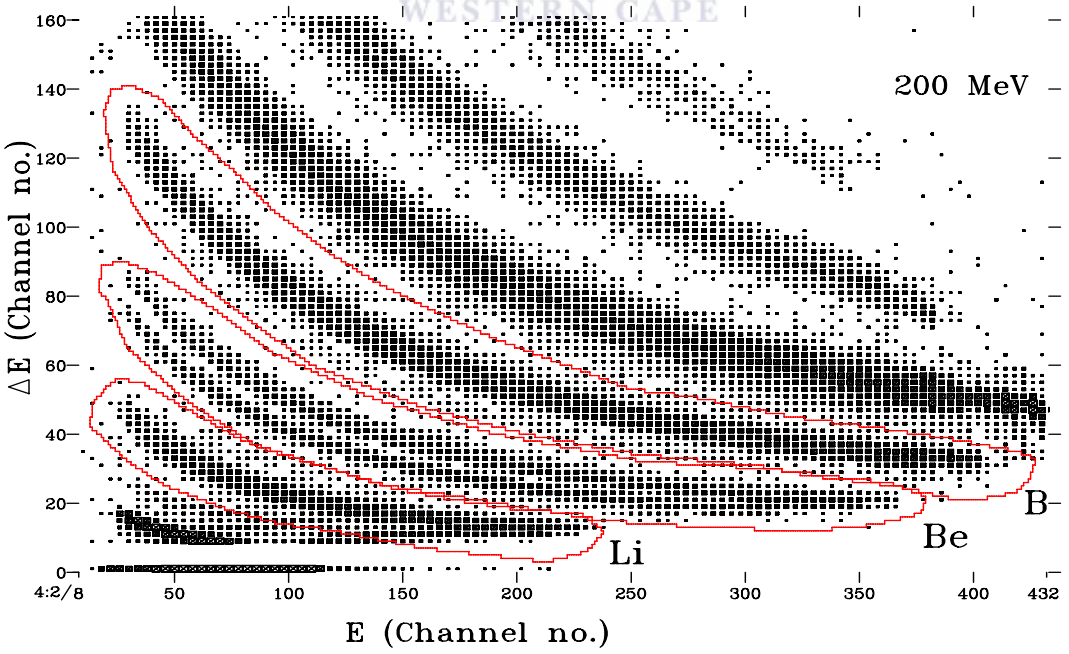

Figure 3.9: Si PID spectrum from the interaction of ^{12}C with ^{12}C at an incident energy of 200 MeV with gates set around the loci of Li, Be and B as shown.

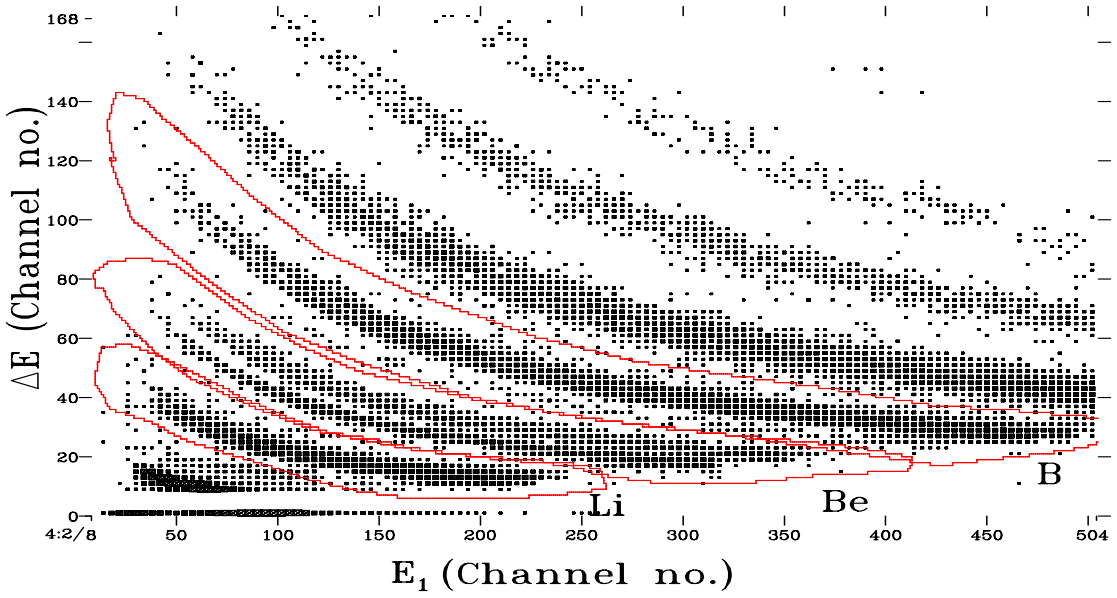

Figure 3.10: Si (ΔE-E_1) PID spectrum from the interaction of ^{12}C with ^{12}C at an incident energy of 400 MeV with gates set around the loci of Li, Be and B as shown.

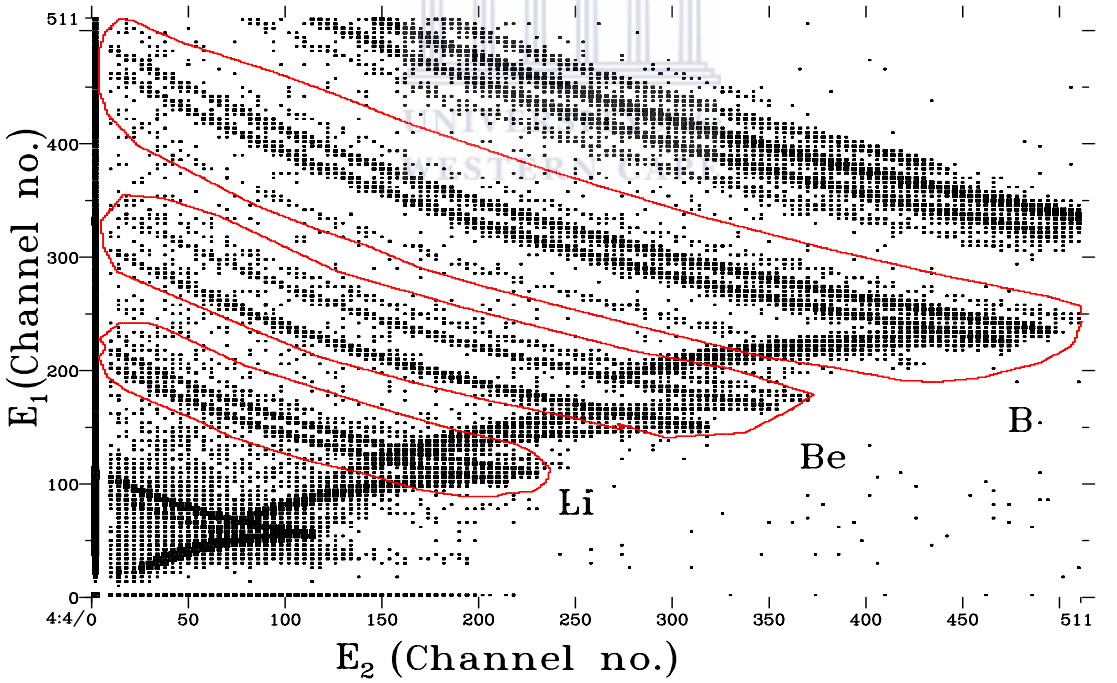

Figure 3.11: Si (E_1-E_2) PID spectrum from the interaction of ^{12}C with ^{12}C at an incident energy of 400 MeV with gates set around the loci of Li, Be and B as shown.

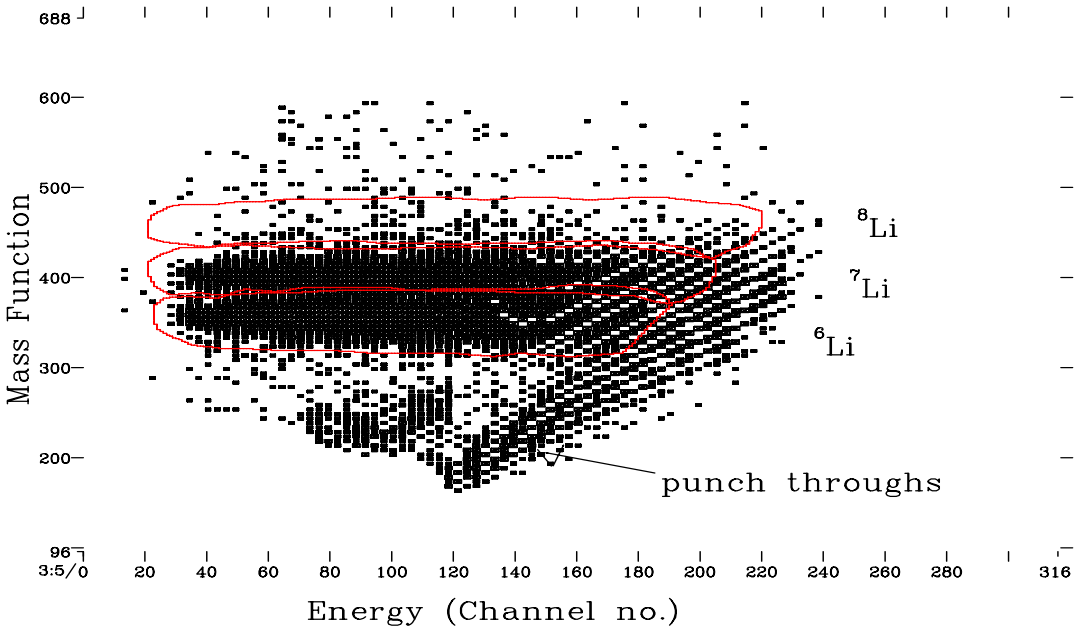

Figure 3.12: Mass function spectrum showing gates that have been set around the ^{6}Li, ^{7}Li and ^{8}Li loci in the interaction of ^{12}C with ^{12}C at an incident energy of 200 MeV.

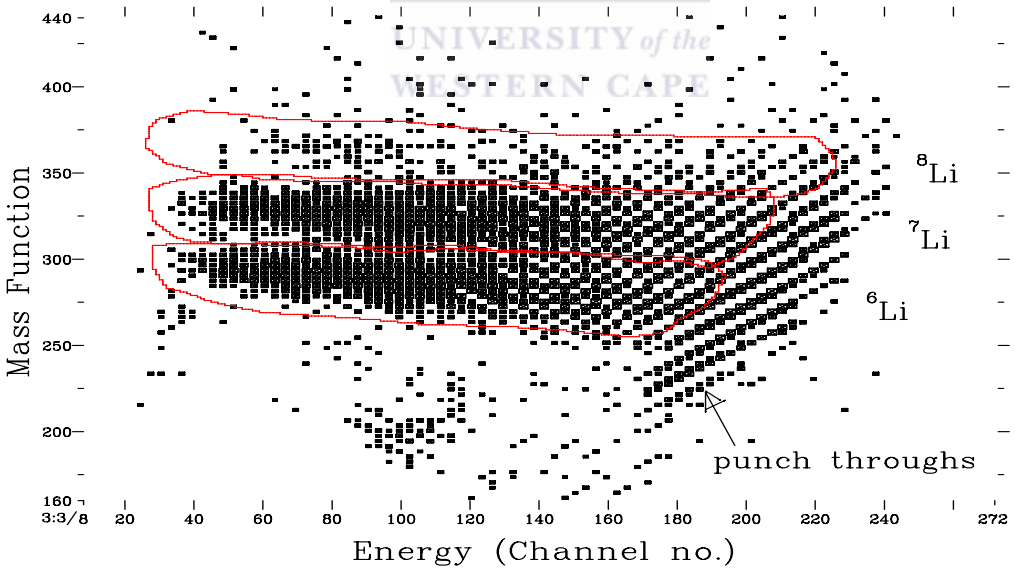

Figure 3.13: Mass function spectrum from the (ΔE-E$_1$) detectors showing gates that have been set around ^{6}Li, ^{7}Li and ^{8}Li loci in the interaction of ^{12}C with ^{12}C at an incident energy of 400 MeV.

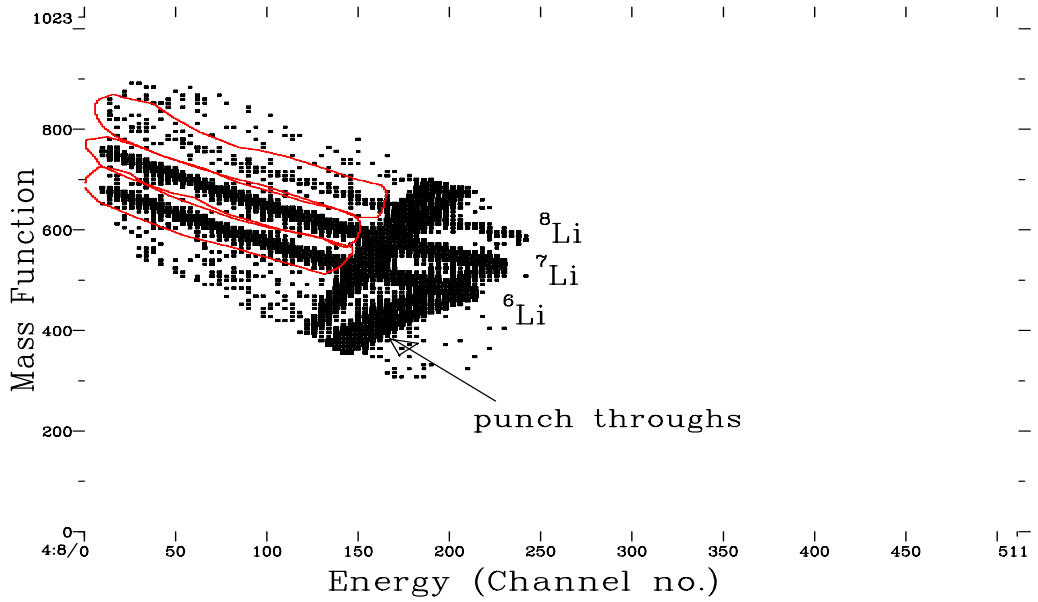

Figure 3.14: Mass function spectrum from the (E_1-E_2) detectors showing gates that have been set around ^{6}Li, ^{7}Li and ^{8}Li loci in the interaction of ^{12}C with ^{12}C at an incident energy of 400 MeV.

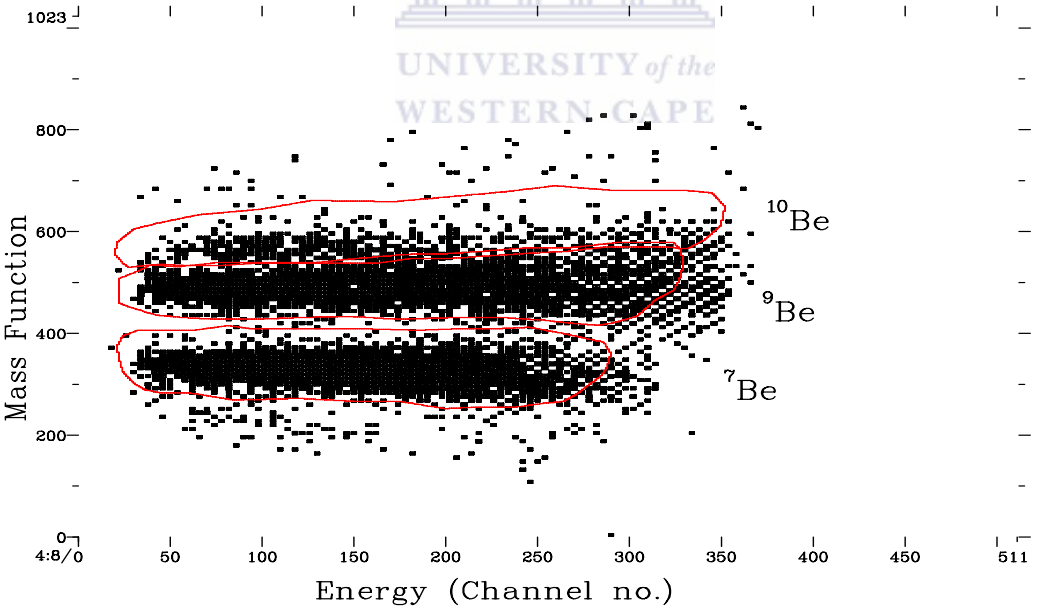

Figure 3.15: Mass function spectrum showing gates that have been set around ^{7}Be, ^{9}Be and ^{10}Be loci in the interaction of ^{12}C with ^{12}C at an incident energy of 200 MeV.

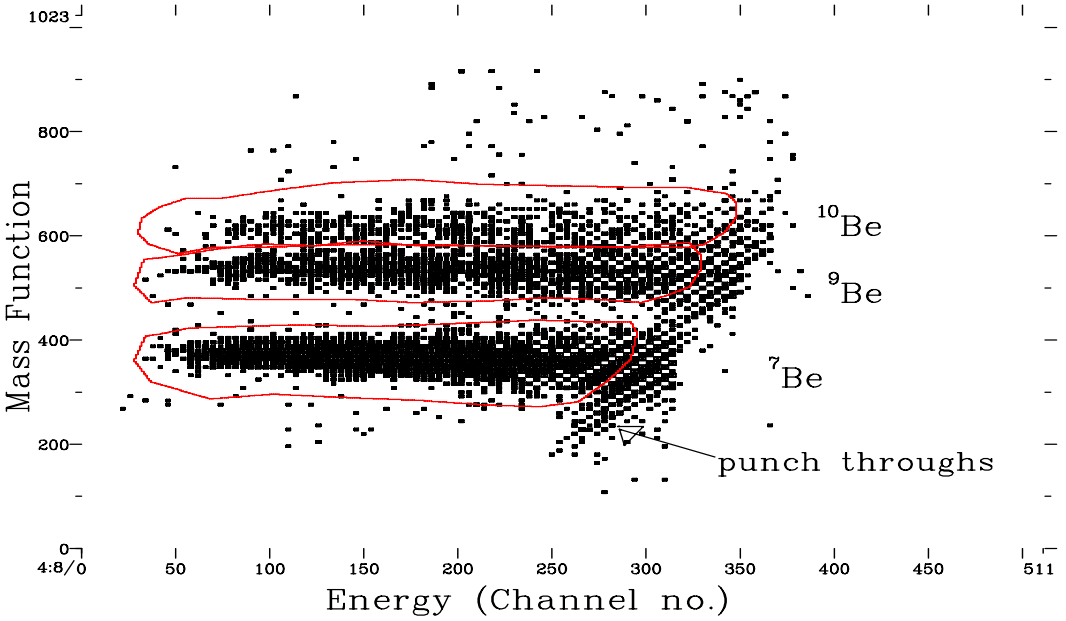

Figure 3.16: Mass function spectrum from the (ΔE-E_1) detectors showing gates that have been set around ^{7}Be, ^{9}Be and ^{10}Be loci in the interaction of ^{12}C with ^{12}C at an incident energy of 400 MeV.

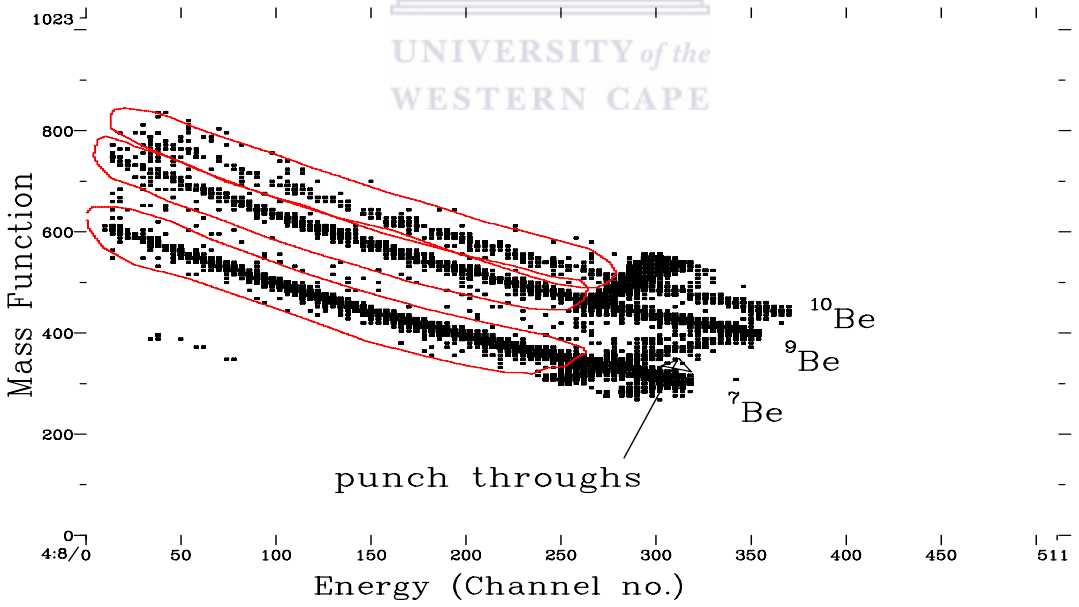

Figure 3.17: Mass function spectrum from the (E_1-E_2) detectors showing gates that have been set around ^{7}Be, ^{9}Be and ^{10}Be loci in the interaction of ^{12}C with ^{12}C at an incident energy of 400 MeV.

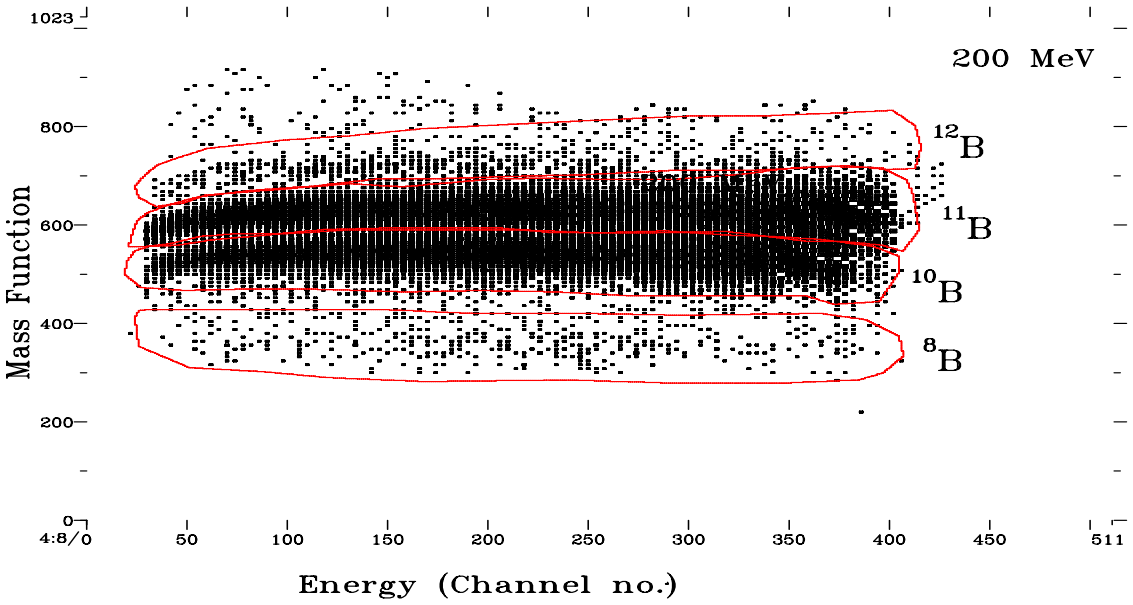

Figure 3.18: Mass function spectrum showing gates that have been set around ^{8}B, ^{10}B, ^{11}B and ^{12}B loci in the interaction of ^{12}C with ^{12}C at an incident energy of 200 MeV.

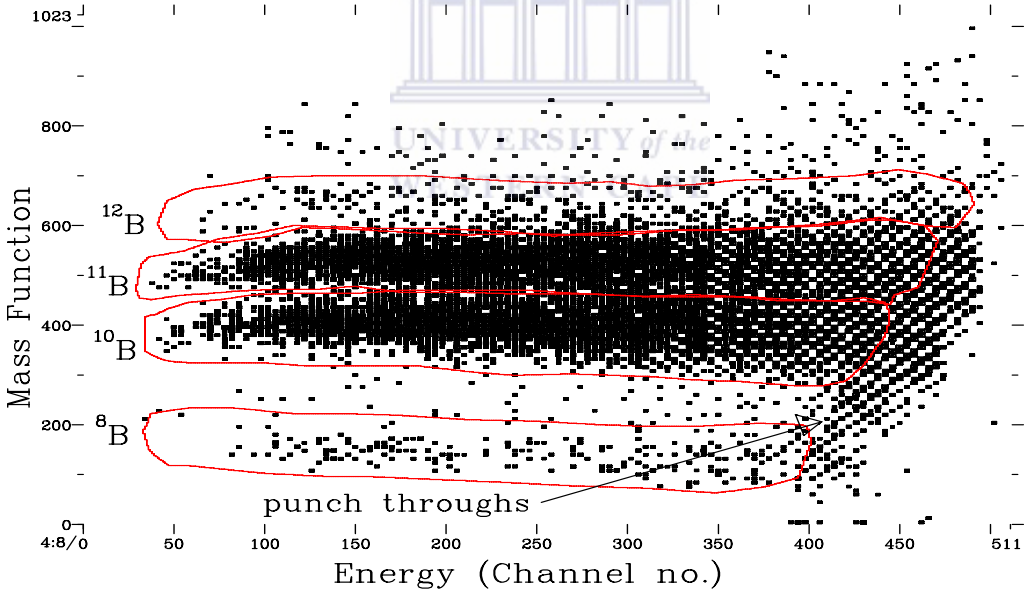

Figure 3.19: Mass function spectrum from the (ΔE-E$_1$) detectors showing gates that have been set around ^{8}B, ^{10}B, ^{11}B and ^{12}B loci in the interaction of ^{12}C with ^{12}C at an incident energy of 400 MeV.

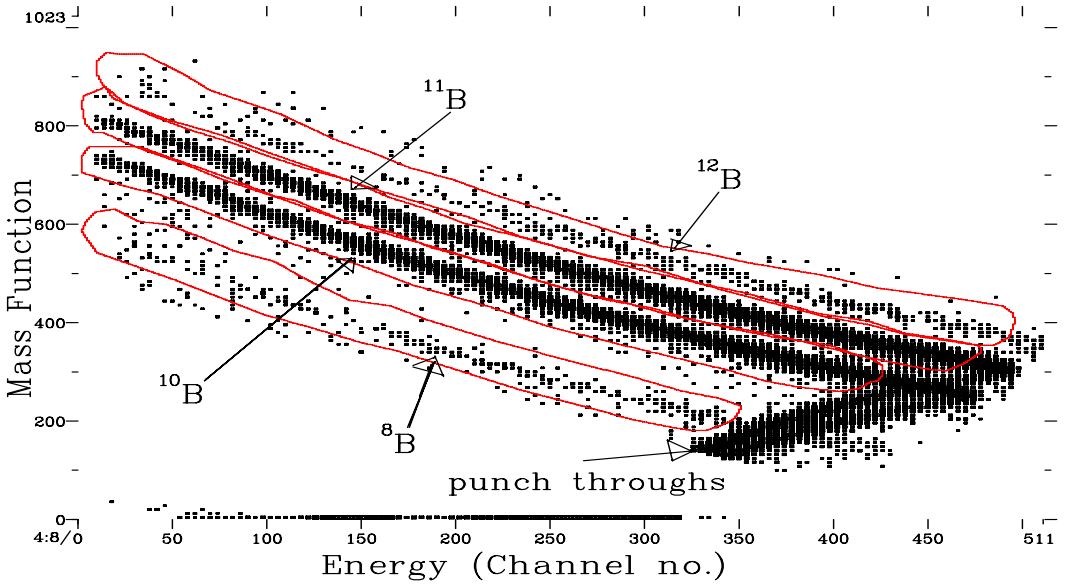

Figure 3.20: Mass function spectrum from the (E_1-E_2) detectors showing gates that have been set around ^{8}B, ^{10}B, ^{11}B and ^{12}B loci in the interaction of ^{12}C with ^{12}C at an incident energy of 400 MeV.

The punch-through events from the mass function spectra were excluded from the gate. This was done to avoid the contamination of the events of interest from other loci. These punch through fold backs were caused by the fragments emitted with high energy that could not stop inside the Si detector telescope and determine the high energy threshold of the Si detectors. The exclusion of the punch through in the gates results in the missing part of the energy spectra at higher energies, which makes it difficult to perform the theoretical calculations.

3.6.2 BCD

The PID of the BCD was based on the measured Bragg curve of the ion that stops inside the active volume of the detector [Ass82]. While the length of each curve corresponds to the range of the ion in the gas, the area beneath the curve is proportional to the energy lost by the particle, and the maximum height of the Bragg peak corresponds to the charge number (Z) of the detected particle. Figure 3.21 shows a typical raw PID spectrum of the BCD. This spectrum was contaminated mainly by high energy protons and alpha particles punching through the detector and therefore it was difficult to fully separate the loci of Li, Be and B. In order to remove the

contaminating events from the PID of the BCD a further two-dimensional spectrum was generated. Valid BCD events were selected by gating on events in the spectrum of energy versus pulse length (m). Figure 3.22 shows the gated energy versus pulse length from which the BCD PID spectrum was generated. Figure 3.23 shows the resulting BCD PID spectrum with gates set around the loci of Li, Be and B. Figure 3.24, 3.25 and 3.26 show the spectra of Li, Be and B, respectively with gates set around the loci of ^{6,7}Li, ^{7,9}Be and ^{8,10,11}B.

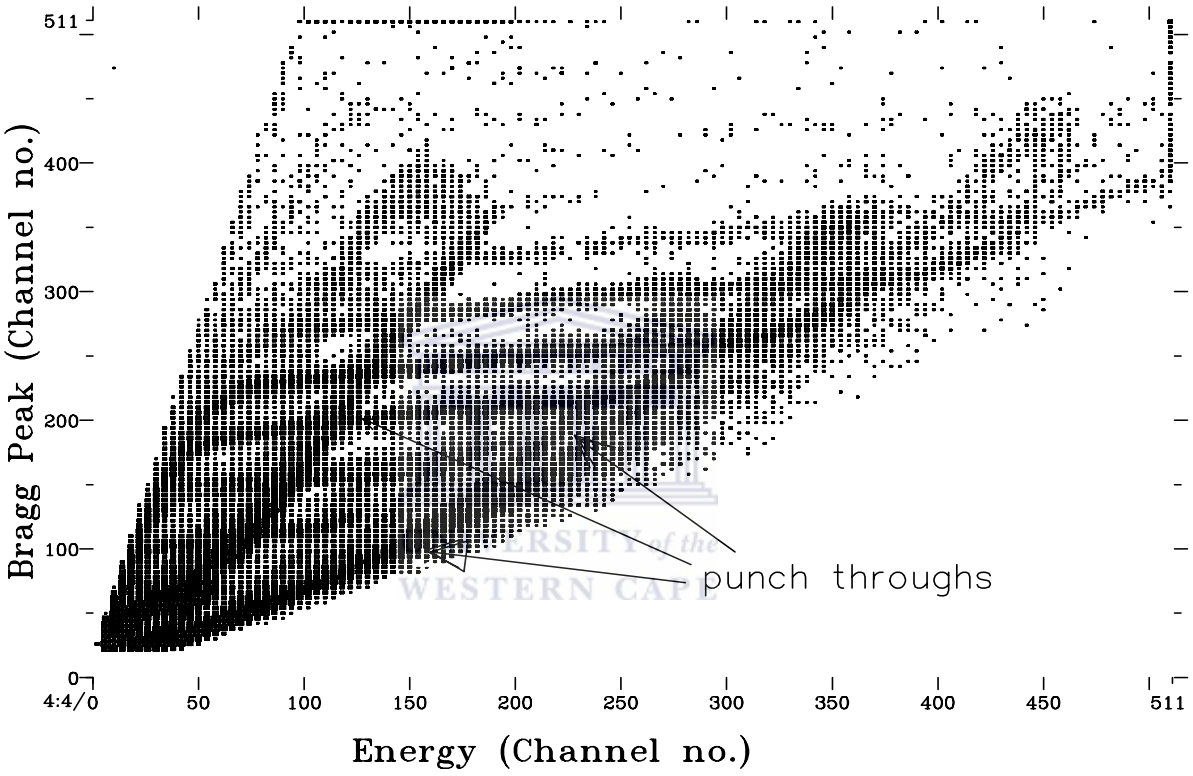

Figure 3.21: Raw BCD PID spectrum with background caused by protons and alpha particles punching through the detector.

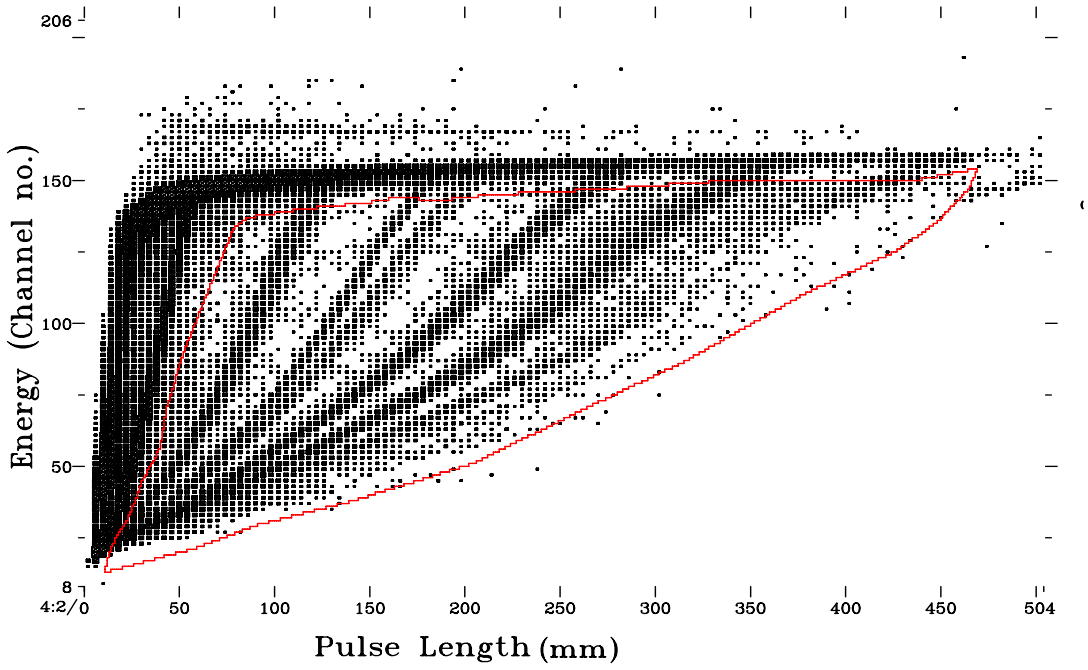

Figure 3.22: Gated energy versus pulse length spectrum used to generate the BCD PID spectrum.

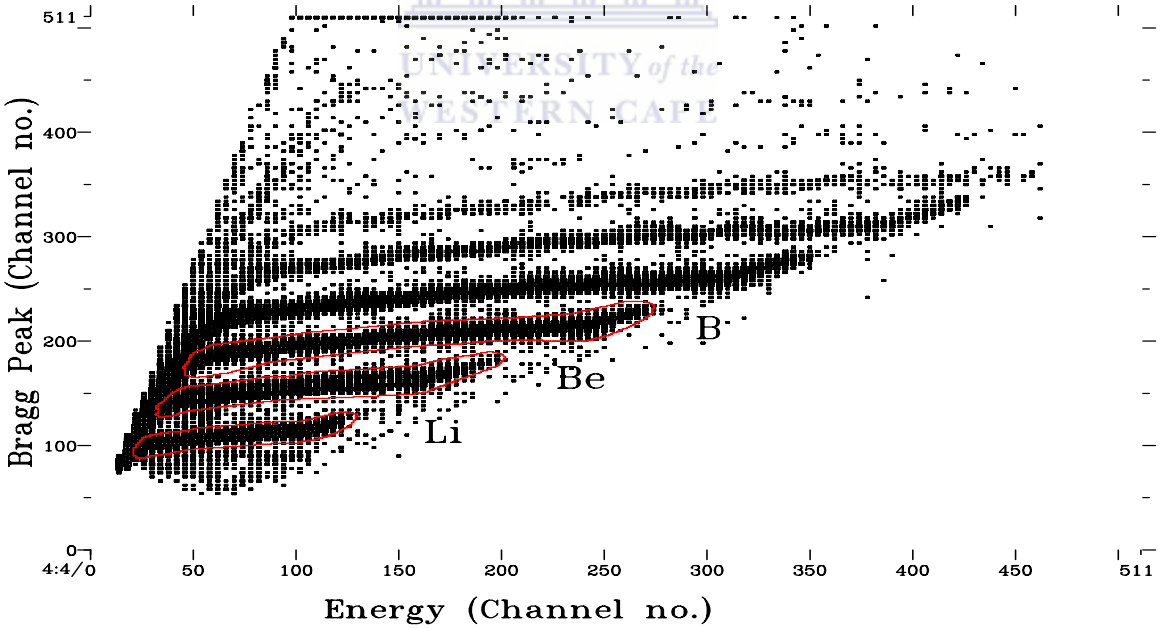

Figure 3.23: Generated BCD PID spectrum with gates set around the fragments of lithium, beryllium and boron in the interaction of ^{12}C with ^{12}C at a beam energy of 200 MeV.

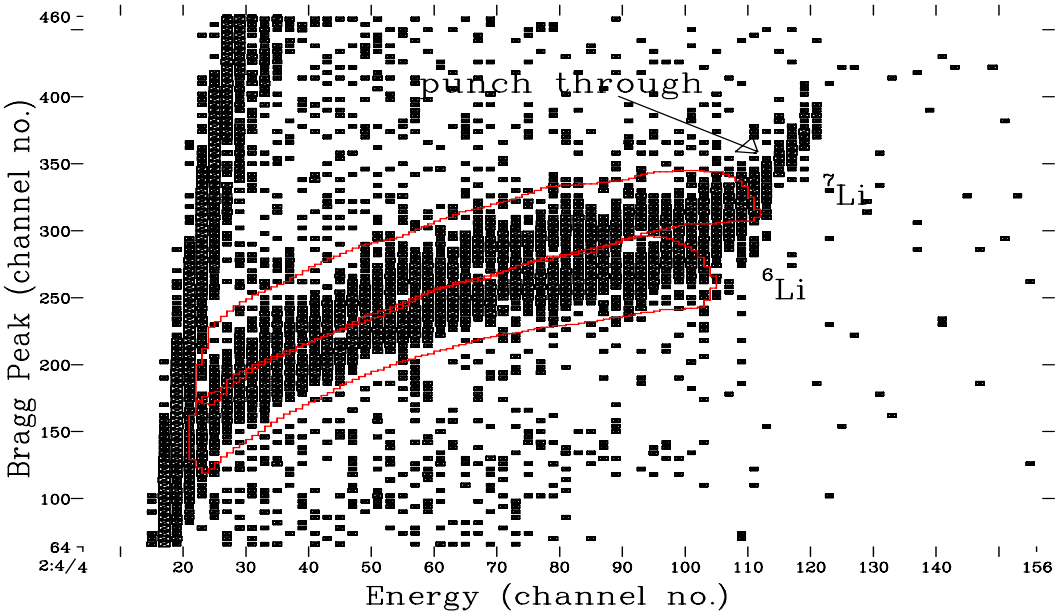

Figure 3.24: BCD PID spectrum with gates set around ^{6}Li and ^{7}Li loci in the interaction of ^{12}C with ^{12}C.

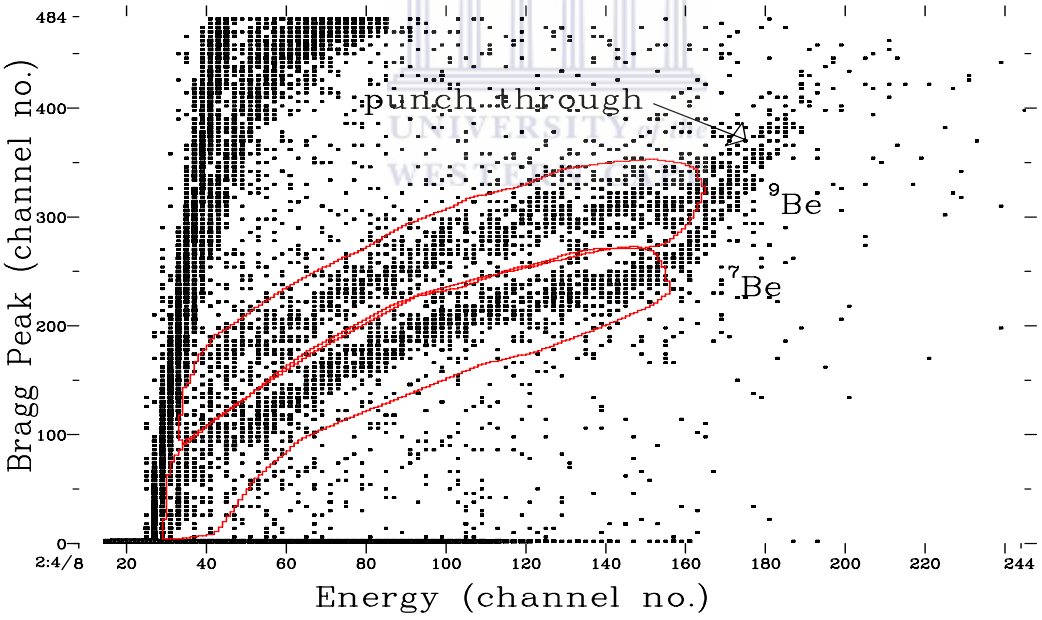

Figure 3.25: BCD PID spectrum with gates set around ^{7}Be and ^{9}Be loci in the interaction of ^{12}C with ^{12}C.

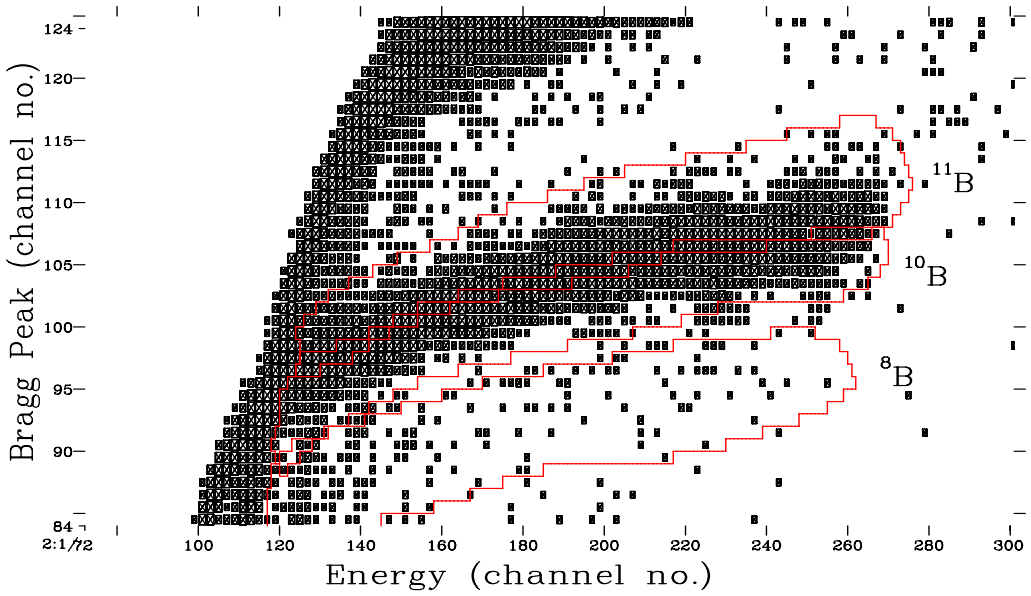

Figure 3.26: BCD PID spectrum with gates set around ^{8}B ^{10}B and ^{11}B loci in the interaction of ^{12}C with ^{12}C.

3.7 Background subtraction

In order to get the correct number of counts in each energy spectrum, the background had to be subtracted from the energy spectra (see table 3.8). The ECR ion source produces ^{12}C ions with charge state of +4 for beam energy of 200 MeV. When the beam interacts with the target the remaining electrons are stripped off, leaving the ion in the charge state of +6, while the charge state with an empty target remain at +4. In order to perform the background subtraction correctly the total charge from an empty target should be normalized to that of ^{12}C target and also for the time differences in data taking. The normalization was performed by multiplying the total charge from the empty target by a factor of 1.5 which is the ratio the charge state of +6 and +4. To check if the background subtraction was needed, the empty runs of the corresponding angles were analyzed and the energy spectra were examined to check if they were affected by background.

Table 3.8: Contains the angles where the background subtractions were performed for 200 MeV.

Beam Energies	Angles of detection
200 MeV	12º, 17º, 25º, 30º,
400MeV	12º

3.8 Conversion to double differential cross section

Figure 3.27 shows the sum of the energy spectra which were extracted from the mass function spectra generated from the Si (ΔE-E_1) detector and Si (E_1-E_2) detector. The dead layer between the Si (E_1) detector and Si (E_2) detector was found no to be significant.

The number of counts in each bin in energy spectra were converted to double differential cross sections. The energy spectra were all compressed to a dispersion of 4 MeV per bin. It is possible to compress the energy spectra because they correspond to the continuum and does not have narrow peaks. The advantage of compressing the energy spectra is to increase the number of counts in each bin, which reduces the uncertainty in the number of counts. To obtain the double differential cross sections the number of counts in each energy spectrum was multiplied by a conversion factor. The double differential cross sections were obtained as follows

$$\frac{d^2\sigma}{\Delta E \, \Delta \Omega} = N_c * \Lambda \qquad (3.2)$$

where,

N_c is the corrected number of counts per bin in energy spectra

The conversion factor Λ was determined from

$$\Lambda = \frac{1}{\Delta E \, \Delta \Omega} \frac{e \cos \theta_T A}{N \lambda_T N_A D} \tag{3.3}$$

where,

ΔE is the energy per bin (MeV)

$\Delta \Omega$ is the solid angle in sr

e is the proton charge

D is the correction factor for the electronic dead time

ρ is the density of the target given by

$$\rho = \frac{\lambda_T N_A}{\cos \theta_T A} \tag{3.4}$$

where,

λ_T is the thickness of the target expressed in mass per unit area

N_A is the Avogadro number

A is the atomic mass of the target nucleus

θ_T is the angle of the target normal to the beam direction

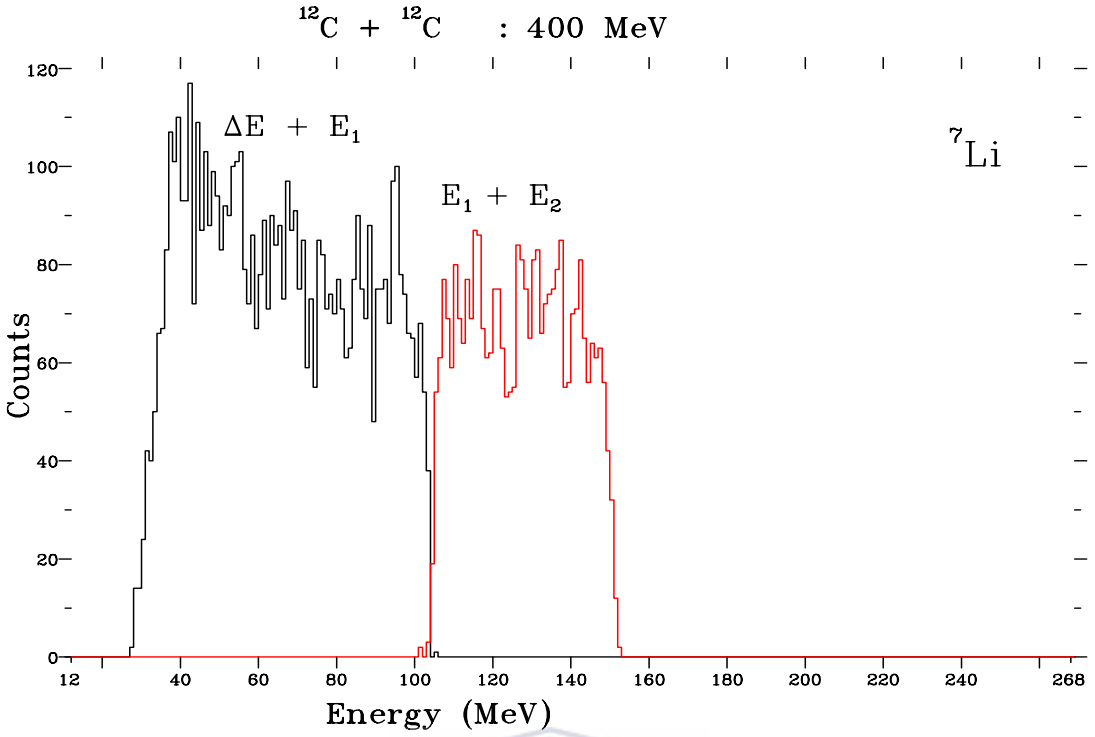

Figure 3.27: Sum of the energy spectra of ^{7}Li from the Si ($\Delta E+E_1+E_2$) detector at an incident energy of 400 MeV. Data are binned in 1 MeV energy bins.

3.9 Error analysis

There are two types of errors that affect the experimental results. These errors are related to the methods used to perform an experiment and also to the counting statistics of the results. The sections below discuss these errors.

3.9.1 Statistical error

The statistical error is due to the uncertainty in the total number of counts. These uncertainties may arise from the systematic error or from the inherent statistical nature of the phenomenon being observed [Leo87]. The statistical error of number of counts N_i is the square root of the total number of counts, $\sqrt{N_i}$. The corrected number of counts is thus given by $N_i \pm \sqrt{N_i}$. The statistical error for the background subtraction was performed by XSYS for each analyzed spectrum. The double differential cross

sections are plotted together with their statistical errors which are presented as error bars.

3.9.2 Systematic error

Systematic errors are uncertainties in the bias of the data [Leo87]. These errors occur due to uncertainties in the measurement of a particular instrument that is used in the experiment. All instruments which are assumed to contribute to the systematic errors are discussed below.

3.9.2.1 Energy calibrations

The errors in the energy calibrations of the Si detectors arose from the uncertainties in the identification of channel numbers corresponding to the alpha peaks from ^{228}Th source and the elastic and inelastic peaks. The energy calibration was confirmed by comparing the high energy peaks of the analyzed spectra of different isotopes to the calculated energy values of the ground state peak using the KINMAT program. Some of the energy spectra were out by about 2 MeV to the expected values calculated with KINMAT. The energy calibration of the Si detector had an estimated uncertainty of about 1%. For the BCD, the energy loss of the alpha particle at the entrance window caused the major uncertainty in the energy calibration while the gas pressure and the thickness of the entrance window also affected the energy calibration. The uncertainty was estimated to be 1.00%.

3.9.2.2 Particle identification

The uncertainties in the particle identification were caused by the fold back of loci of Li, Be and B which crossed over the lower lying loci and thereby resulted in higher number of counts in the energy spectra. To avoid this problem the fold back events were excluded from the gate set around a specific locus. Further uncertainties also arose from the gates that were set around the different loci in the mass function spectra to select the different isotopes. The uncertainties in the PID spectra of the BCD were caused by the gates set around the loci of Li, Be and B isotopes. The overall uncertainty was estimated to be 1% for both the BCD and Si detectors.

3.9.2.3 Solid angle

The uncertainties in the measurement of the distance between the center of the target to the back of the collimators of the Si detector telescope and BCD as well as the measurement of the radii of the collimators mainly contributed to the uncertainties in the solid angles. The uncertainties in the solid angles were estimated to be about 1%.

Table 3.9: Target positions as a function of energy loss of the 8.78 MeV alpha and a ^{12}C target thickness.

Target position	Target	8.78 MeV peak (Channel no.)
445	^{12}C	319.8
450	^{12}C	319.7
440	^{12}C	320.0
455	^{12}C	320.1
435	^{12}C	320.0
	Empty	322.1

3.9.2.4 Target thickness

The uniformity of the target thickness plays an important role in the systematic error. The uncertainty in the target thickness was checked by using a ^{228}Th source. The 8.78 MeV alpha particles from the source were directed to different positions on the thin ^{12}C target to examine the uniformity of the target thickness (table 3.9). The consistency of the 8.78 MeV peak shows that the uncertainty in the thickness of the target was less than 1%.

3.9.2.5 Electronic dead time

The electronic dead time uncertainty was estimated to be less than 2%.

3.9.2.6 Total charge

The uncertainty in the total charge collected by the current integrator of the beam stop was estimated to be less than 0.5% [Dla06].

Total uncertainties

The total uncertainty is calculated by summing up the squares of the uncertainties and taking the square root of the sum (see table 3.10).

Table 3.10: Summary of all uncertainties from different sources for both BCD and silicon detector telescope.

	Si telescope	BCD
Sources	Error in %	Error in %
Total charge	0.5	0.5
Energy calibration	1	1
Particle identification	1	1
Target thickness	1	1
Solid angle	1	1
Electronic dead time	2	2
Total systematic error	2.9	2.9

CHAPTER 4

THEORETICAL MODEL

4.1 Introduction

Most of the experiments performed at iThemba LABS to study the role of nuclear reaction mechanisms involved in the production of IMFs induced by ^{12}C and ^{16}O interacting with medium mass target nuclei such as ^{59}Co, ^{93}Nb and ^{197}Au have been interpreted by means of a theoretical model developed at the University of Milan [Gad99], [Gad03], [Bec03] and [För05]. These earlier studies showed that this model could be successfully implemented to reproduce the energy spectra using different reaction mechanisms such as projectile and target fragmentation and nucleon coalescence through complete and incomplete fusion reactions. In order to perform the calculations using this model a complete set of experimental data is required. The ^{12}C + ^{27}Al and ^{27}Al + ^{12}C experiments were performed in order to understand the reaction mechanisms involved in the production of IMFs produced from the interaction of light ions and most importantly for their application in hadron therapy and radiation protection during space missions and also to separate the fragments produced during the target fragmentation from that produced from the projectile. The reactions mechanisms which were included in the interaction of ^{12}C + ^{27}Al and the inverse reaction to interpret the energy spectra are evaporation, break-up fusion and nucleon transfer. The present ^{12}C + ^{12}C experiment is another extension of this study.

The aim of the present theoretical interpretation is to examine which reaction mechanisms are involved in the production of ^{8}B, ^{10}B, ^{11}B and ^{12}B at different

emission energies and angles in the interaction of ^{12}C with ^{12}C at incident energies of 200 MeV and 400 MeV. The reaction mechanisms added to the applied model include complete fusion reaction, break-up fusion reactions, binary break-up and evaporation.

This chapter revisits the projectile and target fragmentation as well as the nucleon coalescence in which statistical equilibrium is reached through cascade of nucleon-nucleon (N-N) interaction. The theory of projectile and target fragmentation is given by a Serber approximation [Ser47] and the nucleon coalescence is interpreted by using a set of Boltzmann Master Equations (BME) for proton [Cav01], are described in details in the following sections. The evaporation was evaluated by simulating the complete fusion with the BME event generator and the break-up fusion with the FLUKA-LPWBA event generator.

The theoretical calculations are performed by using nuclear transport and Monte Carlo simulation code FLUKA. FLUKA code is also used in the treatment planning in hadron therapy starting from nucleus-nucleus reaction modeling at low energy to CT-based dose calculations and biological effective dose calculations.

4.2 Binary break-up mechanism

The break-up of the projectile or the target nucleus into two fragments is treated under the binary break-up mechanism. The theory of binary break-up is based on the assumption that projectile or target fragmentation is a peripheral direct reaction occurring in a window of large angular momenta [Lil01], [Gad03]. It is assumed that the probability of the projectile surviving a break-up decreases exponentially with increasing projectile energy loss [Mai07], [Gad03]. Following this assumption the spectra of the break-up fragments are evaluated by folding the local plain wave approximation (LPWA) cross-section with an exponential survival probability [Gad00], [Gad02]. It is also assumed that the break-up may occur after a minimal energy loss $E_{l,min}$, the double differential cross-section of a fragment emitted at the angle θ with energy E' from a projectile breakup with incident energy E_o is given by [Gad02],

$$\frac{d^2\sigma}{dEd\Omega}(E_o, E', \theta) = \sigma_{bu} \frac{\int_{E_{l,\min}}^{E_o} P(E_l) S(E, E', \theta) dE_l}{\int_{E_{l,\min}}^{E_o} P(E_l) dE_l} \quad (4.1)$$

where,

E_o is an incident energy of the projectile,

E' is the energy of the produced fragment,

σ_{bu} is the angle and energy integrated break-up cross-section of the produced fragment,

E_l is the energy lost by the projectile before break-up,

$P(E_l)$ is the survival probability after the energy loss E_l and is given by equation 4.2,

$$P(E_l) = \exp[-C(E_l - E_{l,\min})] \quad (4.2)$$

The cross-section ***S*** for producing the fragment of energy E' at angle θ in the breakup of a projectile of energy $E = E_o - E_l$, is given by equation 4.3,

$$S(E, E', \theta) = d^2\sigma^s(E, E', \theta) / dE' d\Omega \quad (4.3)$$

In the LPWA [Ser47, McV80] the cross-section is evaluated with

$$\frac{d^2\sigma^s(E, E', \theta)}{dE' d\Omega} = P' P'' \left|\Psi(\overrightarrow{P})\right|^2 \quad (4.4)$$

where,

P' is the linear momentum of the spectator fragment,

P'' is the linear momentum of the participant fragment,

Ψ is the Fourier transform of the wave function describing the relative motion of the fragment within the projectile, given by equation 4.5

$$\psi(\vec{P}) = \frac{1}{(2\pi\hbar)^{3/2}} \int \psi(r) \exp[-\frac{i}{\hbar}(\vec{p} \bullet \vec{r})] d\vec{r} \qquad (4.5)$$

$\psi(r)$ is the choice of wave function which describes the fragment's relative motion inside the projectile, p is the internal momentum distribution of the fragment inside the projectile and is given by

$$p = \vec{P}' - (m_f / m_p)\vec{P} \qquad (4.6)$$

where,

$\vec{P}$ is the projectile's momentum when it breaks up,

$\vec{P}'$ is the momentum of the observed fragment just after break-up,

m_f is the mass of the observed fragment

m_p is the mass of the projectile.

The break-up calculations performed for the B-spectra in the present work include the breakup of the projectile or target nucleus into ^{11}B and a proton, and their breakup into ^{10}B and a deuteron.

4.3 Nucleon coalescence

Nucleon coalescence occurs when the projectile or participant fragment fuses with the target nucleus, the energy of the projectile or participant fragment is shared equally among the nucleons of the compound nucleus due to interaction between the nucleons, and after the statistical equilibrium is reached nucleons of the same momentum escape from the compound nucleus as clusters of IMFs. The time evolution of a highly excited compound nucleus (e.g. ^{24}Mg* from the complete fusion in the interaction of ^{12}C with ^{12}C) towards the statistical equilibrium is evaluated by solving a set of Boltzmann Master Equations (BME) [Cav96]. The important aspect one needs to know in order to evaluate the spectra of emitted particles is the momentum distribution of the nucleons within the excited nucleus [Gad03]. This is

given by the occupation probabilities of bins into which the momentum space is divided. If the mean values are considered, to evaluate the inclusive particle spectra, one may assume azimuthal symmetry with respect to the beam direction and use as variables p^2 and p_z, which are the square of the nucleon's momentum and its component along the beam axis, respectively. From this assumption the bins may thus be characterized by constant values of Δp^2 (or $\Delta \in$) and Δp_z. The bin indices label momentum space intervals with volume $V_p = \Delta \in \Delta p_z$ centered around given values of energy $\in_i$, and $(p_z)_i$. The bin occupation probabilities $n_i(\in, \theta, t)$ are function of time, nucleon energy and the angle between the nucleon momentum and the projectile direction. Describing the nucleon state as two-fermion's gas, the occupation probabilities at a subsequent time are evaluated by integrating the set of Boltzmann Master Equations (BME) [Cav98]

$$\begin{aligned}\frac{d(n_i g_i)^{\pi}}{dt} = \sum_{jlm} [\,& \omega^{\pi\pi}_{lm\to ij} g_l^{\pi} n_l^{\pi} g_m^{\pi} n_m^{\pi} (1-n_i^{\pi})(1-n_j^{\pi}) \\ & - \omega^{\pi\pi}_{ij\to lm} g_i^{\pi} n_i^{\pi} g_j^{\pi} n_j^{\pi} (1-n_l^{\pi})(1-n_m^{\pi})] \\ & + \sum_{jlm} [\,\omega^{\pi\nu}_{lm\to ij} g_l^{\pi} n_l^{\pi} g_m^{\nu} n_m^{\nu} (1-n_i^{\pi})(1-n_j^{\pi}) \\ & - \omega^{\pi\nu}_{ij\to lm} g_i^{\pi} n_i^{\pi} g_j^{\nu} n_j^{\nu} (1-n_l^{\pi})(1-n_m^{\nu})] \\ & - n_i^{\pi} g_i^{\pi} \omega^{\pi}_{i\to i'} g_{i'}^{\pi} \delta(\in_i^{\pi} - \in_F^{\pi} - B_i^{\pi} - \in_{i'}^{\pi}) - \frac{dD_i^{\pi}}{dt}\end{aligned}$$

(4.7)

where,

π and ν indicate protons and neutrons , respectively,

the quantities g_i are total number of states in bin i,

the quantities $\omega_{ij\to lm}, \omega_{i\to i'}$ and dD_i / dt are, respectively, the internal transition decay rates, the decay rates for emission of a single proton into the continuum, and a

depletion term which accounts for the emission of protons bound in a cluster. The internal transition rates $\omega_{ij\to lm}$ are given by [Cav98],

$$\omega_{ij\to lm} = \frac{1}{2\pi}\int_0^{2\pi} \omega_{\mathrm{i\,j\to l\,m}} d\phi_j, \tag{4.8}$$

where,

$$\omega_{\mathrm{i\ j\ \to l\ m}} = \frac{\sigma_{\mathrm{ij}} v_{\mathrm{ij}} \prod_{\mathrm{i\ j\ \to l\ m}}}{V}. \tag{4.9}$$

Here V is the nuclear volume, v_{ij} is the two interacting nucleon relative velocity. The indeces **i, j, l, m** stand for momenta $\mathbf{p}_i$, $\mathbf{p}_j$, $\mathbf{p}_l$, $\mathbf{p}_m$ and ϕ_j is the azimuthal angle of $\mathbf{p}_j$, having taken $\phi_i = 0$. The quantity $\prod_{ij\to lm}$ represents the probability of reaching bins l and m if the interacting nucleons have the momenta $\mathbf{p}_i$ and $\mathbf{p}_j$ belonging to bins i and j, respectively

$$\omega_{\,i\to\,i'} = \frac{\sigma_{\,inv} v'_{\,i}}{g_{\,i} V'}, \tag{4.10}$$

where,

σ_{inv} is the inverse process cross section and v'_i is the relative velocity between the nucleon and the residual nucleus. When neglecting the nucleus recoil momentum it coincides with the nucleon velocity with respect to the center of mass system. The V' is the laboratory volume which cancels a similar factor appearing in the expression of $g_{i'}$. The differential multiplicity of the particles emitted in the time interval dt at an angle θ with energy E' is given by

$$\frac{d^3N'(E',\theta,t)}{dE'd\theta dt} = RN(\in,\theta,t)\frac{\sigma_{inv}\nu'}{V'}\rho(E',\theta), \tag{4.11}$$

and the measured multiplicities are given by

$$\frac{d^2M}{dE'd\Omega} = \int_0^{t^*}\frac{1}{2\pi\sin\theta}\frac{d^3N'(E',\theta,t)}{dE'd\theta dt}dt, \tag{4.12}$$

where,

E' is the energy of the emitted particle in the continuum,

$N(\in,\theta,t)$ is the occupation probability of the states of the considered particle inside the composite nucleus,

R is the survival factor that takes into account the possible dissolution of the cluster into its constituent nucleons before emission,

t^* is the time at which the emission of high energy particles is over.

$$\rho(E',\theta) = \frac{\sin\theta}{2}\rho(E'), \tag{4.13}$$

where $\rho(E')$ is the density of the particle states in the continuum. For clusters with energy E_c inside the nucleus, the direction of which forms an angle θ_c with respect to the beam, $N(\in,\theta,t) \equiv N(E_c,\theta_c,t)$ is given by,

$$N(E_c,\theta_c,t) = \prod_i (n_i^{\pi})^{P_i(E_c,\theta_c)Z_c} \cdot \prod_i (n_i^{\nu})^{P_i(E_c,\theta_c)N_c}, \tag{4.14}$$

The index i runs over all the bins which the nucleons constituting the cluster may be found. $P_i(E_c, \theta_c)$ is the fraction of the bin i within the Fermi sphere of the cluster c with radius p_{cF}. Z_c and N_c are the numbers of protons and neutrons of cluster c, respectively. If Q_c is the Q-value for the cluster emission and $A_c = N_c + Z_c$, then E_c', the continuum energy of the cluster c, is given by

$$E_c^{'} = E_c + Q_c - A_c(\in_F - \in_{Fc}), \tag{4.15}$$

where, $\in_F$ and $\in_{Fc}$ are the composite nucleus and the cluster Fermi energies, respectively. The depletion term dD_i^{π} / dt in equation 4.7 is given by

$$\frac{dD_i^{\pi}}{dt} = \sum_c \iint P_i(E_c, \theta_c) Z_c \frac{d^3 N^{'}(E_c^{'}, \theta_c, t)}{dE_c^{'} d\theta_c dt} dE_c d\theta_c, \tag{4.16}$$

where the summation runs over all possible clusters *c* and the integrals are over all the angles and energies of clusters containing a proton or a neutron in bin *i*.

4.4 Complete and incomplete fusion

The process which may occur during the thermalization of a composite nucleus created in the complete fusion or incomplete fusion of two ions is simulated by means of a Monte Carlo event generator which is able to incorporate as input results of the numerical integration of the BME [Cav01] calculations (see section 4.3). To provide the FLUKA code with more realistic treatment of nucleus-nucleus interactions below 100 MeV/nucleon, the evaluation of pre-equilibrium emissions for a representative set of ion pairs at different energies was performed with the BME theory. To extract a possible value for the emission angle of a given particle, its predicted cumulative angular distribution $\int_0^{\theta} \frac{dM}{d\theta} d\theta$ (in the centre of mass (CM) frame) is used at considered incident energy. This is obtained by an interpolation from the pre-equilibrium ejectile calculated at a few energies between 10 and 100 MeV/n. To obtain the energy of the ejectile we sample, using the standard rejection methods in equation 4.17, which accurately reproduce its theoretical double differential spectra (in the CM frame) [Mai07],

$$\frac{d^2M}{dEd\Omega} = E^{P_o(\theta)} \exp(-P_1(\theta) - P_2(\theta)E) \tag{4.17}$$

where E is the ejectile energy, and $P_o(\theta)$, $P_1(\theta)$ and $P_2(\theta)$ are parameters depending on the emission angle, particle type, incident energy, and interacting ions. We get these parameters by interpolating from the values obtained for a few incident energies and emission angles [Mai07].

The calculated spectra are compared with the measured double differential cross sections in chapter 5.

CHAPTER 5

RESULTS AND DISCUSSION

5.1 Overview

This chapter presents the double differential cross sections of the ^{6,7,8}Li, ^{7,9,10}Be and ^{8,10,11,12}B fragments emitted in the interaction of ^{12}C with ^{12}C at incident energies of 200 MeV and 400 MeV. Results of comparisons between the experimental spectra and the theoretical calculations performed with the Milan code are presented for the fragments of ^{8}B, ^{10}B, ^{11}B and ^{12}B emitted in the interaction of ^{12}C with ^{12}C at an incident energy of 200 MeV.

5.2 Inclusive energy spectra of Li, Be and B isotopes

The double differential cross-sections of the inclusive spectra of the ^{6,7,8}Li, ^{7,9,10}Be and ^{8,10,11,12}B isotopes, shown in figures 5.1 to 5.10, were measured over an angular range between 8^{o} and 60^{o} with the Silicon detector telescope and between 15^{o} to 60^{o} with the BCD. These cross sections are shown with statistical errors and are accurate to within a systematic error of approximately 3% (see table 3.5). The energy gap between the data extracted with the BCD and the Si detector telescope is due to the high and low energy thresholds of the BCD and the Si detector telescope, respectively. The Li and Be spectra exclude the events from fold back which result from the particle of interest punching through the stopping detector as described in section 3.6.1.

The double differential cross sections of Li, Be and B isotopes show a rather flat behavior at forward emission angles between 8° and 17° as a function of emission energy due to the contribution of all reaction mechanisms involved in their production

such as nucleon transfer, fragmentation, pre-equilibrium emission, nucleon coalescence through complete and incomplete fusion and evaporation. At emission angle between 20° and 35° the cross sections decrease slightly with increasing emission energy, due to the fact that the contributions of mechanisms such as direct reactions (e.g. nucleon transfer) start to fade. At large emission angles between 40º and 60º the cross sections drop very rapidly with an increasing emission energies and eventually show an exponential decay curve.

Figure 5.11 shows the difference between the cross sections of ^{7}Li, ^{7}Be and ^{10}B emitted at forward angle of 8ºand the ones emitted at an angle of 60. The cross sections show that the production rate of these isotopes of interest is not equal. While ^{6}Li and ^{7}Li seem to be produced at almost the same rate, ^{8}Li was produced at a much lower rate. In the case of Be isotopes the production rate of ^{10}Be is less than the rate of ^{7}Be and ^{9}Be. Although ^{9}Be is produced with the rate slightly lower than ^{7}Be. For the B isotopes ^{8}B and ^{12}B as well as ^{10}B and ^{11}B are produced similar rate, respectively, ^{10}B and ^{11}B are produced at a higher rate than ^{8}B and ^{12}B.

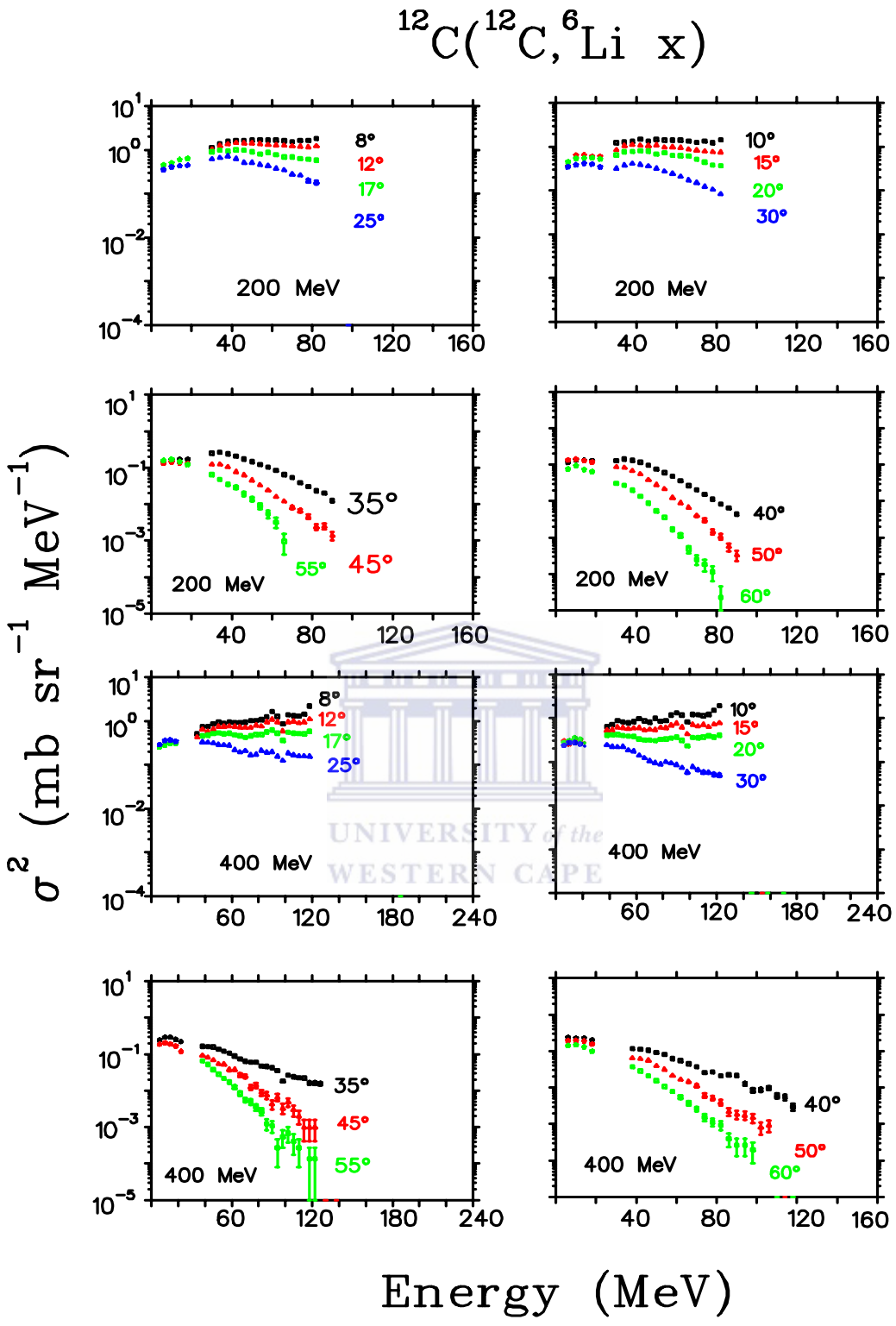

Figure 5.1: Double differential cross sections of ^{6}Li emitted in the interaction of ^{12}C with ^{12}C at incident energies of 200 and 400 MeV at different emission angles as indicated. The BCD data are given by the stars. The error bars reflect the statistical errors.

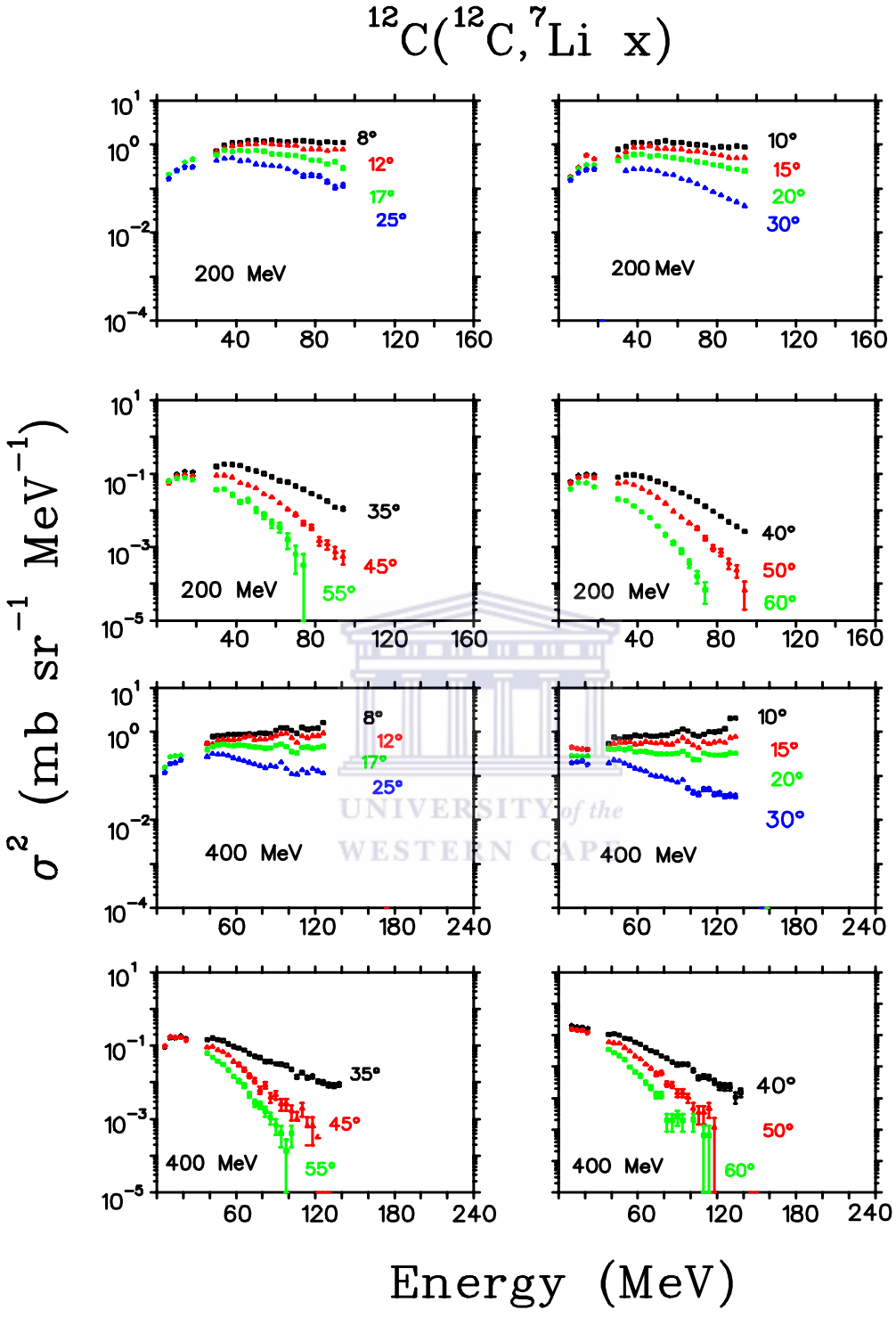

Figure 5.2: Double differential cross sections of ^{7}Li emitted in the interaction of ^{12}C with ^{12}C at incident energies of 200 and 400 MeV at different emission angles as indicated. The BCD data are given by the stars. The error bars reflect the statistical errors.

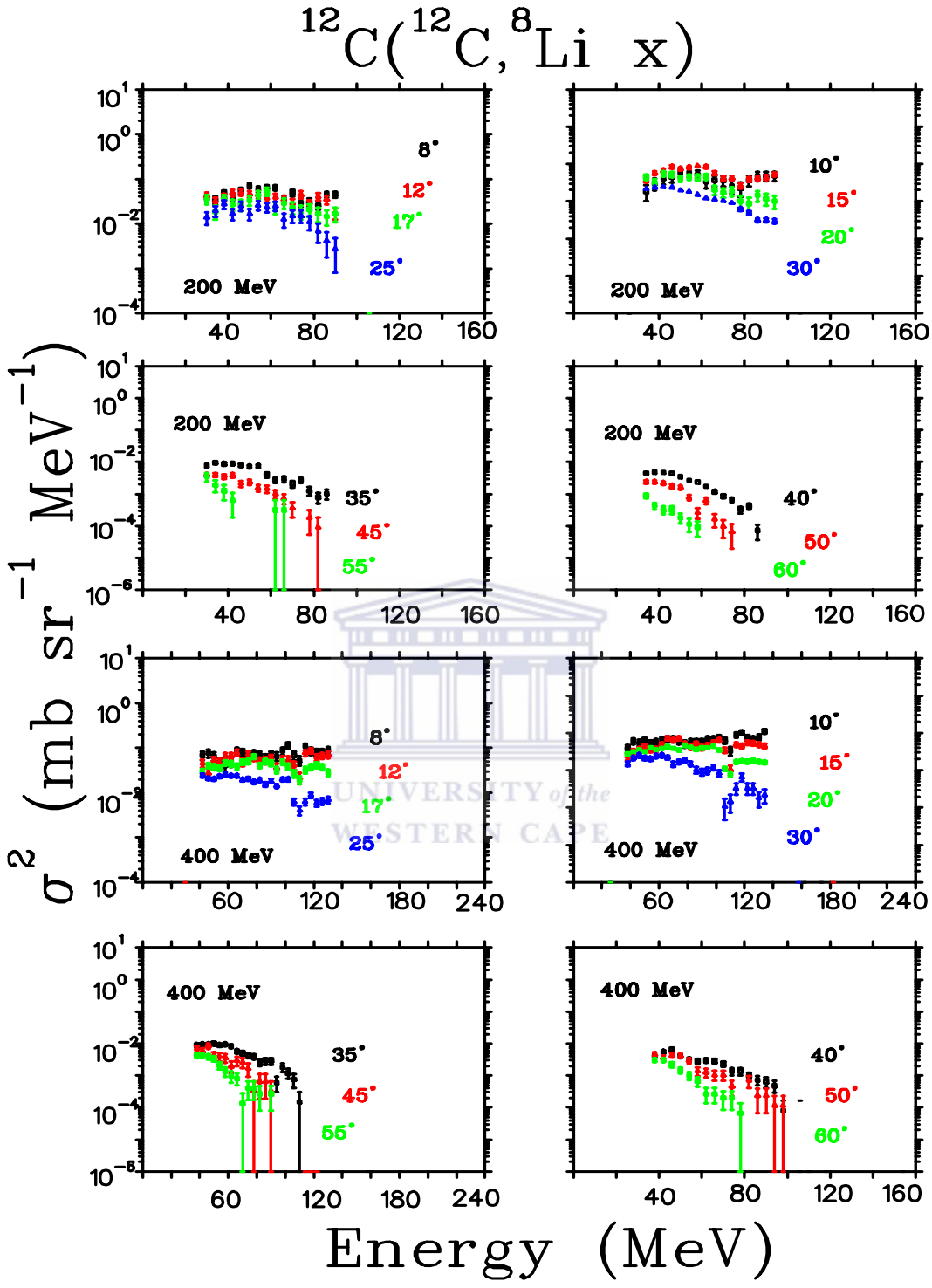

Figure 5.3: Double differential cross sections of ^{8}Li emitted in the interaction of ^{12}C with ^{12}C at incident energies of 200 and 400 MeV at different emission angles as indicated. The BCD data are given by the stars. The error bars reflect the statistical errors.

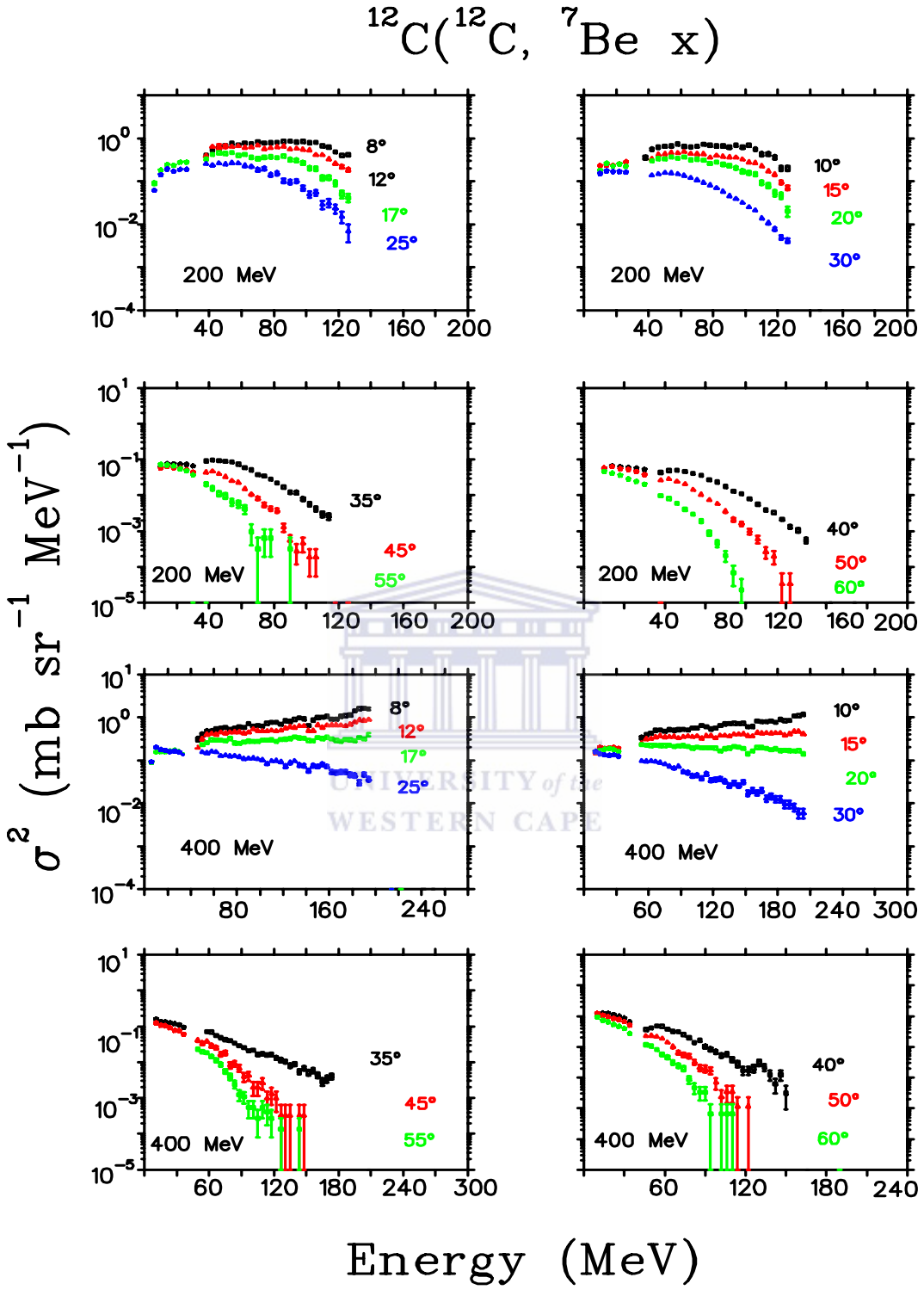

Figure 5.4: Double differential cross sections of ^{7}Be emitted in the interaction of ^{12}C with ^{12}C at incident energies of 200 and 400 MeV at different emission angles as indicated. The BCD data are given by the stars. The error bars reflect the statistical errors.

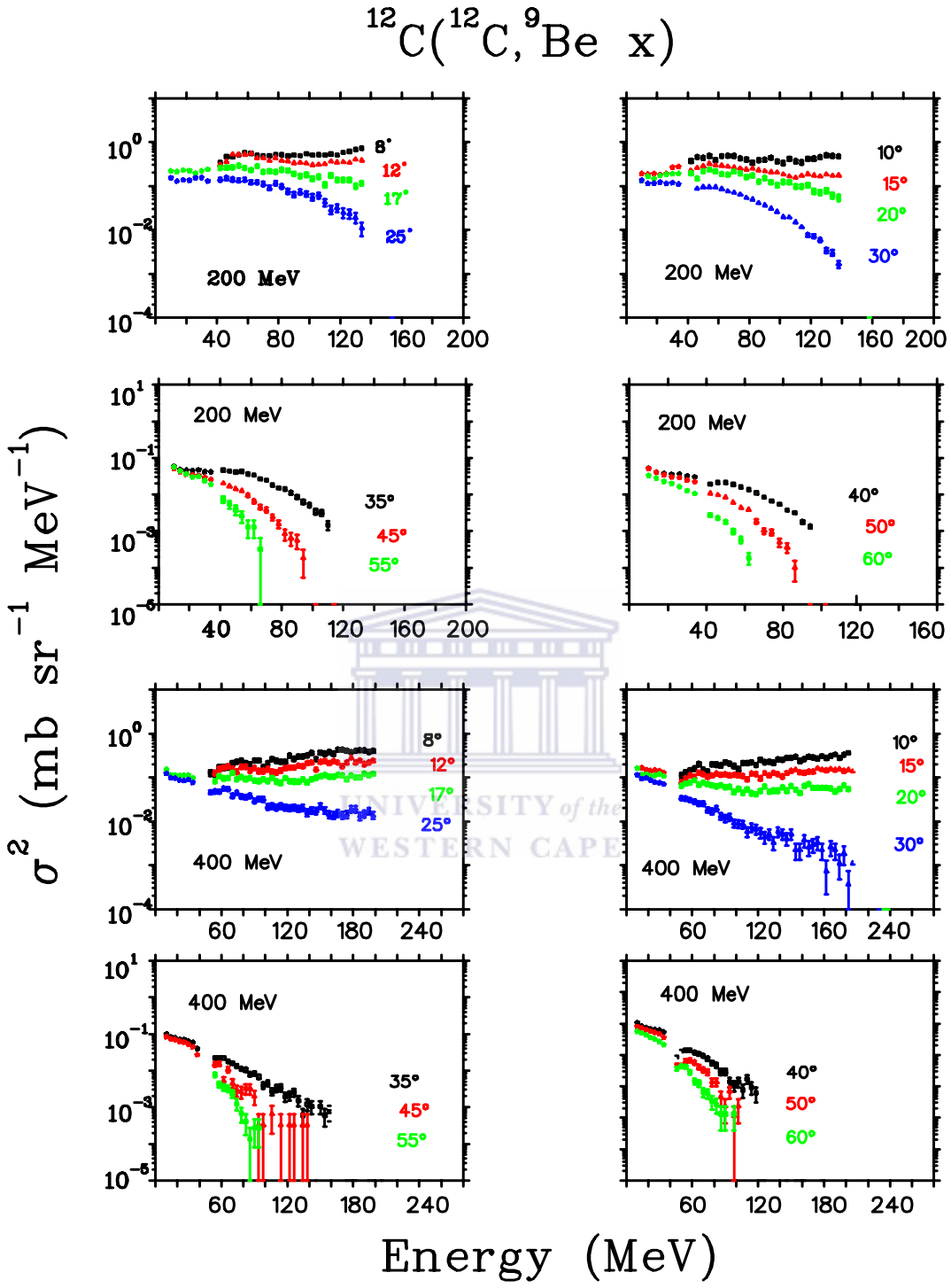

Figure 5.5: Double differential cross sections of ^{9}Be emitted in the interaction of ^{12}C with ^{12}C at incident energies of 200 and 400 MeV at different emission angles as indicated. The BCD data are given by the stars. The error bars reflect the statistical errors.

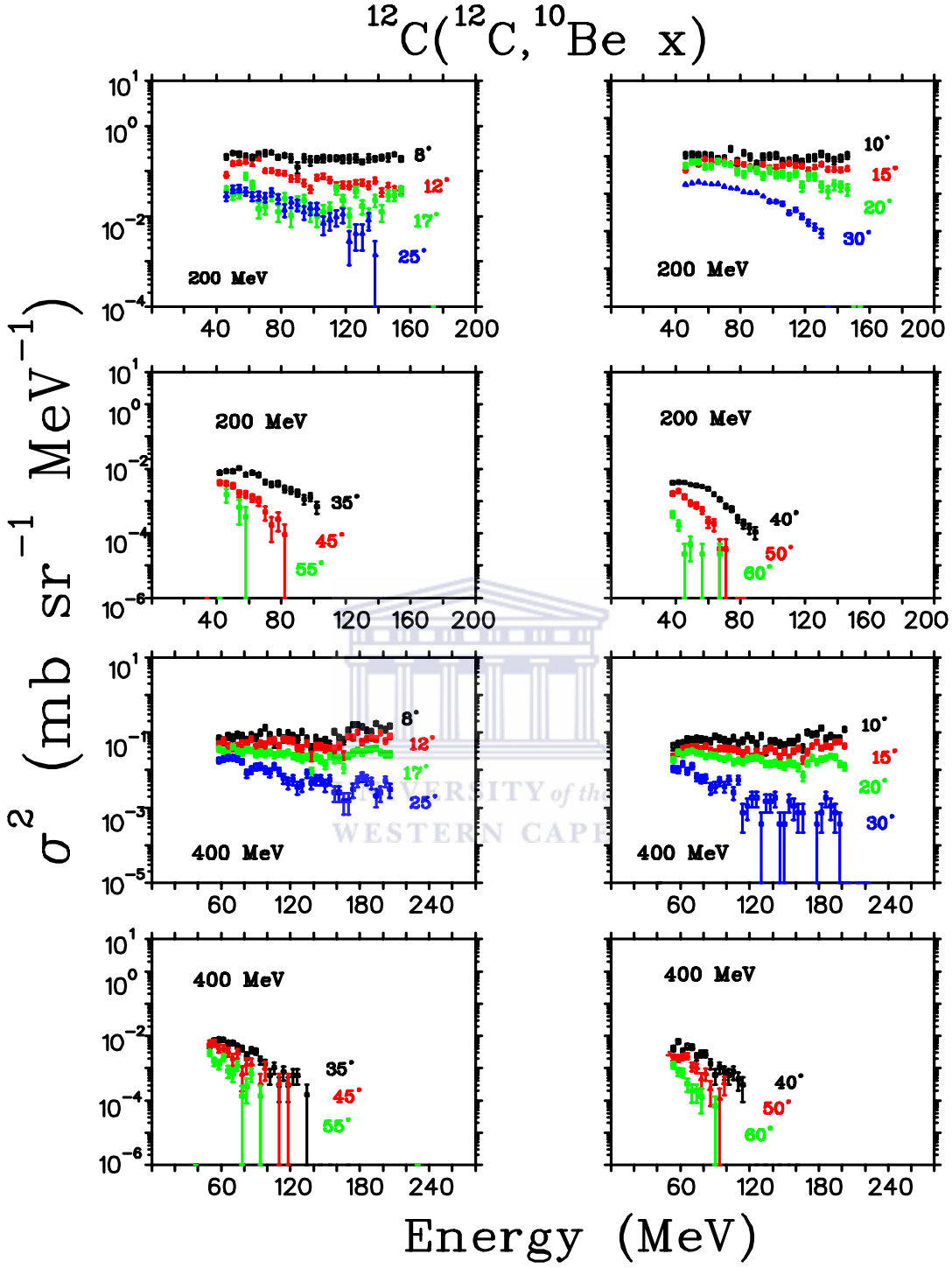

Figure 5.6: Double differential cross sections of ^{10}Be emitted in the interaction of ^{12}C with ^{12}C at incident energies of 200 and 400 MeV at different emission angles as indicated. The BCD data are given by the stars. The error bars reflect the statistical errors.

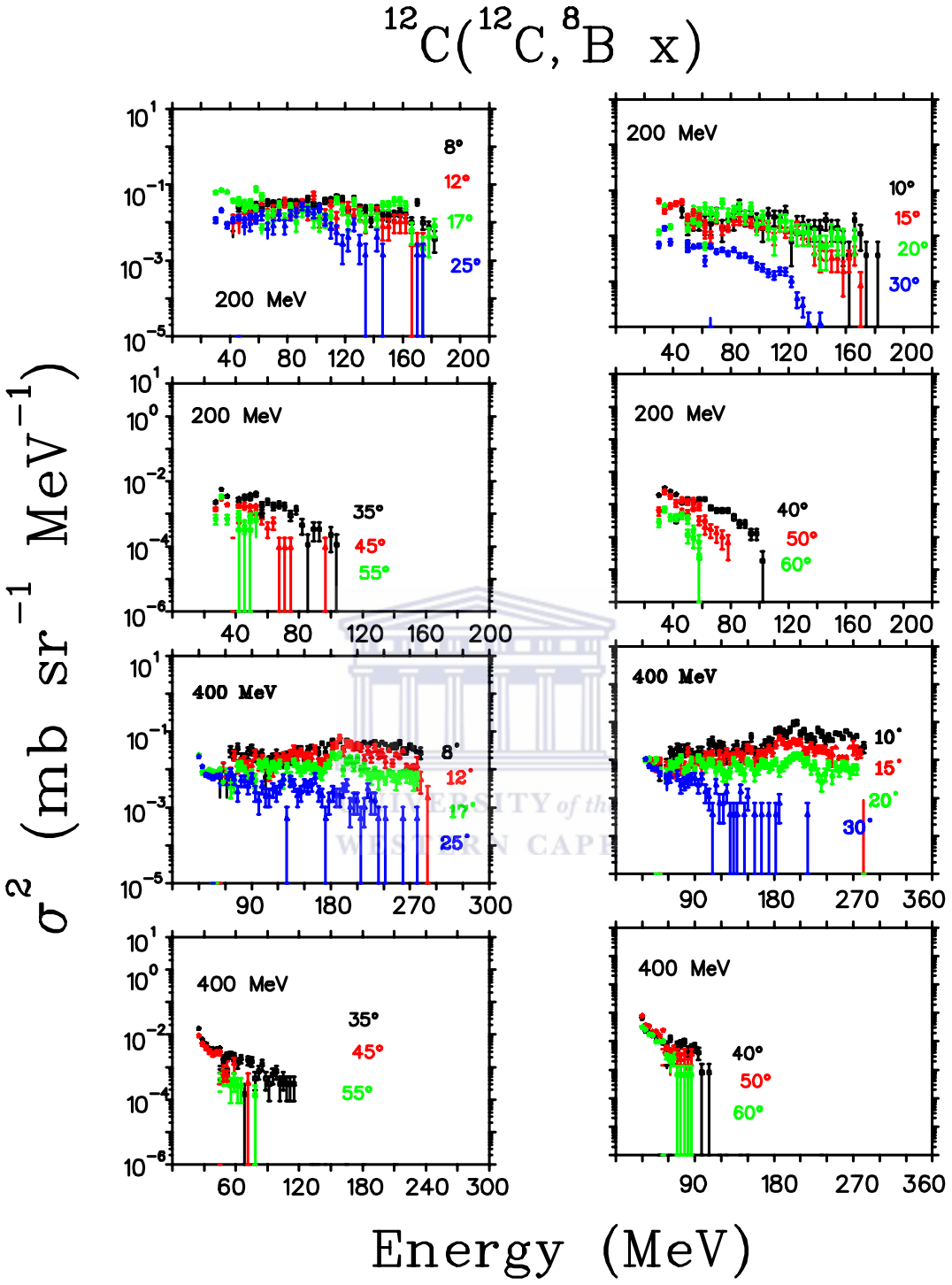

Figure 5.7: Double differential cross sections of ^{8}B emitted in the interaction of ^{12}C with ^{12}C at incident energies of 200 and 400 MeV at different emission angles as indicated. The BCD data are given by the stars. The error bars reflect the statistical errors.

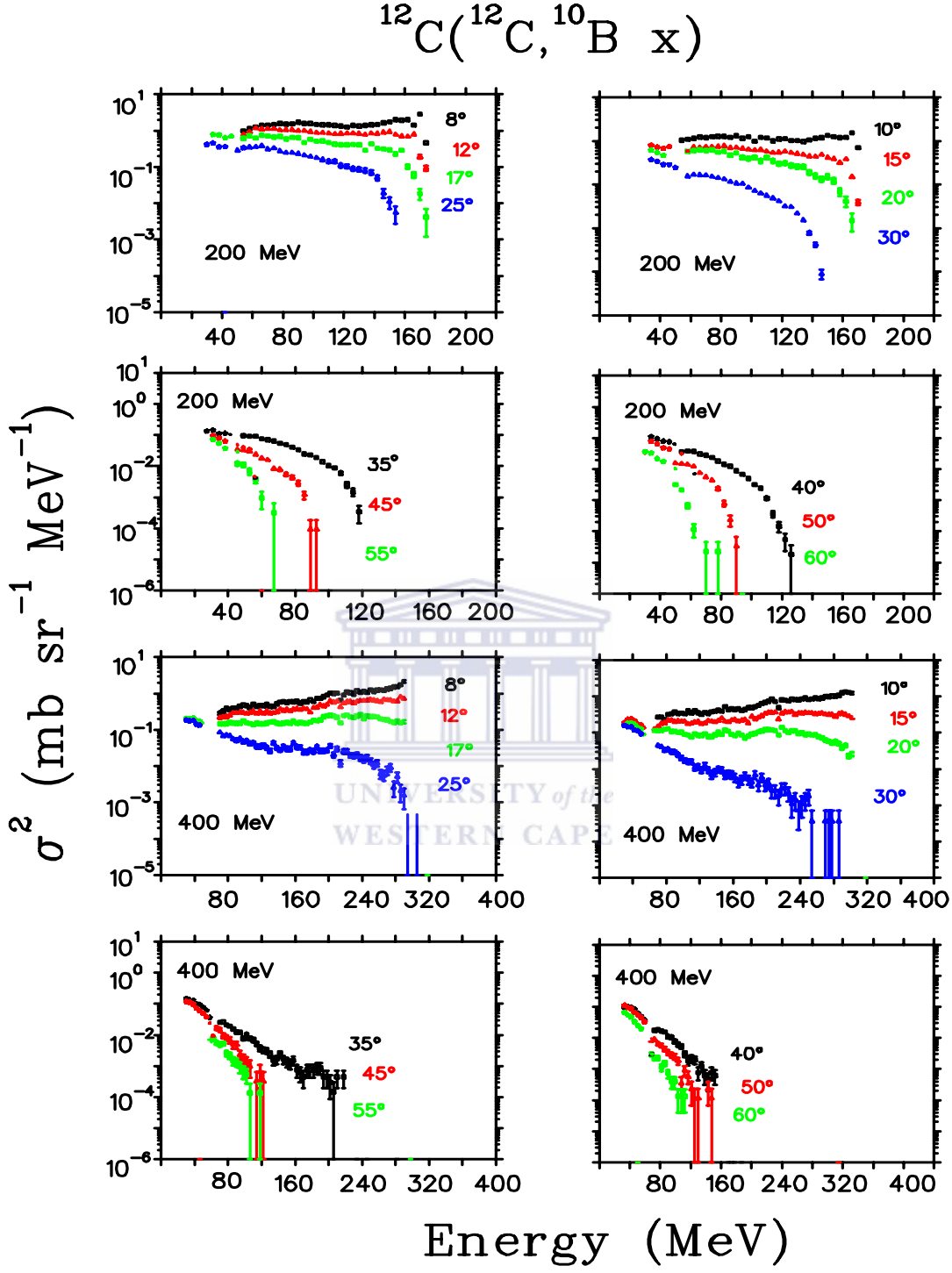

Figure 5.8: Double differential cross sections of ^{10}B emitted in the interaction of ^{12}C with ^{12}C at incident energies of 200 and 400 MeV at different emission angles as indicated. The BCD data are given by the stars. The error bars reflect the statistical errors.

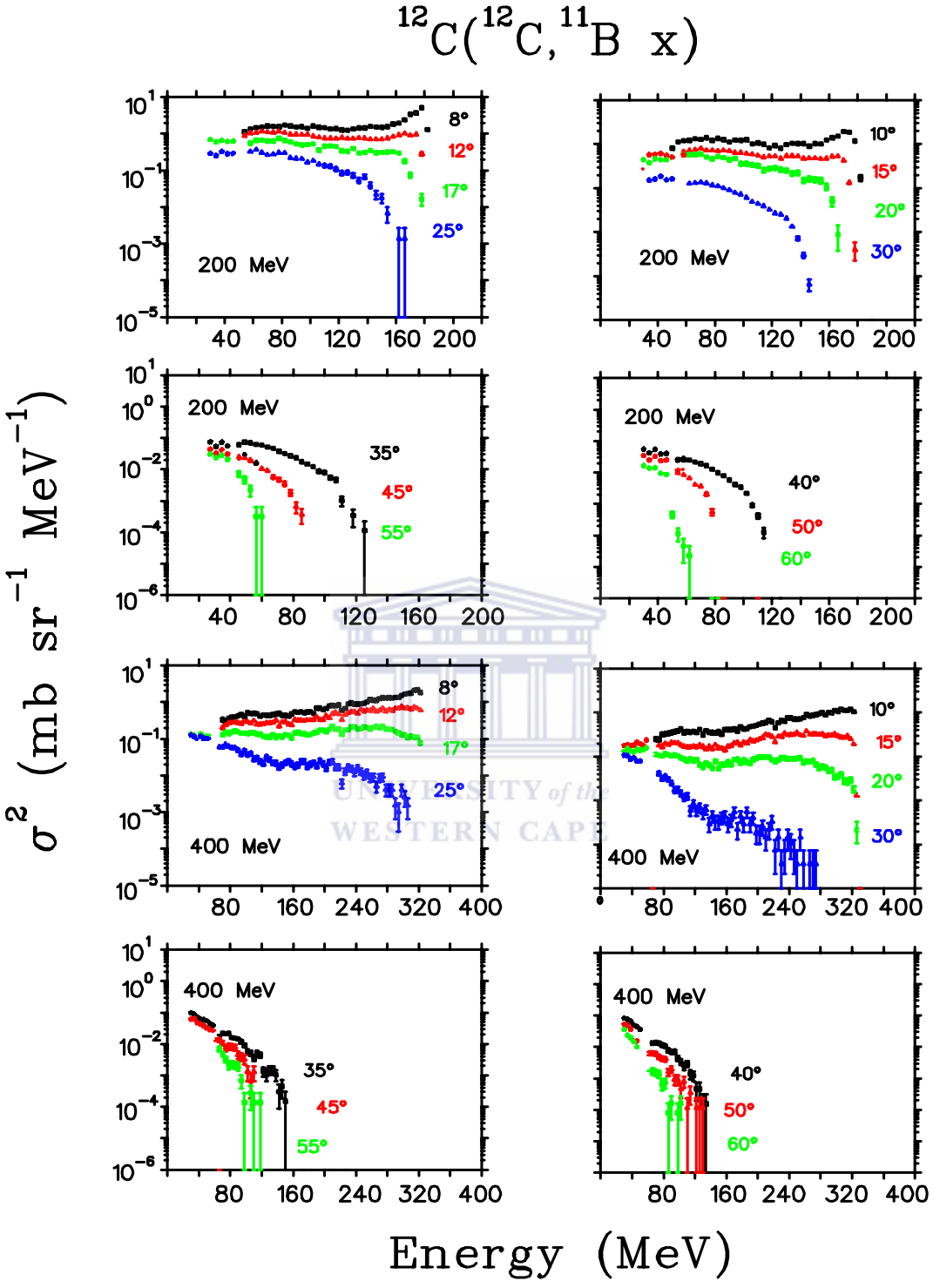

Figure 5.9: Double differential cross sections of ^{11}B emitted in the interaction of ^{12}C with ^{12}C at incident energies of 200 and 400 MeV at different emission angles as indicated. The BCD data are given by the stars. The error bars reflect the statistical errors.

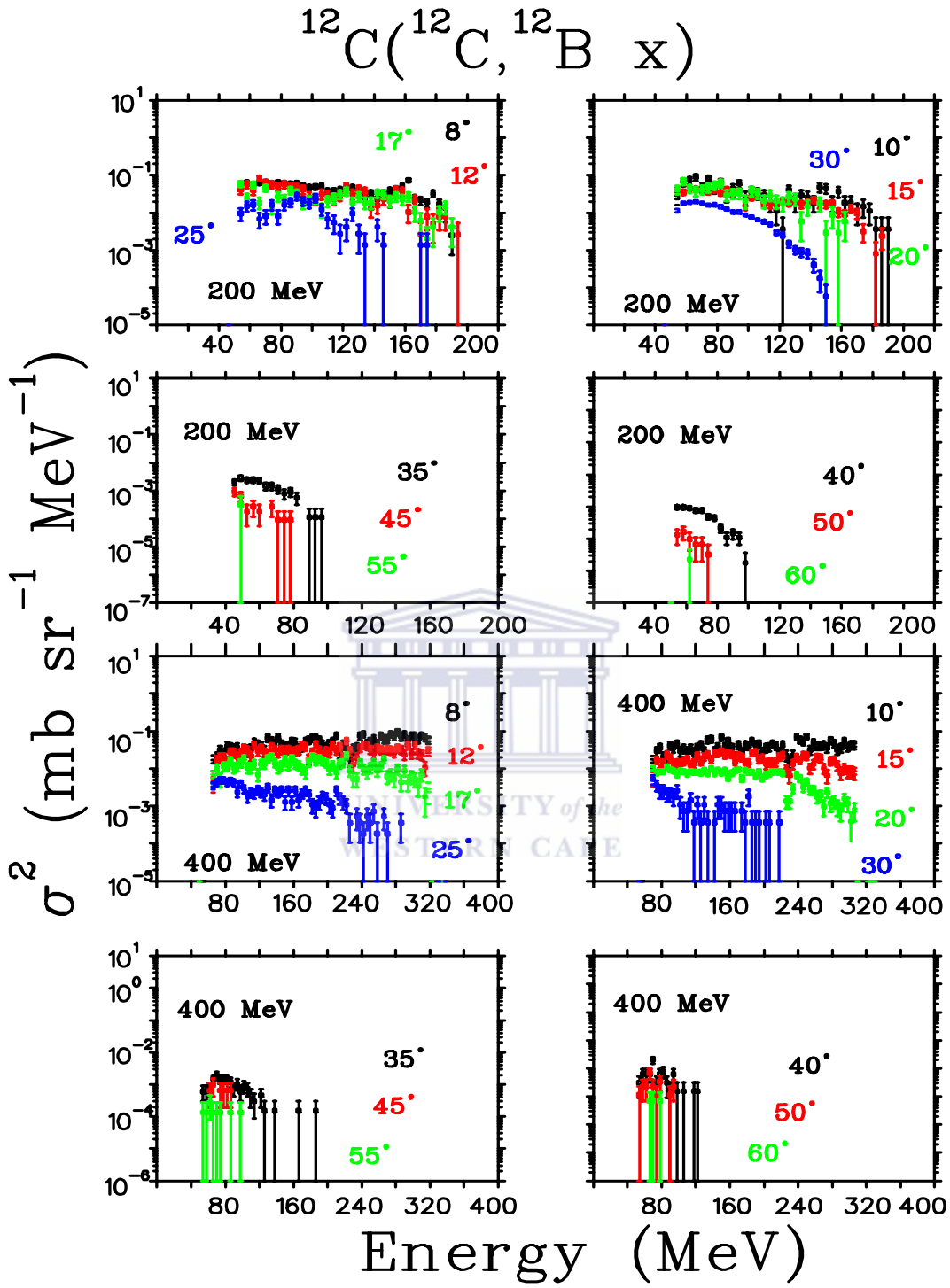

Figure 5.10: Double differential cross sections of ^{12}B emitted in the interaction of ^{12}C with ^{12}C at incident energies of 200 and 400 MeV at different emission angles as indicated. The BCD data are given by the stars. The error bars reflect the statistical errors.

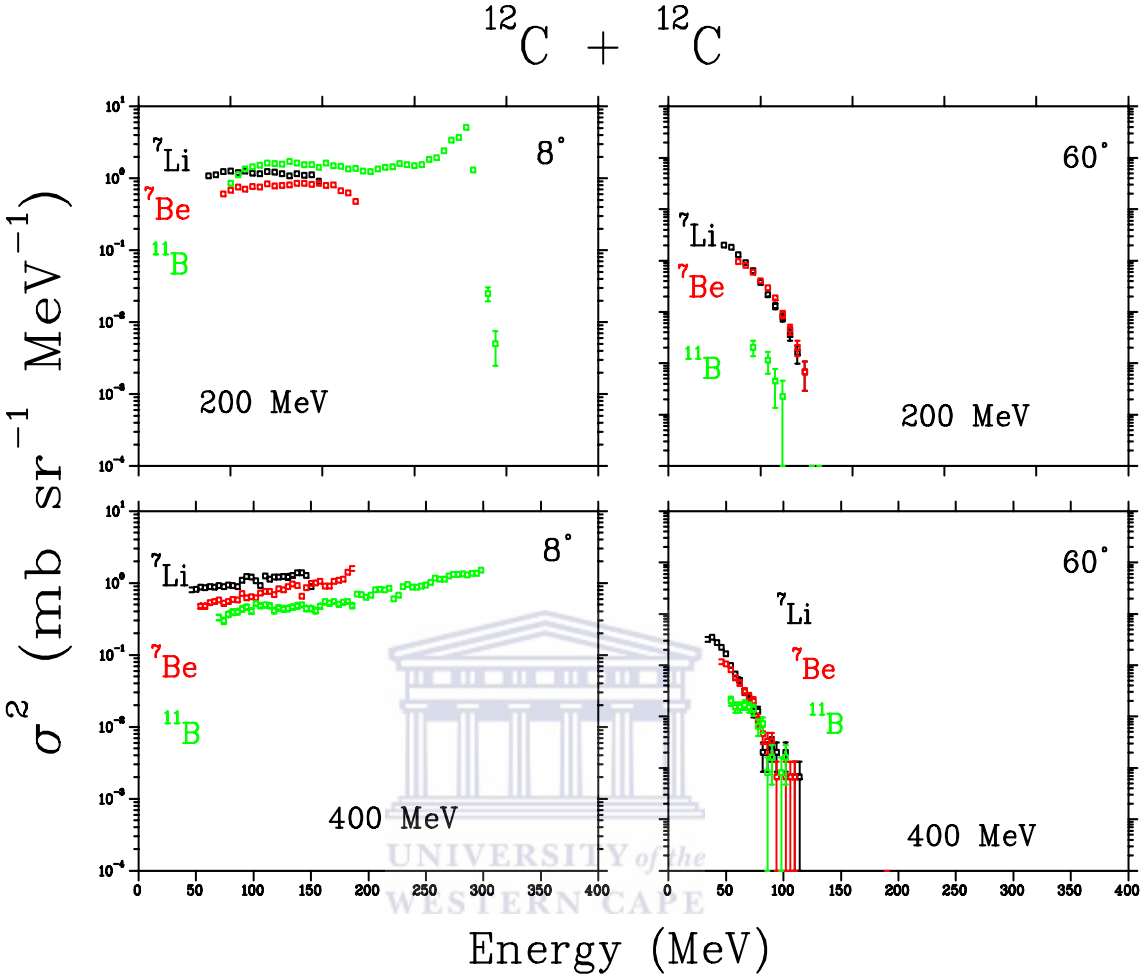

Figure 5.11: Double differential cross sections of ^{7}Li, ^{7}Be ^{11}B emitted at a forward angle of 8º and a backward angle of 60º in the interaction of ^{12}C with ^{12}C at incident energies of 200 and 400 MeV. The error bars reflect the statistical errors.

5.3 Angular distributions of Li, Be and B

Angular distributions of the ^{6,7,8}Li, ^{7,9,10}Be and ^{8,10,11,12}B are shown in figures 5.12 to 5.14. These IMFs were emitted in the interaction of ^{12}C with ^{12}C at incident energies of 200 MeV and 400 MeV. Angular distributions representing emission energies of 20 MeV for the Li and Be fragments and 40 MeV for the B fragments, were extracted from the double differential cross sections measured with the BCD. The other angular distributions at emission energies of 70 MeV, 110 MeV and 150 MeV were extracted

from the data obtained with the Si detector telescope. At the low emission energies and emission angles the cross sections of the Li, Be and B isotopes seem to be isotropic and drop slightly at larger angles, which shows that the fragments are probably produced by the contribution of all reaction mechanisms. At the higher emission energies the slope of Li, Be and B drop more rapidly as a function of emission angle showing an exponential decay graph, which suggests that the fragments are produced by direct reaction mechanisms, these particles are mostly detected at forward angles. Figure 5.15 shows that the angular distributions of ^{6}Li, ^{7}Be and ^{10}B fragments seem to have the same trend which shows that they are all produced by the same reactions mechanisms.

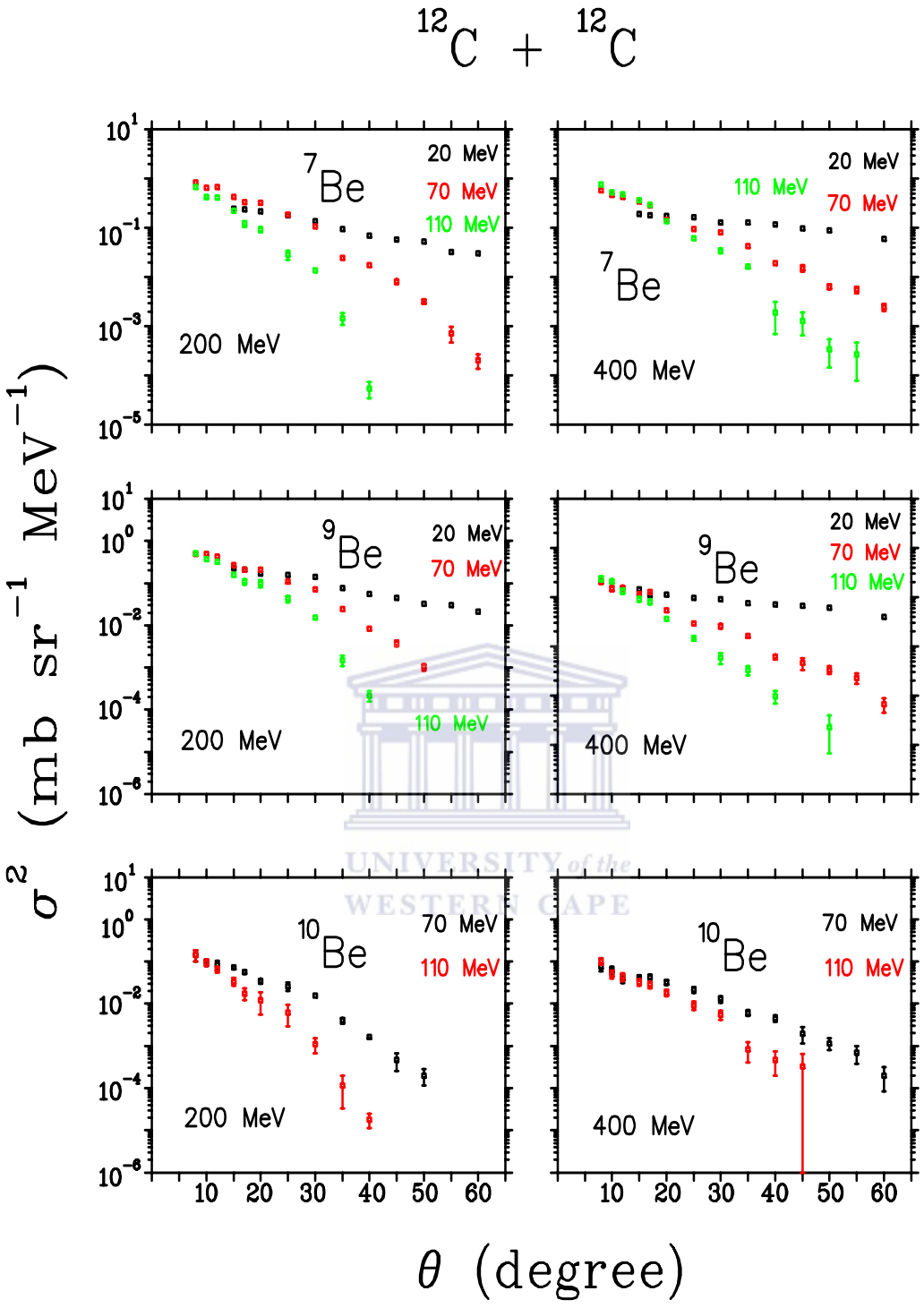

Figure 5.12: Angular distributions of ^{6}Li, ^{7}Li and ^{8}Li measured in the laboratory system in the interaction of ^{12}C with ^{12}C at incident energies of 200 and 400 MeV. The beam energies and the fragments with their emission energies are given in the figures. The error bars reflect the statistical errors.

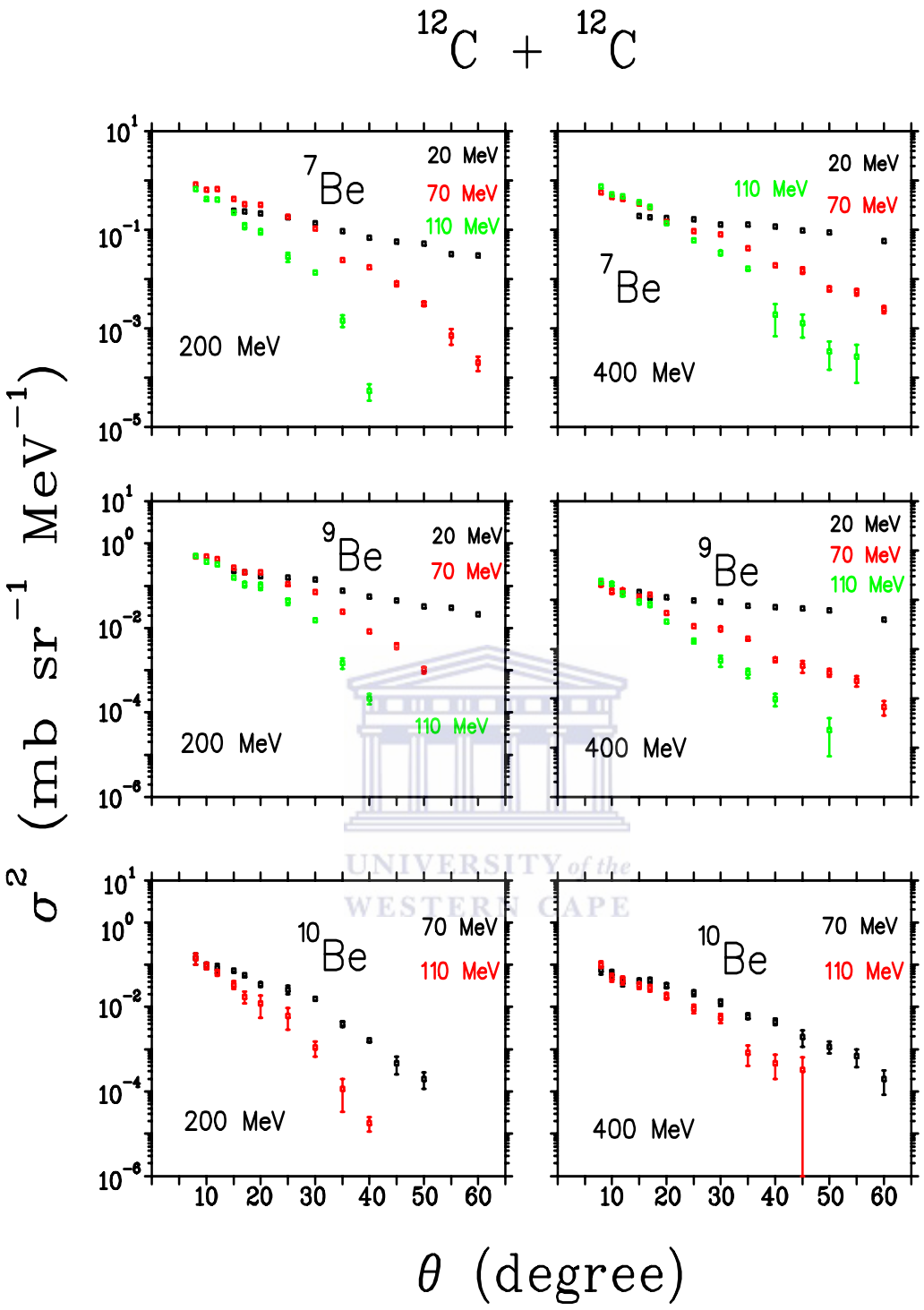

Figure 5.13: Angular distributions of ^{7}Be, ^{9}Be and ^{10}Be measured in the laboratory system the interaction of ^{12}C with ^{12}C at incident energies of 200 and 400 MeV. The beam energies and the fragments with their emission energies are given in the figures. The error bars reflect the statistical errors.

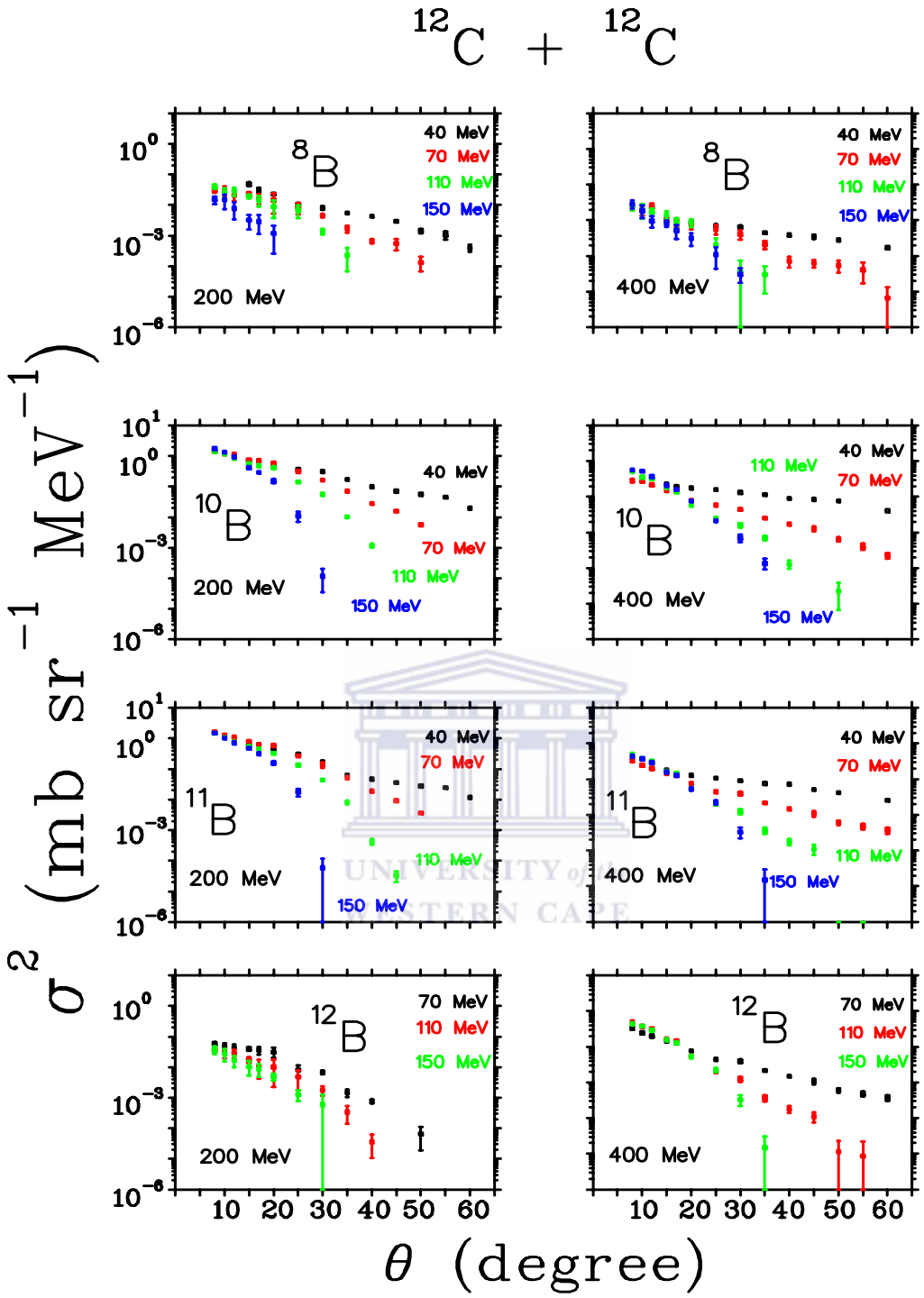

Figure 5.14: Angular distributions of ^{8}B, ^{10}B, ^{11}B and ^{12}B measured in the laboratory system in the interaction of ^{12}C with ^{12}C at incident energies of 200 and 400 MeV. The beam energies and the fragments with their emission energies are given in the figures. The error bars reflect the statistical errors.

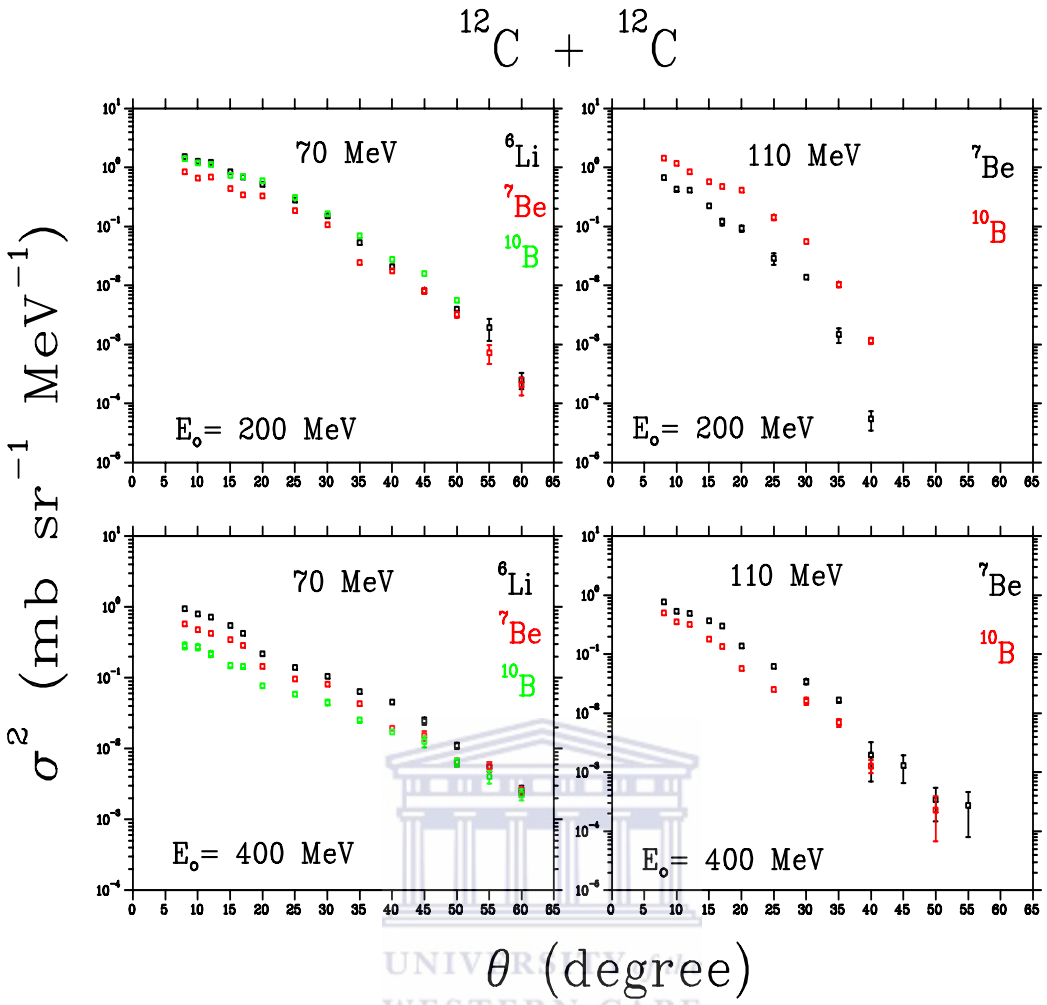

Figure 5.15: Angular distributions of ^{6}Li, ^{7}Be and ^{10}B measured in the interaction of ^{12}C with ^{12}C at incident energies of 200 and 400 MeV. The beam energies and the fragments with their emission energies are given in the figures. The error bars reflect the statistical errors.

5.4 Comparison of experimental energy spectra with the theoretical calculations

The comparison between the experimental data and the theoretical calculations are only shown for the four boron isotopes at the incident energy of 200 MeV. These calculations were obtained by simulating the complete and incomplete fusion and the break-up fusion with the FLUKA-BME new event generator [Mai07]. In the case of the Li and Be isotopes the calculations are hampered by the fact that the energy

spectra are truncated at the high energies due to the high energy thresholds of the Si detector telescope.

Figure 5.16 and together with table 5.1 show the different contributions of the reaction mechanisms considered in this study to interpret the production of ^{11}B. Here, for example, the different reaction mechanism paths for the production of ^{11}B are shown at the emission angle of 12º.

The green line represents the complete fusion of the projectile ^{12}C with the target nucleus ^{12}C leading to the formation of the excited compound nucleus ^{24}Mg* with a fusion cross section of 250 mb (see table 5.1). This excited compound nucleus decays by evaporation. The probability of this compound nucleus to produce light fragments such as ^{11}B as an evaporation residue is however smaller compared to the production of heavier fragments [Mai07].

The violet histogram represents the break-up of the projectile or the target nucleus into ^{11}B and a proton. This reaction is known as projectile or target fragmentation which is a direct reaction, in which ^{11}B is emitted without undergoing any further interactions with the target or the projectile. The high energy part of the histogram shows those ^{11}B which are produced in the break-up of the projectile while the low energy contribution is due to the break-up of the target nucleus.

The red histogram represents the nucleon coalescence process from the cascade of nucleon-nucleon interactions in complete and incomplete fusion of projectile or participant fragment with the target nucleus.

The remaining histograms represent the various break-up fusion processes as given in table 5.1. In these processes the projectile ^{12}C breaks up into two fragments of which one fragment fuses with the target nucleus to form an excited compound nucleus which then decays into ^{11}B and other fragments by evaporation. The incoherent sum of all these mechanisms is given by the black histogram which shows a good correspondence with the experimental data given by the full circles as well as error bars.

Table 5.1: Contains the reaction mechanisms and the break-up cross sections considered in the theoretical calculations.

Fragmentation	Product	Mechanism	Color	σ [mb]
(^{4}He + ^{8}Be) + ^{12}C	^{20}Ne*	Break-up fusion	Yellow	150
(^{6}Li + ^{6}Li) + ^{12}C	^{18}F*	Break-up fusion	Dotted black	50
(^{8}Be + ^{4}He) + ^{12}C	^{16}O*	Break-up fusion	Dashed black	300
(^{10}B + d) + ^{12}C	^{14}N*	Spectator fragment	Light blue/Cyan	40
(^{11}B + p) + ^{12}C	^{13}N*	Spectator fragment	Violet	100
(^{11}C + n) + ^{12}C	^{13}C*	Break-up fusion	Blue	100
^{12}C + ^{12}C	^{24}Mg*	Complete fusion	Green	250

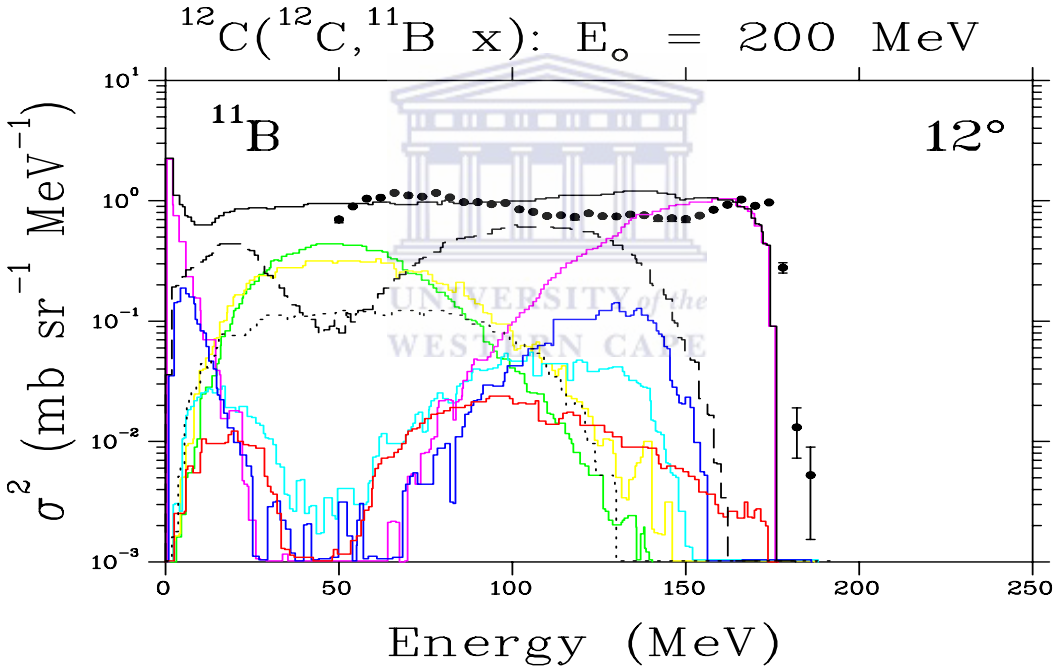

Figure 5.16: Comparison between the experimental data and the theoretical calculations of double differential cross sections of ^{11}B at the emission angle of 12º. The experimental data are given by the full circles with statistical error bars. The red histogram represents the overall contributions from nucleon coalescence. The green histogram is the complete fusion. The remaining histograms show contributions from the break-up fusion processes which are listed in table 5.1 [Mai07]. The solid-line black histogram represents the incoherent sum of all contributions.

Figure 5.17 and 5.18 show the comparisons between the experimental data and the theoretical calculations for ^{8}B. In figure 5.17 at low emission energies the calculated energy spectra slightly overestimate the measured spectra, while at higher emission energies the measured spectra are higher than the calculated spectra. At larger emission angles (figure 5.18) the calculated spectra and the measured spectra show a good correspondence especially from 35º to 50º. Figure 5.19 and 5.20 show the comparisons for ^{10}B between 8º and 60º. At the most forward angles, from 8º and 20º the experimental data show a good correspondence with the calculations, while at larger emission angles (in figure 5.20) the measured spectra overestimate the calculations. In figure 5.21 and 5.22 the comparisons for ^{11}B show the same behavior as that of ^{10}B. At forward angles the measured spectra also show a good correspondence with the theoretical calculations and at larger emission angles the experimental data overestimate the theoretical calculations. The comparisons between the measured and calculated spectra of ^{12}B are shown in figure 5.23 and 5.24. These figures show a good correspondence between the measured and calculated spectra for almost all the emission angles, except at 8º where the calculated spectrum slightly overestimate the measured cross sections and also at 30º the measured spectrum overestimates the calculations.

In summary, at low emission energies these ^{8,10,11,12}B are mainly produced as evaporation residues in the complete fusion of the projectile and target nucleus. At intermediate energies the production of these fragments is due to nucleon coalescence through complete and incomplete fusion and also by break-up fusion reactions. The high energy region is dominated by direct reactions and nucleon transfer reactions which could be the transfer of a proton from the projectile to the target nucleus and produces ^{11}B e.g. ^{12}C (^{12}C, ^{11}B) ^{13}N.

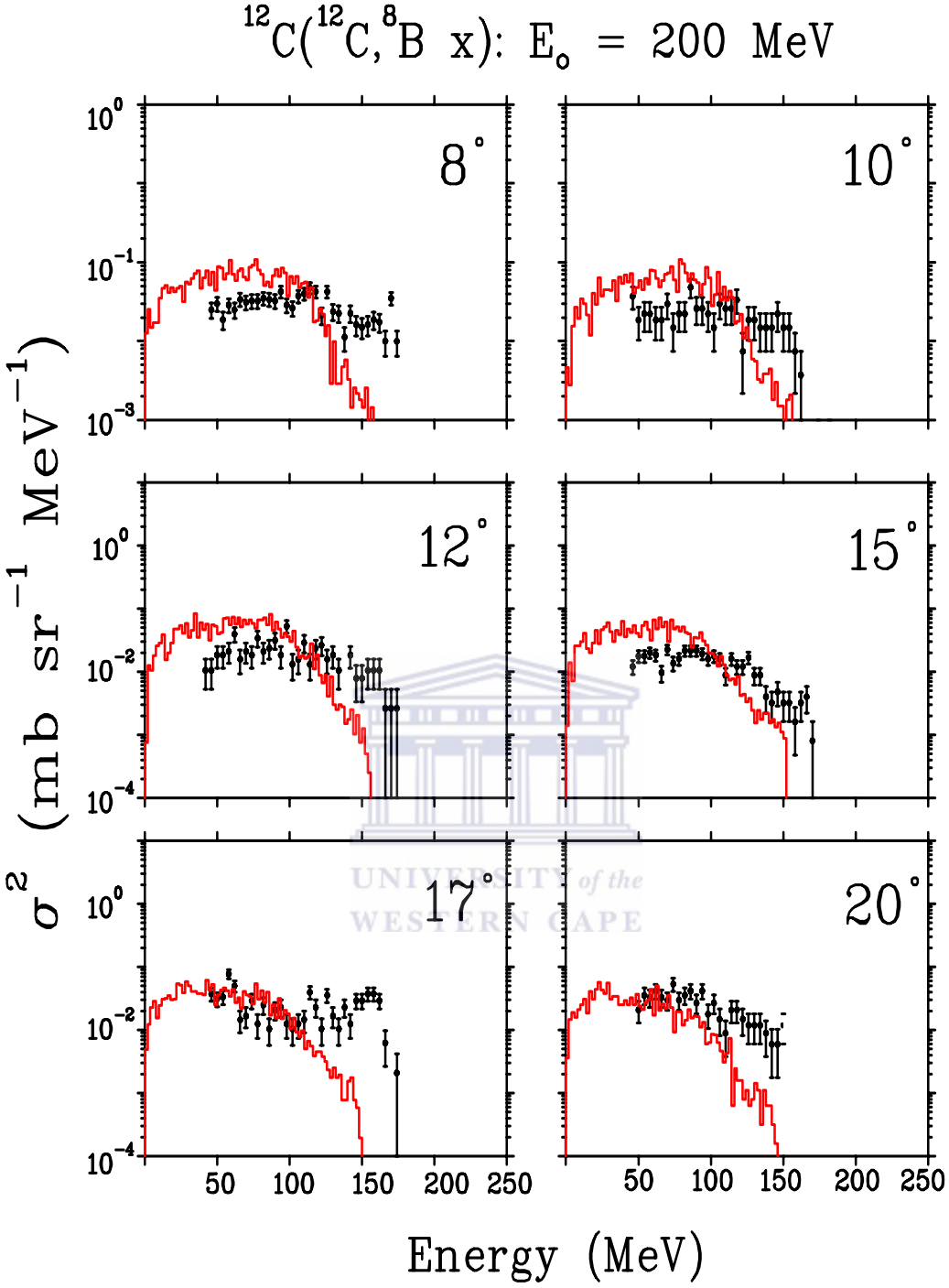

Figure 5.17: Comparisons between the experimental data and the theoretical calculations of double differential cross sections of ^{8}B at different emission angles. The experimental data are given by the full circles with statistical error bars. The incoherent sums of all contributions are represented by the red histograms [Mai07].

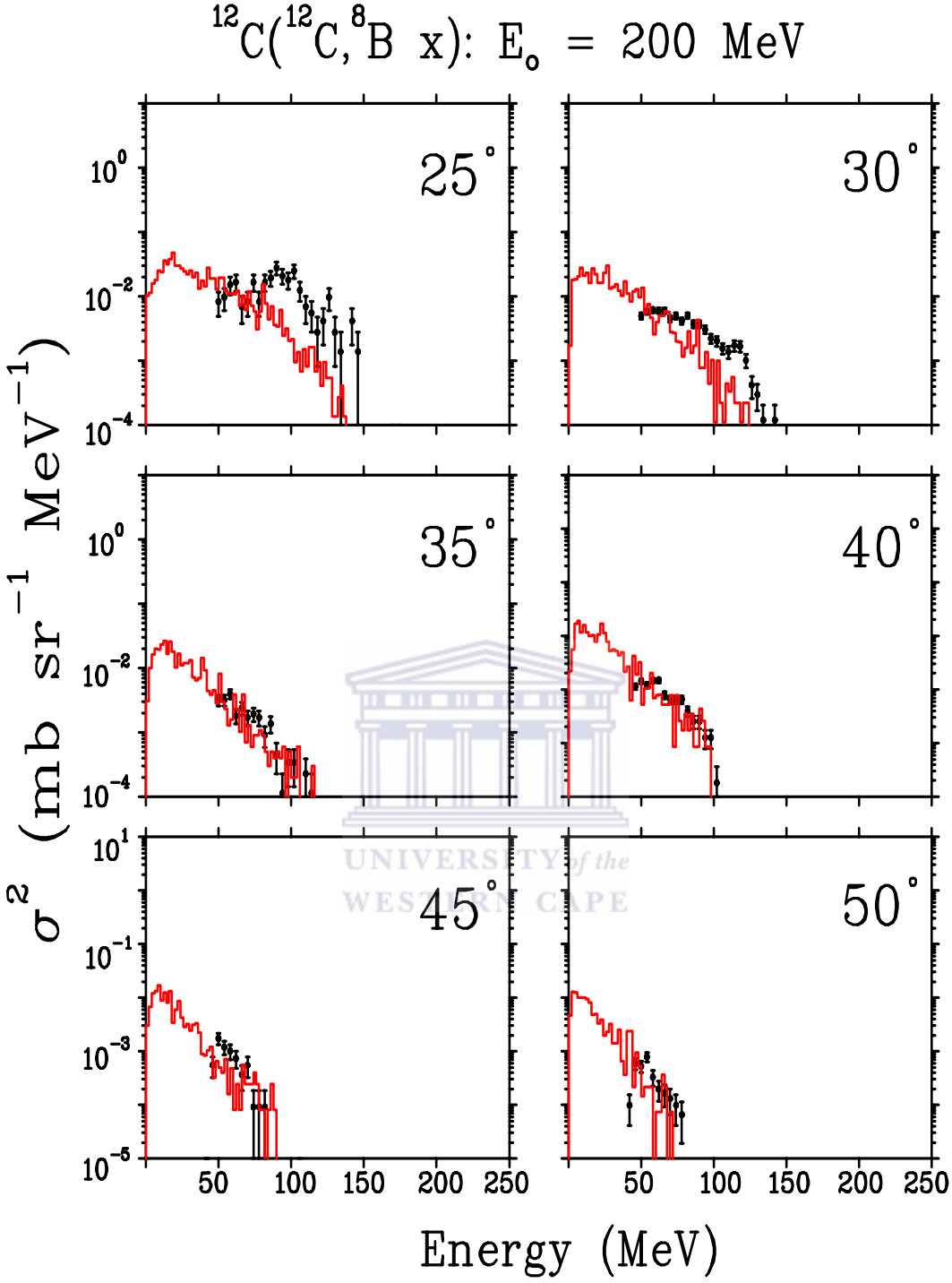

Figure 5.18: See caption of figure 5.17.

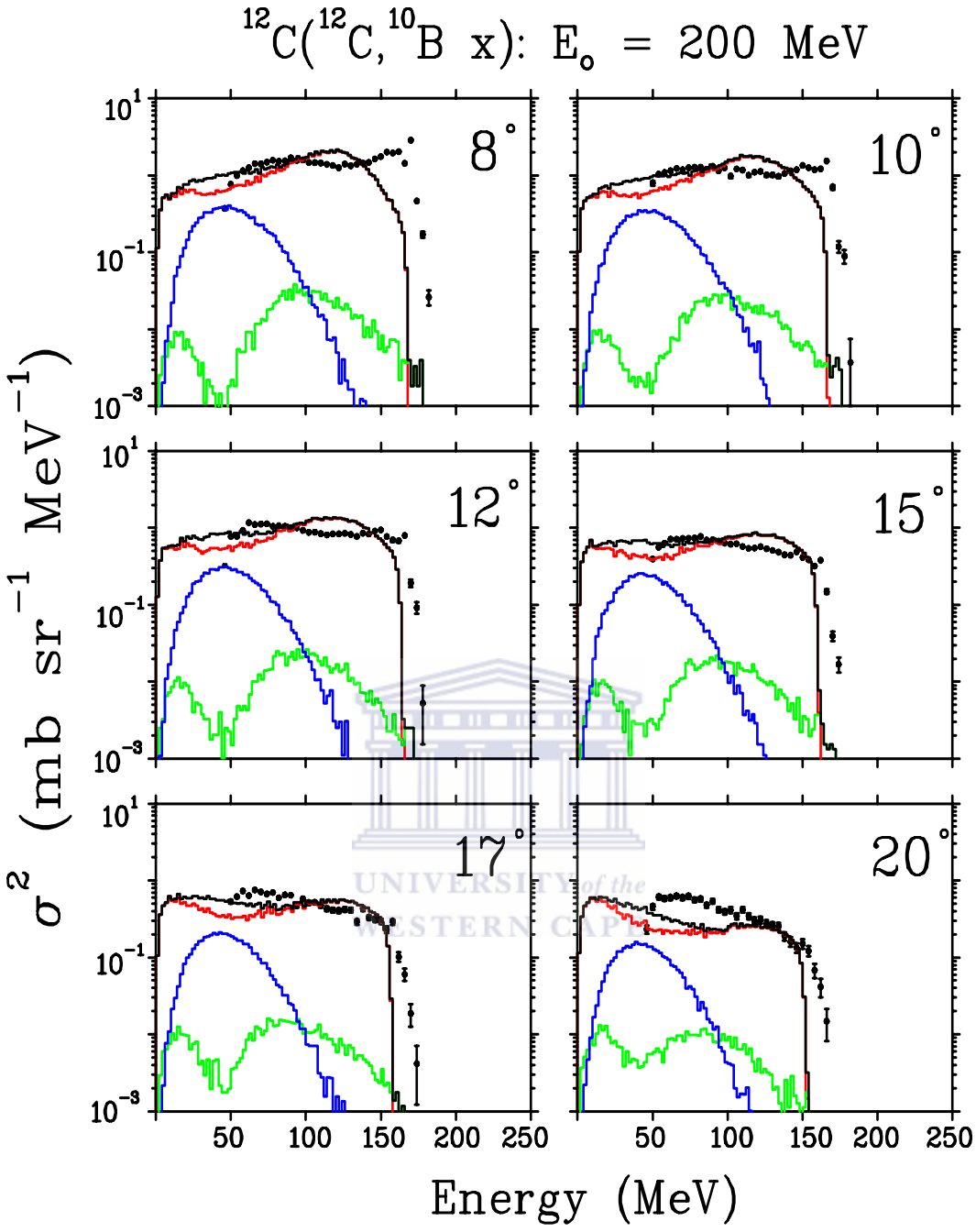

Figure 5.19: Comparisons between the experimental data and the theoretical calculations of double differential cross sections of ^{10}B at different emission angles. The experimental data are given by the full circles with statistical error bars. The blue histograms represent the complete fusion (CF) and the red histograms represent the break-up fusion (BF) processes followed by nucleon coalescence. The green histograms represent the reaction $^{12}C(^{12}C,^{10}B)^{14}N$. The incoherent sums of all contributions are given by the black histograms [Mai07].

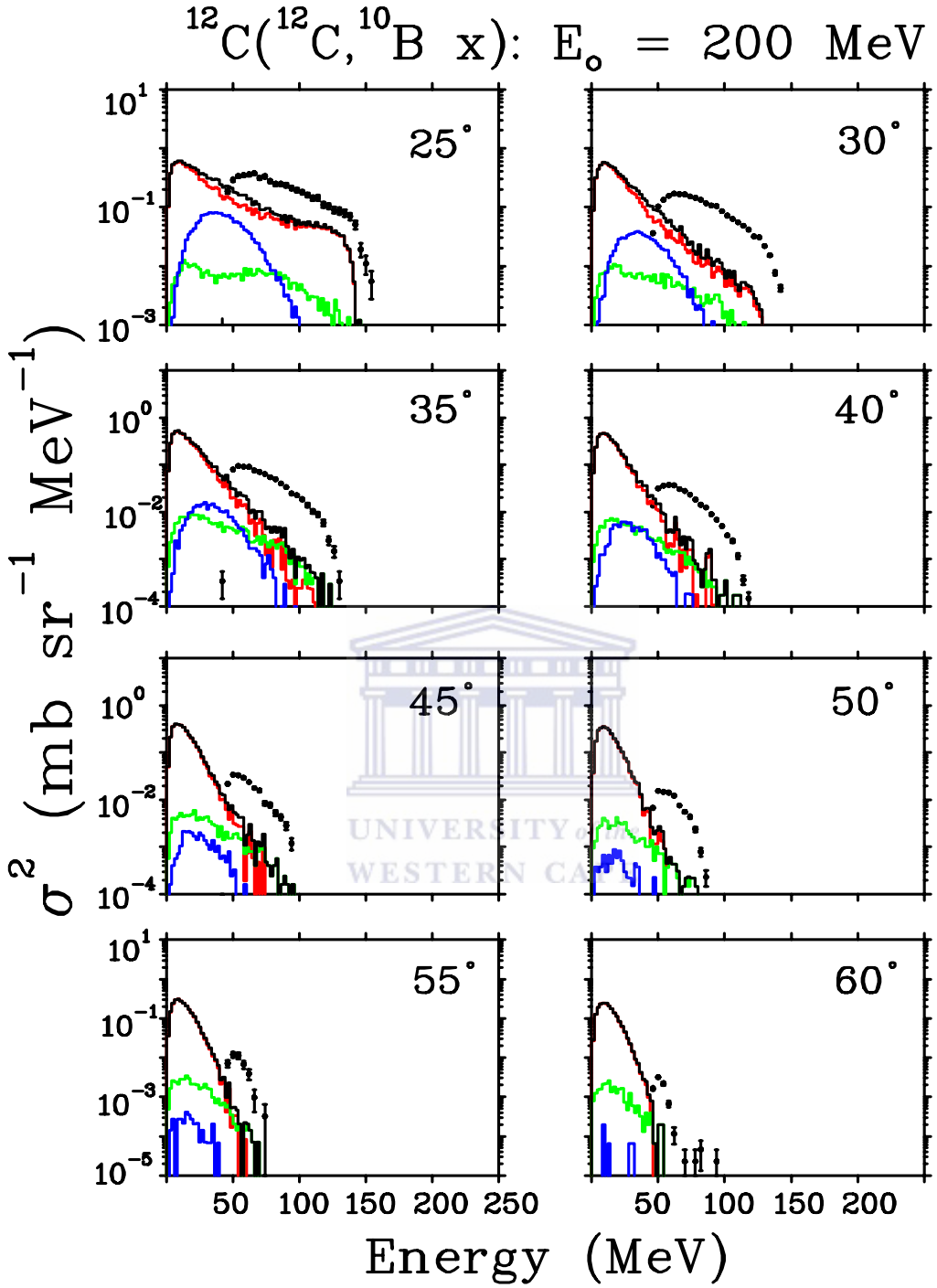

Figure 5.20: See caption of figure 5.19.

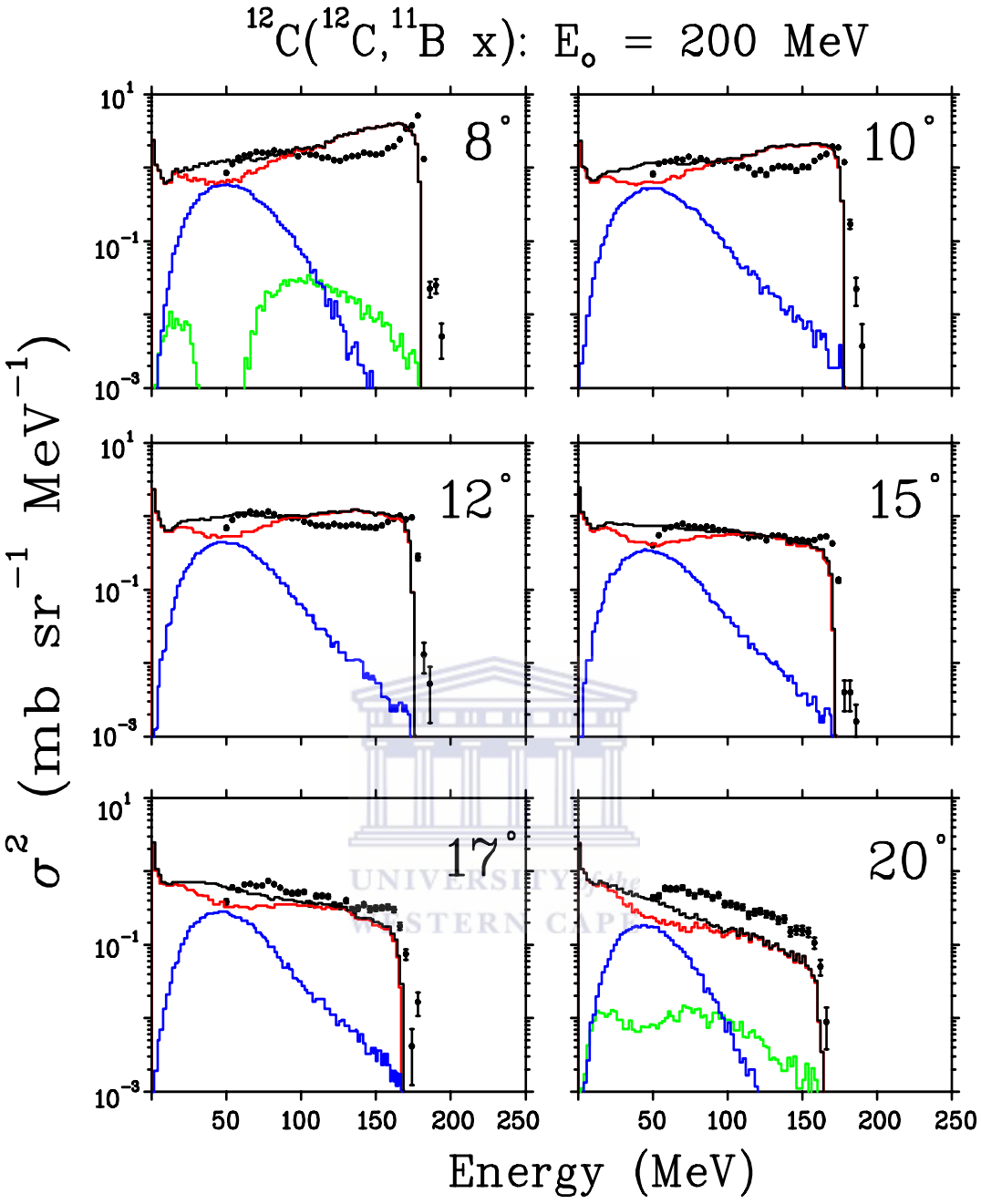

Figure 5.21: Comparisons between the experimental data and the theoretical calculations of double differential cross sections of ^{11}B at different emission angles. The experimental data are given by the full circles with statistical error bars. The blue histograms represent the complete fusion (CF) and the red histograms represent the break-up fusion (BF) processes followed by nucleon coalescence. The green histograms represent the reaction $^{12}C(^{12}C,^{10}B)^{14}N$. The incoherent sums of all contributions are given by the black histograms [Mai07].

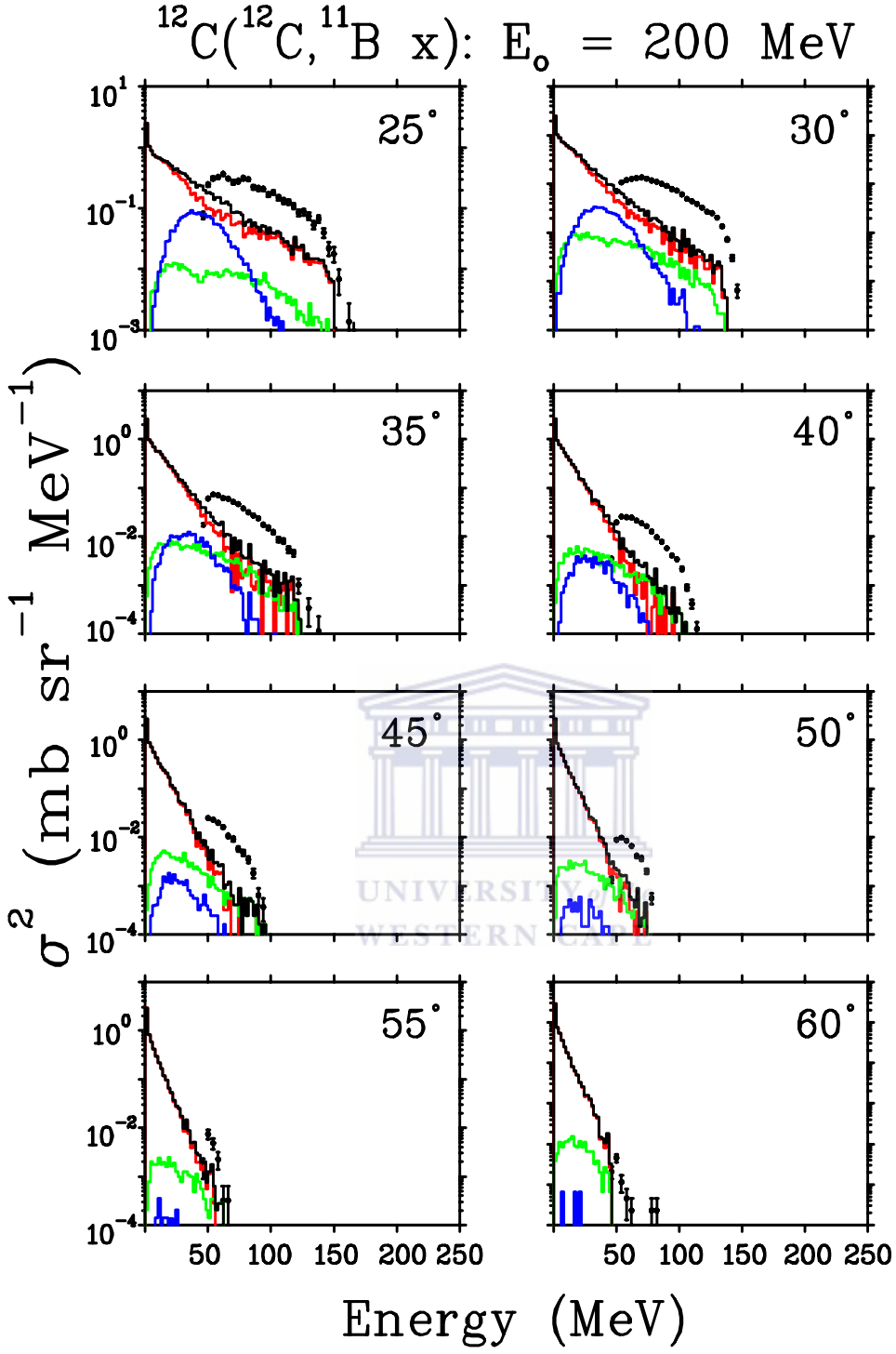

Figure 5.22: See caption of figure 5.21.

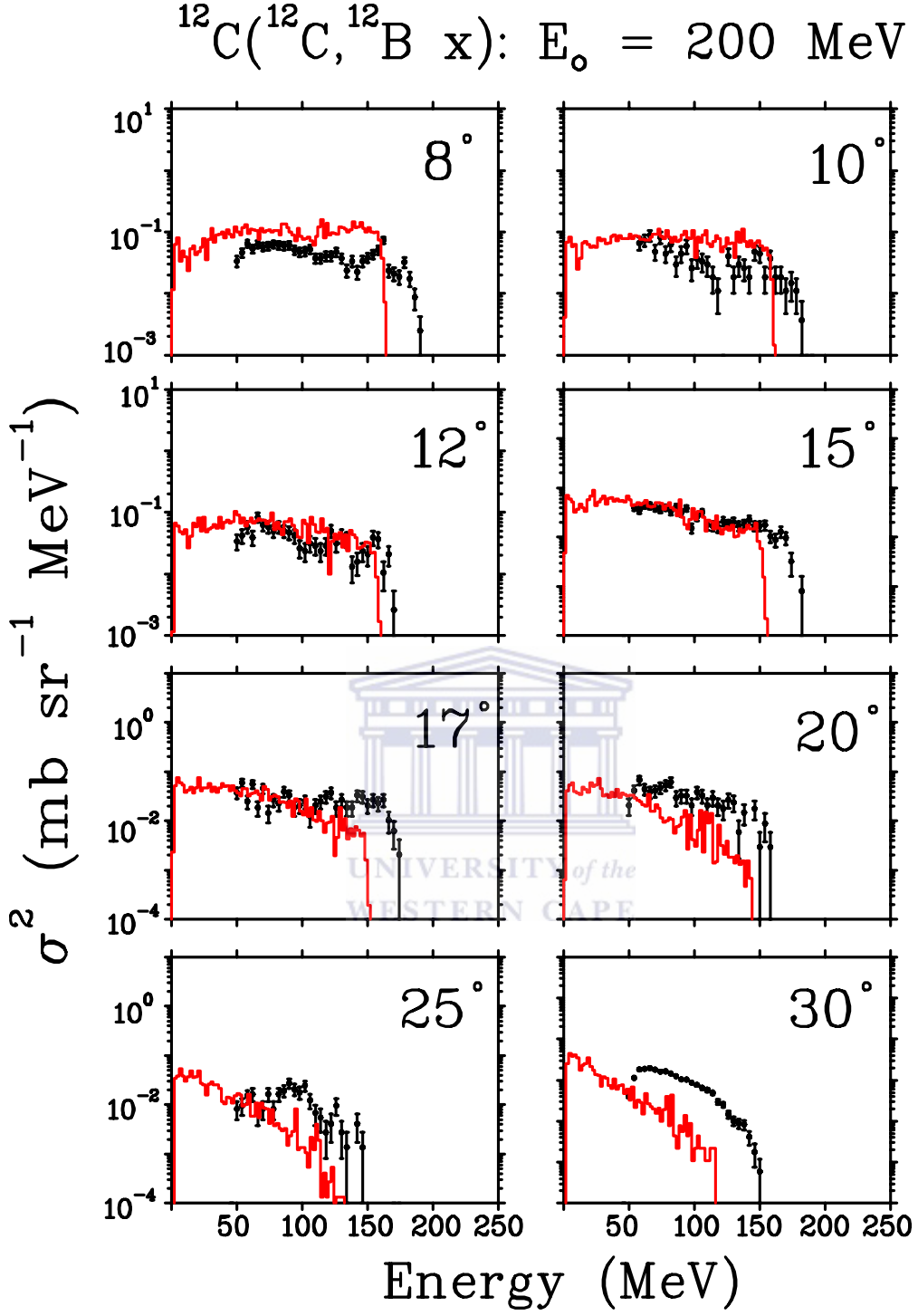

Figure 5.23: Comparisons between the experimental data and the theoretical calculations of double differential cross sections of ^{12}B at different emission angles. The experimental data are given by the full circles with statistical error bars. The incoherent sums of all contributions is represented by the red histograms [Mai07].

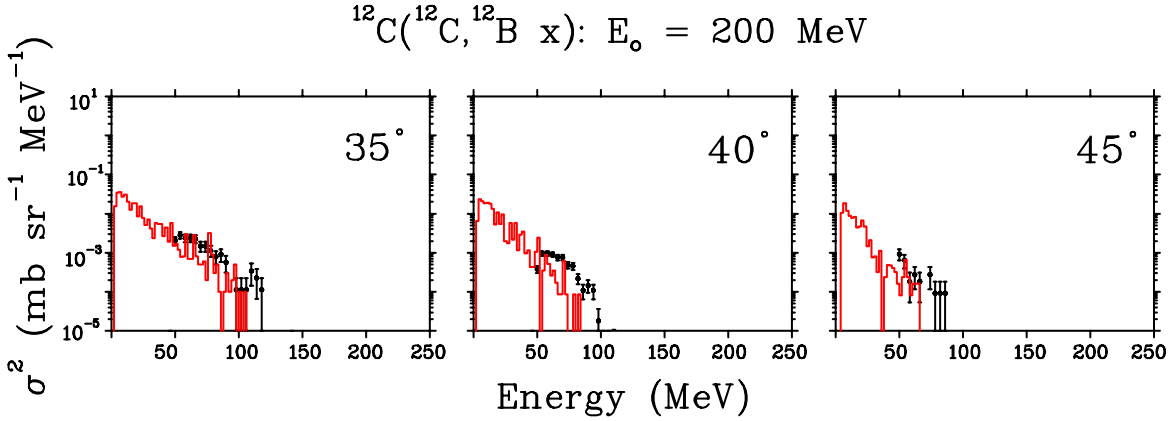

Figure 5.24: See caption of figure 5.23.

CHAPTER 6

Summary and conclusions

The aim of the present study was to investigate and contribute to the understanding of the reaction mechanisms involved in the production of ^{6,7,8}Li, ^{7,9,10}Be and ^{8,10,11,12}B isotopes emitted in the interaction of ^{12}C with ^{12}C at incident energies of 200 and 400 MeV. The BCD which has a low energy threshold was used to measure the low energy part of the spectra over an angular range between 15º and 60º, while the Si detector telescope was used to measure the high energy part of the spectra over an angular range between 8º and 60º.

The standard ΔE-E technique was used to obtain the particle identification spectra for the data measured with the Si detector telescope by plotting the energy lost in ΔE detector against the energy deposited in the E detector. In the case of the BCD the Bragg peak of the ion that stopped inside the active volume of the BCD was plotted against the energy deposited by the ion inside the BCD. The Bragg peak is proportional to the charge (Z) of the particle. The energy gap between the data extracted with the BCD and the Si detector telescope is due to the high and low energy thresholds of the BCD and the Si detector telescope, respectively.

In order to overcome the high energy thresholds of the Si detector telescope the detector's thickness should be increased to prevent the light IMFs from punching through the detectors. For the BCD the gas pressure could be increased in order to increase the range of the ions that stop inside the detector. This would eliminate the gap between the BCD data and the data obtained with the Si detector telescope. Nevertheless, the cross sections show that the data extracted with the BCD are more or less consistent with the data extracted using the Si detector telescope. The ^{6}Li and ^{7}Li seem to be produced at almost the same rate, ^{8}Li was produced at a much lower rate. In the case of Be isotopes the production rate of ^{10}Be is less than the rate of ^{7}Be and ^{9}Be. Although ^{9}Be is produced with the rate slightly lower than ^{7}Be. For the B

isotopes ^{8}B and ^{12}B as well as ^{10}B and ^{11}B are produced similar rate, respectively, ^{10}B and ^{11}B are produced at a higher rate than ^{8}B and ^{12}B.

The theoretical calculations were performed only for the spectra of ^{8}B, ^{10}B, ^{11}B and ^{12}B. The calculations could not be performed for the Li and Be isotopes because the high energy part of these spectra was truncated due to the high energy thresholds of the Si detector telescope. The overall comparisons between the experimental data and the theoretical spectra of the B isotopes show good agreement at almost all the emission angles. At low emission energies the production of the B isotopes is dominated by complete fusion reactions of the projectile and the target nucleus leaving ^{8,10,11,12}B as evaporation residues. The probability of producing even lighter IMFs such as the Li and Be isotopes as evaporation residues is far less probable. At intermediate emission energies the production of IMFs is dominated by nucleon coalescence through complete and incomplete fusion reactions, pre-equilibrium emission and also break-up fusion fragments. The high emission energies were dominated by direct reaction, for example the direct nucleon transfer. The reaction mechanism such as nucleon transfer contributes mainly at forward angles and its contribution decreases with an increasing emission angle, but the contribution of fragmentation, evaporation and nucleon coalescence dominates even at large emission angles.

Based on the calculations performed for the B isotopes at 200 MeV, one can draw a conclusion about the reaction mechanisms involved in the production of Li and Be isotopes at 200 MeV beam and also predict the mechanisms involved in the production of Li, Be and B isotopes produced at 400 MeV beam. A comparison of the cross sections for instance of ^{7}Li, ^{7}Be and ^{11}B seem to follow the same trend at forward and also at larger angles which show that it is likely that they are produced by the same reaction mechanisms. It was also found that the results extracted from the 400 MeV runs have the same behaviour as the results extracted from 200 MeV run at all emission angles as function of emission energies. From these results it can be assumed that the IMFs produced at 400 MeV beam are most likely produced by the same reaction mechanisms as the IMFs produced in the interaction of ^{12}C with ^{12}C at an incident energy of 200 MeV.

The mechanisms which dominate the production of IMFs in the present study are fragmentation, break-up fusion, nucleon coalescence through complete and incomplete fusion and evaporation.

REFERENCES

[And92] L. N. Andronenko, M. N. Andronenko, A. A. Kotov, W. Neubert, L. A. Vaishnene, S. A. Pavlenko, D. M.. Seliverstov, V. L. Stepanov, V. I. Yatsura, Nuclear Instruments and Methods A **312**, 467-474 (1992).

[Ass82] J. M. Asselineau, J. Duchon, M. L'Haridon, P. Mosrin, R. Regimbart And B. Tamain, Nuclear Instruments and Method **204**, 109-115 (1982).

[Bar04] R. Barna, V. Bollini, A. Bubak, A. Budzanowsli, D. De Pasquale, D. Filges, S. V. Förtsch, F. Goldenbaum, A. Hczko, H. Hadde, A. Italiano, L. Jarczyk, B. Kamys, J. Kasiel, M. Kirstryn, St. Kistryn, St. Kliczewski, W. Migdal, H. Ohm, N. Paul, B. Piskor.Ignatowicz, K. Pysz, Z. Rudy, H. Schaal, R. Siudak, E. Stephan, G. F. Steyn, R. Sworst, T. Thovhogi, M. Wojciechowski, W. Zipper, Nuclear Instruments and Methods in Physics Research A **519**, 610-622 (2004).

[Bas05] M. S. Basunia, E. B. Norman, H. A. Shuqart, A. R. Smith, M. J. Dolinski, and B. J. Quiter, Phy. Rev. C **71**, 035801 (2005).

[Bec03] B. Becker, F. Albertini, E. Gadioli, G. F. Steyn, M. Cavinato, S.H. Connel, A. A. Cowley, E. Fabrici, S. V. Förtsch, E.Gadioli Erba, J. J. Lawrie, and E. Sideras Haddad, Eur. Phys. J. A **18,** 639-644 (2003).

[Bha94] C. Bhattacharya, S. Bhattacharya, and K. Krishna, Phys. Rev. C **49**, 3147 (1994).

[Cav96] M. Cavinato, E. Fabrici, E. Gadioli, E. Gadioli Erba, M. Galmarini, A. Gritti, Z. Phys. A **347** (1996) 471.

[Cam04] A. Gómez Camacho and E. F. Aguilera, REVISTA MEXICANA DE FISICA 50 (3) 265-271 (2004)

[Cav98] M. Cavinato, E. Fabrici, E. Gadioli, E. Gadioli Erba, E. Risi, Nuclear Physics A **643**, 15-29 (1998).

[Cav01] M. Cavinato, E. Fabrici, E. Gadioli*, E. Gadioli Erba, G. Riva, Nuclear Physics A **679**, 753-764 (2001).

[Den98] B. Denecke and S. de Jonge, Appl. Rad. Iso. (1998).

[Dla06] J. Dlamini, Masters Thesis Unpublished (2006).

[För05] S. V. Förtsch, F. Cerutti,P. Colleoni, E. Gadioli, A. Mairani, G. F. Steyn, J. J. Lawrie, F. D. Smit, S. H. Connell, R. W. Fearick, T. Thovhogi, H. Machner, F. Goldenbaum, K. Pysz, AIP Conference Proceedings, Vol. 769, 1642-1645 (2005).

[För07] S. V. Förtsch, F. Cerutti,P. Colleoni, E. Gadioli, E. Gadioli-Erba, A. Mairani, G. F. Steyn, J. J. Lawrie, F. D. Smit, S. H. Connell, R. W. Fearick, T. Thovhogi, Nuclear Physics A (2007).

[Fuc94] H. Fuchs and K. Möhring, Rep. Prog. Phys. **57,** 231-324 (1994).

[Gad00] E. Gadioli, M. Cavinato, E. Gadioli Erba, R. Bassini, C. Birattari, S. Crippa, G. F. Steyn, S.V. Förtsch, , J. J. Lawrie, F. M. Nortier, S. H. Connell, E. Sideras Haddad, J. P. F. Sellschop, A. A. Cowley, "Evidence for a dissipative friction mechanisms based on ^{8}Be fragments from the interaction of ^{12}C with ^{59}Co." (Unpublished).

[Gad02] E. Gadioli, G. F. Steyn, C. Birattari, C. Catarinaro, M. Cavinato, S. H. Connell, A. A. Cowley, E. Fabrici, S.V. Förtsch, E. Gadioli Erba, J. J. Lawrie, J. P. F. Sellschop and E. Sideras Haddad, Nuclear Physics A **708**, 391-412 (2002).

[Gad03] E. Gadioli, G. F. Steyn, F. Albertini, C. Birattari, M. Cavinato, S. H. Connell, A. A. Cowley, E. Fabrici, S.V. Förtsch, E. Gadioli Erba,

J. J. Lawrie, M. Pigni, J. P. F. Sellschop and E. Sideras Haddad, Eur. Phys. J. A **17**, 195-212 (2003).

[Gad92] E. Gadioli and P.E. Hodgson. Pre-Eqiulibrium Nuclear Reactions (Oxford Clarendon Press, 1992).

[Gad99] E. Gadioli, M. Cavinato, E. Fabrici, E. Gadioli Erba, C. Birattari, I. Mica, S. Solia G. F. Steyn, S.V. Förtsch, , J. J. Lawrie, F. M. Nortier, T. G. Stevens, S. H. Connell, J. P. F. Sellschop, A. A. Cowley, Nuclear Physics A **654**, 523-540 (1999).

[Gou83] C. R. Gould, N. R. Roberson, IEEE Transaction on Nuclear Science, Vol. NS-**30**, No. 5 (1983)

[Gru82] C. R. Cruhn, M. Binimi, R. Legrain, R. Loveman, W. Pang, M. Roach, D. K. Scott, A. Shotter, T. J. Symons, J. Wouters, and M Zisman, Nuclear Instrument and Methods **196**, 33-40 (1982).

[Hod97] P. E. Hodgson, E. Gadioli, E. Gadioli Erba, Introductory Nuclear Physics, Oxford Science Publications (1997).

[Hus81] M.S Hussein, K. W. McVoy and D. Saloner, Physics Letters, **98B**, no. **3**, 162-165 (1981).

[Jip84] P. Jipsen, ELOSS, A Program for Calculating the Ranges of Ions in Matter, National Accelerator Center (1984) (Unpublished).

[Leo87] W.R. Leo, Techniques for Nuclear and Particle Physics Experiments, (1987).

[Lil01] J. Lilley, Nuclear Physics Principle and Applications, Wiley and Sons (2001).

[Mag98] A. Magiera, J. Hebenstreit, L. Jarczyk, B. Kamys, A. Strzalkowski, and B. Styezen, Phy. Rev. C **57**, 749-763 (1998).

[Mai07] A. Mairani, PhD thesis, Unpublished (2007).

[McV80] K. W. McVoy, M. Carolina Nemes, Z. Phys. A **295**, 177 (1980).

[Met04] W. A. Metwally, R. P Gardner and C. W. Mayo, Nuclear Instruments and Methods in Physics Research Section B: Beam Interaction with Materials and Atoms, Vol. **213**, 394-399 (2004).

[Mud05] L. J. Mudau, M.Sc thesis. "Emission of ^{3}He and ^{6}He particles from the interaction of ^{12}C with ^{93}Nb at 400 MeV incident energy" (unpublished).

[Och96] H. Ochiishi, H. Ito, K. Kimura, S. Kouda, T. Murakami, M. Shimooka, Y. Sugaya, K. H. Tanaka, S. Toyama, Y. Yamanoi, K. Yamamoto, K. Yasuda, Nuclear Instruments and Methods in Physics Research A **369,** 269-276 (1996).

[Pil96] J. V. Pilcher, The NAC MBD to VME Conversion Guide (1996).

[Ram01] H. Ramebäck, M. Berglund, D. Vendelbo, R. Wellum, P. D. P. Taylor, Institute for Reference material and measurements, European Commission-SRC, B-2440 (2001).

[Rit85] R. Ritzka, W. Dünnweber, A. Glaesner, W. Hering, H. Puchta, and W. Trautmann, Phys. Rev. C **31**, 133 (1985).

[Ser47] R. Serber, Phys. Rev. **72**, 1008 (1947).

[She85] N. J. Shenhav and H. Stelzer, Nuclear Instruments and Methods in Physics Research **228,** 359-364 (1985).

[Sin68] J. J. Singh and E. Rind, NASA TECHNICAL NOTES, high energy proton damage in Silicon Surface Barrier detectors (1968).

[Tyk95] R. Tykva, J. Sabol, Low-level Environmental Radioactivity: Sources and Evaluation (1995).